Aus dem Institut für Neuropathologie

(Zentrum für Neuropathologie und Prionforschung ZNP)

Institut der Ludwig-Maximilians-Universität München

DMG brain organoids: A new preclinical model for H3K27- altered diffuse midline glioma

Dissertation

zum Erwerb des Doktorgrades der Humanbiologie

an der Medizinischen Fakultät der

Ludwig-Maximilians-Universität München

vorgelegt von

Marbod Julian Klenner

aus

München

Jahr

2024

Mit Genehmigung der Medizinischen Fakultät der
Ludwig-Maximilians-Universität zu München

Erster Gutachter:	Prof. Dr. Jochen Herms
Zweiter Gutachter:	Prof. Dr. Kirsten Lauber
Dritter Gutachter:	Priv. Doz. Dr. Roland Kälin

Mitbetreuung durch den promovierten Mitarbeiter:	Dr.med. Alexander Beck
Dekan:	Prof. Dr. med. Thomas Gudermann

Tag der mündlichen Prüfung: 15.01.2024

Table of contents

Zusammenfassung

Bösartige Tumore des Gehirns zählen zu den häufigsten Todesursachen im Kindesalter, wobei das H3K27-mutierte diffuse Mittelliniengliom (DMG) zu den tödlichsten pädiatrischen Hirntumoren gehört. Die derzeitige Standardtherapie besteht aus der Bestrahlung des Tumors mit adjuvanter Gabe von Temozolomid, wobei die Überlebenszeit der jungen Patienten nur um wenige Monate verlängert wird. An präklinischen Modelsystemen wurden vielversprechende Arzneimittelkandidaten identifiziert, jedoch zeigen nur wenige dieser Wirkstoffe positive Effekte in der Klinik. Dieses eingeschränkte Transferpotential medikamentenbasierter Therapien verdeutlicht den Bedarf an neuen DMG-Modellen. Ziel dieser Arbeit war es daher, ein repräsentatives *In-vitro*-DMG-Modell für die Wirkstofftestung zu entwickeln. Zu diesem Zweck wurden dreidimensionale zerebrale Organoide mit H3K27M DMG-Tumorzellen co-kultiviert, was zur Bildung von DMG brain organoids (DBO) führte. Einzelzell-CODEX Analysen zeigten, dass die Co-Kultur eine Tumorzellzusammensetzung (AC-, OC- und OPC-ähnliche Tumorzellen) induziert, die der Situation im Tumor stärker ähnelt, als es bei anderen präklinischen Modellsystemen der Fall ist. Anschließend wurde ein Behandlungsschema etabliert, um die Effekte vielversprechender Arzneimittelkandidaten aus der aktuellen Forschung genauer zu charakterisieren. Fluoreszenzmikroskopische Methoden wurden eingesetzt, um die Verringerung der Tumorzellen in DBOs, das Proliferationspotenzial sowie die Zusammensetzung der Tumorzell-Subpopulationen quantitativ zu analysieren. Speziell die NAMPT-Inhibitoren Daporinad und GMX1778 erwiesen sich als potente Wirkstoffe, die die Tumorlast der DBOs stark verringerten. Auch die HDAC-Inhibitoren Romidepsin und Panobinostat zeichneten sich durch eine tumorreduzierende Wirkung aus. Panobinostat verringerte hier speziell die potenziell tumortreibende OPC-ähnliche Subpopulation. Zusätzlich zeigten beide Wirkstoffe eine stark ausgeprägte Proliferationsinhibition der verbleibenden Tumorzellen. Die Behandlungen mit dem DRD2-Antagonisten ONC206 führten ebenfalls zu einer vielversprechenden Kombination von DBO-Tumorlastreduktion und Proliferationshemmung. ONC206 erwies sich als potenter im Vergleich zu seinem Analogon ONC201 und reduzierte alle Tumorzellsubpopulationen relativ gleichmäßig. Auch CDK- (Dinaciclib, Zotiraciclib) und Proteasom-Inhibitoren (Delanzomib) reduzierten die Tumorlast stark und verringerten die Proliferation der verbleibenden DMG-Zellen. Ein speziell antiproliferativer Effekt wurde bei allen verwendeten HSP90-Inhibitoren beobachtet, wobei sich die Wirkstoffe AUY922 und HSP990 als besonders wirksam erwiesen. Wie die Ergebnisse der Behandlungen zeigen, könnten DBOs ein nützliches Instrument zur detaillierten Charakterisierung einzelner therapeutischer Effekte sein. Ferner ließ sich beobachten, dass die zytotoxische Wirkung mehrerer Medikamente (unter anderem Panobinostat, Marizomib sowie AUY922 und HSP990) auf H3K27M Zellen in DBOs geringer ausfiel als in anderen *In-vitro*-Testungen. Dies lässt eine geringere Sensitivität der Zellen vermuten, was im Hinblick auf das therapieresistente Tumorverhalten in der Klinik eine interessante Modelleigenschaft sein könnte. Zusammen mit der Möglichkeit, DBOs durch den Einsatz moderner Laborgeräte in größeren Mengen zu generieren, könnte das Modellsystem dazu beitragen, das translationale Potenzial präklinischen Wirkstofftestungen zu erhöhen.

Abstract

Malignant tumors of the brain are among the leading causes of death in childhood, with H3K27-mutated diffuse midline glioma (DMG) being one of the most lethal pediatric brain tumors. Currently, standard therapy involves radiation of the tumor with adjuvant administration of temozolomide, prolonging survival of young patients by only a few months. Promising drug candidates have been identified using preclinical model systems, but only a few of these agents show positive effects in the clinic. This limited translational potential of drug-based therapies highlights the need for new DMG models. Therefore, the aim of this work was to develop a representative *in vitro* DMG model for drug testing. Three-dimensional cerebral organoids were co-cultured with H3K27M DMG tumor cells for this purpose, resulting in the formation of DMG brain organoids (DBO). Single-cell CODEX analyses showed that co-culture induced a tumor cell composition (AC-, OC-, and OPC-like tumor cells) more similar to the situation in the tumor than seen in other preclinical model systems. Subsequently, a treatment regimen was established to further characterize the effects of promising drug candidates from current research. Fluorescence microscopic methods were used to quantitatively analyze the reduction of tumor cells in DBOs, the proliferation potential, and the composition of tumor cell subpopulations. Specifically, the NAMPT inhibitors daporinad and GMX1778 were found to be potent agents that greatly reduced the tumor burden of DBOs. The HDAC inhibitors romidepsin and panobinostat were also characterized by tumor-reducing properties and panobinostat specifically decreased the potentially tumor-driving OPC-like subpopulation here. In addition, both agents showed a strong proliferation inhibition of the remaining tumor cells. Treatments with the DRD2 antagonist ONC206 also resulted in a promising combination of DBO tumor burden reduction and proliferation inhibition. ONC206 proved to be more potent compared with its analogue ONC201, reducing all tumor cell subpopulations relatively equally. CDK (dinaciclib, zotiraciclib) and proteasome (delanzomib) inhibitors also strongly reduced tumor burden and decreased proliferation of the remaining DMG cells. A specific antiproliferative effect was observed with all HSP90 inhibitors used, with AUY922 and HSP990 being particularly potent. As shown by the results of the treatments, DBOs could be a useful tool for detailed characterization of individual therapeutic effects. Furthermore, it could be observed that the cytotoxic effect of several drugs (including panobinostat, marizomib, AUY922 and HSP990) on H3K27M cells was lower in DBOs compared to other *in vitro* studies. This suggests a lower sensitivity of the cells, which could be an interesting model feature with regard to therapy-resistant tumor behavior in the clinic. Together with the possibility of generating DBOs in larger quantities by using modern laboratory equipment, the model system could help to increase the translational potential of preclinical drug testing.

Figures

Tables

Abbreviation

CODEX	CO-Detection by indEXing
AC-like	Astrocytic-like
APOE	Apolipoprotein E
BBB	Blood-brain barrier
BCAS1	Brain enriched myelin associated protein 1
BIN1	Bridging integrator 1
BSA	Bovine serum albumin
CD44	Cluster of differentiation 44
CDK	Cyclin-dependent kinase
CED	Convection-enhanced delivery
COMAT	Cerebral organoid maturation medium
DAPI	4′,6-diamidino-2-phenylindole
DIPG	Diffuse intrinsic pontine glioma
DMEM/F-17	Dulbecco's modified eagle medium/nutrient mixture *F*-12
DMG	Diffuse midline glioma
DMSO	Dimethylsulfoxid
DRD2	Dopamine receptor D2
EB	Embryoid body
ECM	Extracellular matrix
FFPE	Formalin-fixed paraffin-embedded tissue
GBO	Glioblastoma organoids
GFAP	Glial fibrillary acidic protein
GLICO	Glioblastoma corticoid
HDAC	Histone deacetylase
HDACi	Histone deacetylase inhibitor
HSP90	Heat shock protein 90
HMTI	High-multiplexed tissue imaging
IF	Immunofluorescence
iPSC	Induced pluripotent stem cells
KI67	Kiel antigen no. 67
mTOR	Mammalian target of rapamycin
NAD+	Nicotinamide adenine dinucleotide recycling
NAMPT	Nicotinamide phosphoribosyltransferase

OC-like	Oligodendrocytic-like
OPC-like	Oligodendrocyte precursor cell-like
PBS	Phosphate buffered saline
PCNA	Proliferating cell nuclear antigen
PDGFRα	Platelet-derived growth factor receptor α
PDX	Patient-derived xenograft
PFA	Paraformaldehyde
pHGG	Pediatric high-grade glioma
PI3K	Phosphoinositide 3-kinase
PRC2	Polycomb repressive complex 2
RNA-seq	Ribonucleic acid-sequencing
RT	Radiation therapy
scRNA-seq	Single cell RNA-sequencing
SIRT2	Sirtuin 2
SOX10	SRY-box transcription factor 10
TSM	Tumor stem media

1. Introduction

Tumors in the central nervous system (CNS) are the second most common cancer type worldwide among children under 14 years of age according to the Global cancer statistics 2020 from the International Agency for Research on Cancer (GLOBOCAN, 2020; Figure 1). This group of cancers is associated with high mortality, whereby the exact location and type of tumor are critical to the prognosis of disease progression. In particular, malignant tumors in the brain are difficult to treat and represent the leading cause of childhood death in Germany (Kyu et al., 2018). Among these, pediatric high-grade gliomas (pHGG) are one of the most diagnosed brain tumors in children (Sturm et al., 2017) with a diffuse and infiltrative growth pattern. According to the latest WHO classification from 2021, pediatric-type diffuse HGGs are mainly distinguished by their histone mutation status (Louis et al., 2021). This work specifically addresses H3K27-altered diffuse midline gliomas (DMGs) and further details on this tumor subtype are provided in the following section.

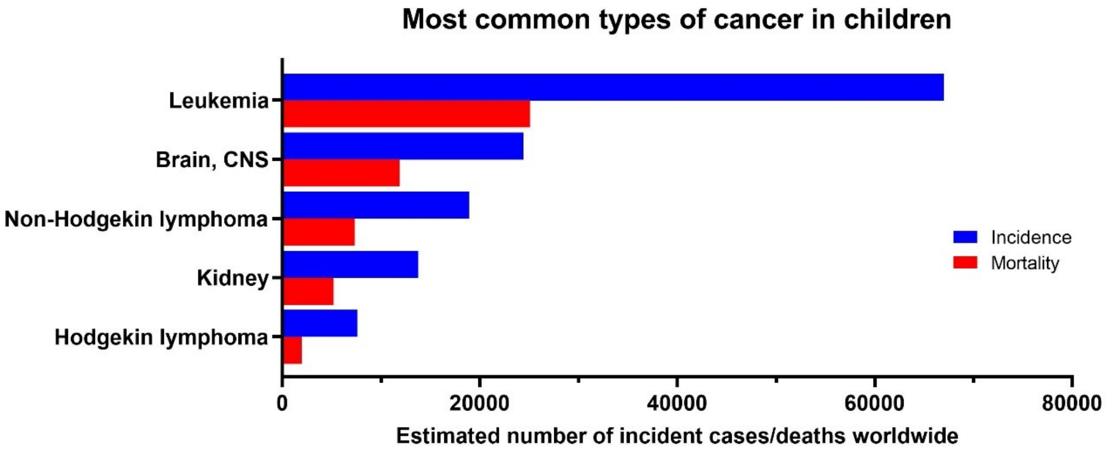

Figure 1: The five most common tumor types in children. The graph shows incidence and mortality based on tumor location in both sexes and in the age range of 0-14 worldwide. Data for the figure are taken directly from the international Agency for Research on Cancer`s Global Cancer Observatory website (GLOBOCAN 2020; http://gco.iarc.fr).

1.1 H3K27-altered diffuse midline gliomas

Diffuse midline gliomas are a particularly aggressive pediatric type of cancer located in the midline structures of the brain. They account for approximately 10 % - 20 % of newly diagnosed CNS tumors in children and mostly occur in the brain stem (Patil et al., 2021). For a long time, relatively little was known about the biology of these tumors as risks of taking biopsies were too high and tumor material was rare. Sequencing studies from 2012 provided the first insights into the genomic alterations of the tumor (Khuong-Quang et al., 2012; Schwartzentruber et al., 2012; Wu et al., 2012) and identified the characteristic point mutation in histone 3. The vast majority of DMGs harbors this driver mutation at position 27 in the histone 3 gene variants H3.1 and H3.3 (Sturm et al., 2017), resulting in a lysine to methionine substitution (H3K27M) (Khuong-Quang et al., 2012). This H3K27-alteration inhibits the polycomb repressive complex 2 (PRC2), thus impairing epigenetic repression by a global reduction of trimethylation and potentially leading to altered cell differentiation (Buczkowicz et al., 2014; Funato et al., 2014; Lewis et al., 2013; Sturm et al., 2014). Notably, the pontine localization of H3K27M tumors is associated with a particular poor prognosis in patients. Tumors at this location were previously called diffuse intrinsic pontine glioma (DIPG) and are now encompassed within the H3K27-altered diffuse midline glioma category (Louis et al., 2021). With a median age at diagnosis of 6.8 years and a median survival rate of only 11 months, DMGs with pontine localization are the leading cause of brain tumor-related death in childhood (Buczkowicz & Hawkins, 2015; Hoffman et al., 2018). Among other factors, only a patient age of ≤3 years and a longer symptom duration at diagnosis are considered predictors of a slightly better prognosis (Broniscer et al., 2008; Ueoka et al., 2009). The H3K27 mutation in DMGs is often accompanied by partner driver alterations in genes such as ACVR1, FGFR1, PDGFRα, PIK3CA, PTEN, MYC and TP53, further contributing to tumor aggressiveness (Fontebasso et al., 2014; Funato et al., 2014; Nikbakht et al., 2016; Paugh et al., 2013; Taylor et al., 2014).

New insights have also been gained in the field of intratumoral heterogeneity in recent years. Filbin et al. identified distinct tumor cell populations in H3K27M-gliomas (Filbin et al., 2018). In addition to a more de-differentiated oligodendrocyte precursor cell population (OPC-like), more differentiated oligodendrocytic (OC-like) and astrocytic (AC-like) tumor cells were found with each subpopulation showing expression patterns of marker proteins. OPC-like cells represented a more stem-like (dedifferentiated and cycling) population that potentially self-renews and gives rise to the other subpopulations. In a publication from 2022, all H3K27M-glioma subpopulations were analyzed in context of exact tumor location (Liu et al., 2022). Site specificity was found for OPC-like tumor cells, which are increased in the pons in a more immature pre-OPC-like state compared to other midline structures such as the thalamus. This may also contribute to the particular poor prognosis of H3K27-altered DMGs with pontine localization.

1.2 Current treatment strategies for H3K27-altered DMGs

The delicate and difficult-to-access location of the tumor in the midline structures of the brain, as well as the diffuse growth into nearby brain areas, severely limit the surgical removal of H3K27-altered DMGs. Important insights into the biological nature of H3K27-altered DMGs have only been gained in recent years and this knowledge has formed the basis for a variety of therapeutic ideas. Preclinical testing has led to the identification of potentially interesting drug candidates, however, despite all efforts, the minority of compounds prolonged survival of the young patients (Kluiver et al., 2020). Hypofractionated radiation therapy showed no benefit in comparison to conventional radiation therapy (RT) but allowed patients to achieve rapid symptom relief and a shorter hospital stay (Janssens et al., 2009). Efforts to enhance radiation effects further through the use of chemotherapeutic interventions showed no clear advantage (Jansen et al., 2015). Therefore, fractionated RT with adjuvant temozolomide remains the standard treatment, prolonging overall survival only by a few months (El-Khouly et al., 2019; Gallitto et al., 2019; Leszczynska et al., 2021).

Despite many drawbacks, a number of clinical trials are planned or ongoing to identify new treatment options for pediatric H3K27-altered DMGs (Dalle Ore et al., 2023). The recurrent H3K27-mutation in DMGs induces a global hypomethylation through the inhibition of the methyltransferase PCR2 (Bender et al., 2013; Lewis et al., 2013), which negatively affects gene expression. To counteract this epigenetic dysregulation, HDAC inhibitors (HDACi) have become an important research focus in the field of H3K27-altered DMGs. By inhibiting HDACs, the compounds are able to increase histone acetylation, leading to a reduction of tightly wound heterochromatin and allowing gene expression in the affected regions (G. Li et al., 2020). Thus, the HDAC inhibitor panobinostat showed promising effects in preclinical studies and was moved to phase I and II clinical trials (Aziz-Bose & Monje, 2019; Grasso et al., 2015). Also, PI3K and mTOR inhibitors are under investigation for the treatment of H3K27-altered DMGs. Early genetic analysis revealed frequent amplifications in the RTK-Ras-PI3K-AKT signaling network in H3K27-altered DMGs and affected members of this pathway emerged as potential therapeutic targets (Paugh et al., 2011; Zarghooni et al., 2010). Due to multiple compensatory mechanisms of single protein inhibition of this signal pathway, the development of dual inhibitors was advanced (Chang et al., 2019; Wright et al., 2021). Structural similarities of the kinase domains of phosphoinositide 3-kinase (PI3K) and mammalian target of rapamycin (mTOR), further led to the development of PI3K/mTOR inhibitors (Wright et al., 2021; H. Yang et al., 2013). The most promising member of this inhibitor class in the field of brain tumor treatment is paxalisib due to its preclinical tumor-reducing activity *in vivo* and its ability to cross the blood-brain barrier (BBB) at concentrations with moderate toxic side effects in glioblastoma patients (Heffron et al., 2016; Wen et al., 2020). Furthermore, the FDA awarded the orphan drug designation to paxalisib for rare childhood brain cancers in 2022, which supports the possible market launch of the drug decisively (BioSpace, 2022). Clinical trials have been initiated to evaluate the efficacy of the drug in patients with H3K27-altered DMGs as single agent treatment or in combination therapy (Table 1: NCT03696355, NCT05009992). Another promising therapeutic approach in H3K27-altered DMGs is the use of dopamine receptor 2 (DRD2) antagonists. DRD2, a G protein-coupled receptor, is known to stimulate tumor growth and has been identified as a potential therapeutic target in brain cancers which overexpress the receptor, including H3K27-altered DMGs (Aziz-Bose & Monje, 2019; J. Li et al., 2014). To counteract this upregulated receptor activity, the selective DRD2 antagonist ONC201, which belongs to the group of imipridones, was tested by several research groups. Preclinical and clinical studies suggested, that ONC201 is able to cross the BBB and first clinical experiences showed objective tumor responses in H3K27-altered DMGs with well tolerated doses (Allen et al., 2013; Arrillaga-Romany et al., 2020; Chi et al., 2019; Hall et al., 2019). Thereby, intratumoral concentrations of 600 nM to 9,3 µM were achieved with a weekly oral administration of the drug (Arrillaga-Romany et al., 2020). Currently, phase II and III studies are ongoing to further test the efficacy of ONC201 alone or in combination with other agents in H3K27-altered DMG patients (Table1: NCT05009992, NCT05476939 and NCT02525692). Phase II and III trials (also for combination therapy) in DMGs are currently running (NCT05009992, NCT05476939, NCT02525692 in Table 1). In addition, phase I trials with the promising ONC201-analogue ONC206 are conducted or start in 2023 for newly diagnosed and recurrent DMGs (NCT04541082, NCT04732065 in Table 1). Other therapeutical approaches are also in the focus of clinical studies and an overview of these trials is provided in Table 1.

Table 1: Current clinical trials for H3K27-altered DMGs. For each trial, the NCT identifier, phase, current status and treatment, as well as patient age are listed. The clinical trial registry page clinicaltrials.gov (accessed in March 2023) was searched to find ongoing or recently finished (in 2022) trials.

Study title and NCT identifier:	**Phase:**	**Status:**	**Treatment:**	**Age (years):**
Non-Invasive Focused Ultrasound (FUS) With Oral Panobinostat in Children With Progressive Diffuse Midline Glioma (DMG) (**NCT04804709**)	I	Active, not recruiting	Drug: **Panobinostat** (HDAC inhibitor); Device FUS	4-21
Phase I Study of Marizomib + Panobinostat for Children With DIPG (**NCT04341311**)	I	Active, not recruiting	Drug: **Marizomib** (proteasome inhibitor), **Panobinostat** (HDAC inhibitor)	0-21
Study of GDC-0084 in Pediatric Patients With Newly Diagnosed Diffuse Intrinsic Pontine Glioma or Diffuse Midline Gliomas (**NCT03696355**)	I	Completed	Drug: **Paxalisib** (PI3K/mTOR inhibitor); **Radiation therapy**	2-21
Combination Therapy for the Treatment of Diffuse Midline Gliomas (**NCT05009992**)	II	Recruiting	Drug: **ONC201** (DRD2 antagonist), **Paxalisib** (PI3K/mTOR inhibitor), **Panobinostat** (HDAC inhibitor); **Radiation therapy**	2-39
Trial of Panobinostat in Children With Diffuse Intrinsic Pontine Glioma (PBTC-047) (**NCT02717455**)	I	Active, not recruiting	Drug: **Panobinostat** (HDAC inhibitor)	2-21
Gemcitabine in Newly Diagnosed Diffuse Intrinsic Pontine Glioma (**NCT02992015**)	I	Recruiting	Drug: **Gemcitabine** (antimetabolite)	3-17
Biological Medicine for Diffuse Intrinsic Pontine Glioma (DIPG) Eradication 2.0 (**NCT05476939**)	III	Recruiting	Drug: **ONC201** (DRD2 antagonist), **Everolimus** (mTOR inhibitor); **Radiotherapy**	>= 6 months
A Study of Ribociclib and Everolimus Following Radiation Therapy in Children With Newly Diagnosed Non-biopsied Diffuse Pontine Gliomas (DIPG) and RB+ Biopsied DIPG and High-grade Gliomas (HGG) (**NCT03355794**)	I	Completed	Drug: **Ribociclib** (CDK inhibitor), **Everolimus** (mTOR inhibitor)	1-30
Fimepinostat in Treating Brain Tumors in Children and Young Adults (**NCT03893487**)	I	Active, not recruiting	Drug: **Fimepinostat** (PI3K/HDAC inhibitor)	3-39

Table 1 continued

Study title and NCT identifier:	**Phase:**	**Status:**	**Treatment:**	**Age (years):**
Abemaciclib in Children With DIPG or Recurrent/Refractory Solid Tumors (AflacST1501) (**NCT02644460**)	I	Recruiting	Drug: **Abemaciclib** (CDK inhibitor)	2-15
Adavosertib and Local Radiation Therapy in Treating Children With Newly Diagnosed Diffuse Intrinsic Pontine Gliomas (**NCT01922076**)	I	Completed	Drug: **Adavosertib** (WEE1 inhibitor); **Radiation therapy**	3-21
Phase I Study of Oral ONC206 in Recurrent and Rare Primary Central Nervous System Neoplasms (**NCT04541082**)	I	Recruiting	Drug: **ONC206** (DRD2 antagonist)	>= 18
Oral ONC201 in Recurrent GBM, H3 K27M Glioma, and Midline Glioma (**NCT02525692**)	II	Active, not recruiting	Drug: **ONC201** (DRD2 antagonist)	>= 16
ONC206 for Treatment of Newly Diagnosed, or Recurrent Diffuse Midline Gliomas, and Other Recurrent Malignant CNS Tumors (PNOC 023) (**NCT04732065**)	I	Recruiting	Drug: **ONC206** (DRD2 antagonist); Radiation therapy	2-21
Stereotactic Biopsy Split-Course Radiation Therapy in Diffuse Midline Glioma, SPORT-DMG Study (**NTC05077735**)	II	Recruiting	**Hypofractionated radiation** therapy	>= 1
Diffuse Intrinsic Pontine Glioma (DIPG) Reirradiation (ReRT) (**NCT01469247**)	I/II	Completed	**Radiation therapy**	0-17
CAR T Cells to Target GD2 for DMG (**NCT05544526**)	I	Not yet recruiting	Biological: **GD2 CAR T cells**	2-16
Genetically Modified Cells (KIND T Cells) for the Treatment of HLA-A*0201-Positive Patients With H3.3K27M-Mutated Glioma (**NCT05478837**)	I	Not yet recruiting	Biological: Autologous **Anti-H3.3K27M TCR-expressing T-cells**; Drugs: Cyclophosphamide (alkylating agent), Fludarabine (nucleotide analog)	3-21
Clinical Trial to Assess the Safety and Efficacy of AloCELYVIR With Newly Diagnosed Diffuse Intrinsic Pontine Glioma (DIPG) in Combination With Radiotherapy or Medulloblastoma in Monotherapy (AloCELYVIR) (**NCT04758533**)	I/II	Recruiting	Biological: **AloCELYVIR** (mesenchymal stem cells with oncolytic adenovirus); **Radiation therapy**	1-21
131I-omburtamab Delivered by Convection-Enhanced Delivery in Patients With Diffuse Intrinsic Pontine Glioma (**NCT05063357**)	I	Not yet recruiting	Biological: **131I-omburtamab** (radiolabeled antibody); Device: Convection Enhanced Delivery	3-21

Table 1 continued

Study title and NCT identifier:	**Phase:**	**Status:**	**Treatment:**	**Age (years):**
Nimotuzumab in Combined With Concurrent Radiochemotherapy in the Treatment of Newly Diagnosed Diffuse Intrinsic Pontine Glioma (DIPG) in Children (**NCT04532229**)	III	Recruiting	Biological: **Nimotuzumab** (anti-EGFR antibody); **Radiation therapy**	3-15
Brain Stem Gliomas Treated With Adoptive Cellular Therapy During Focal Radiotherapy Recovery Alone or With Dose-intensified Temozolomide (Phase I) (BRAVO) (**NCT03396575**)	I	Recruiting	Biological: **TTRNA-DC vaccine**, HSC; Drug: **Cyclophosphamide** (alkylating agent), **Fludarabine** (nucleotide analog), **Temozolomide** (alkylating agent)	3-30
A Study of Low Dose Bevacizumab With Conventional Radiotherapy Alone in Diffuse Intrinsic Pontine Glioma (**NCT04250064**)	II	Recruiting	Biological: **Bevacizumab** (anti-VEGF antibody); Ultra-low-dose **radiation therapy**	3-18
Expanded Access to OKN-007 for Patients With Diffuse Midline Glioma, H3 K27-altered (NCT05518838)	Expanded access	Available	Drug: **OKN-007** (gene regulating small molecule)	1-18
A Study of BXQ-350 in Children With Newly Diagnosed Diffuse Intrinsic Pontine Glioma (DIPG) or Diffuse Midline Glioma (DMG) (**NCT04771897**)	I	Recruiting	Drug: **BXQ-350** (synthetic lysosomal protein targeting phosphatidylserine (PS) lipids)	1-30
Blood-brain Barrier (BBB) Disruption Using Exablate Focused Ultrasound With Doxorubicin for Treatment of Pediatric DIPG (**NCT05630209**)	I/II	Recruiting	Drug: **Doxorubicin** (antracycline); Device: Exablate	5-21
Pediatric Trial of Indoximod With Chemotherapy and Radiation for Relapsed Brain Tumors or Newly Diagnosed DIPG (**NCT04049669**)	II	Recruiting	Drug: **Indoximod** (IDO/TDO inhibitor), **Temozolomide** and **Cyclophosphamide** (alkylating agents), **Etoposide** (topoisomerase inhibitor**), Lomustine** (alkylating agent); **Radiation therapy**	3-21
rHSC-DIPGVax Plus Checkpoint Blockade for the Treatment of Newly Diagnosed DIPG and DMG (**NCT04943848**)	I	Recruiting	Biological: **rHSC-DIPGVax** (off-the-shelf neo-antigen heat shock protein); Biologicals: **Balstilimab** (anti-PD-1 antibody), **Zalifrelimab** (anti-CTLA4 antibody)	1-18
PEP-CMV Vaccine Targeting CMV Antigen to Treat Newly Diagnosed Pediatric HGG and DIPG and Recurrent Medulloblastoma (**NCT05096481**)	II	Not yet recruiting	Biological: **PEP-CMV vaccine**; Drug: **Temozolomide** (alkylating agent)	3-25

Table 1 continued

Study title and NCT identifier:	**Phase:**	**Status:**	**Treatment:**	**Age (years):**
A Phase 1/2 Study of Sonodynamic Therapy Using SONALA-001 and Exablate 4000 Type 2 in Patients With DIPG (**NCT05123534**)	II	Recruiting	Combination product: **SONALA** (ALA), MRgFUS (MR-guided ultrasound device)	>= 5
PEACH TRIAL- Precision Medicine and Adoptive Cellular Therapy (PEACH) (**NCT04837547**)	I	Recruiting	Biological: **TTRNA-xALT** (Tumor-specific ex vivo expanded autologous lymphocyte transfer)	1-30
Vorinostat and Temsirolimus With or Without Radiation Therapy in Treating Younger Patients With Newly Diagnosed or Progressive Diffuse Intrinsic Pontine Glioma (**NCT02420613**)	I	Active, not recruiting	Drug: **Temsirolimus** (mTOR inhibitor), **Vorinostat** (HDAC inhibitor)	7 months - 21 years
H3.3K27M Peptide Vaccine With Nivolumab for Children With Newly Diagnosed DIPG and Other Gliomas (**NCT02960230**)	I/II	Active, not recruiting	Biological: **K27M peptide**; Drug: **Nivolumab** (anti-PD-1 antibody)	3-21
A Study of the Drug Selinexor With Radiation Therapy in Patients With Newly Diagnosed Diffuse Intrinsic Pontine (DIPG) Glioma and High-Grade Glioma (HGG) (**NCT05099003**)	I/II	Recruiting	Drug: **Selinexor** (XPO1 inhibitor); **Radiation therapy**	1-21
CBL0137 for the Treatment of Relapsed or Refractory Solid Tumors, Including CNS Tumors and Lymphoma (**NCT04870944**)	I/II	Active, not recruiting	Drug: **CBL0137** (FACT complex inhibitor)	1-30
Oral AMXT 1501 Dicaprate in Combination With IV DFMO (**NCT05500508**)	I/II	Recruiting	Drug: **AMXT1501** (polyamine transport inhibitor), **DFMO** (ODC inhibitor)	>= 12
Pembrolizumab in Treating Younger Patients With Recurrent, Progressive, or Refractory High-Grade Gliomas, Diffuse Intrinsic Pontine Gliomas, Hypermutated Brain Tumors, Ependymoma or Medulloblastoma (**NCT02359565**)	I	Recruiting	Biological: **Pembrolizumab** (anti-PD1 antibody)	1-29
Study of B7-H3-Specific CAR T Cell Locoregional Immunotherapy for Diffuse Intrinsic Pontine Glioma/Diffuse Midline Glioma and Recurrent or Refractory Pediatric Central Nervous System Tumors (**NCT04185038**)	I	Recruiting	Biological: **SCRI-CARB7H3**(s) (B7H3-specific chimeric antigen receptor (CAR) T cells)	1-26

Table 1 continued

Study title and NCT identifier:	**Phase:**	**Status:**	**Treatment:**	**Age (years):**
A Phase 1b Study of PTC596 in Children With Newly Diagnosed Diffuse Intrinsic Pontine Glioma and High-grade Glioma (**NCT03605550**)	I	Recruiting	Drug: **PTC596** (BMI-1 inhibitor)	1-21
Dose Escalation Study of CLR 131 in Children, Adolescents, and Young Adults With Relapsed or Refractory Malignant Tumors Including But Not Limited to Neuroblastoma, Rhabdomyosarcoma, Ewings Sarcoma, and Osteosarcoma (CLOVER-2) (**NCT03478462**)	I	Recruiting	Drug: **CLR131** (small-molecule phospholipid iodine-131 conjugate)	2-25
A Phase I Study of Mebendazole for the Treatment of Pediatric Gliomas (**NCT01837862**)	I/II	Recruiting	Drug: **Mebendazole** (anthelmintic), **Vincristine** (cytostatic agent), **Carboplatin** (cytostatic agent), **Temozolomide** (alkylating agent), **Irinotecan** (topoisomerase inhibitor); Biological: **Bevacizumab** (anti-VEGF antibody)	1-21
INCB7839 in Treating Children With Recurrent/Progressive High-Grade Gliomas (**NCT04295759**)	I	Recruiting	Drug: **INCB7839** (ADAM inhibitor)	3-21
Phase I Study of APX005M in Pediatric CNS Tumors (**NCT03389802**)	I	Recruiting	Biological: **APX005M** (CD40 agonist antibody)	1-21
Phase I Study of Mebendazole Therapy for Recurrent/Progressive Pediatric Brain Tumors (**NCT02644291**)	I	Completed	Drug: **Mebendazole** (anthelmintic)	1-21
A Study of Cabozantinib as a Maintenance Agent to Prevent Progression or Recurrence in High-Risk Pediatric Solid Tumors (**NCT05135975**)	II	Recruiting	Drug: **Cabozantinib** (tyrosine kinase inhibitor)	18 months-40 years
A MultIceNTER Phase I Peptide Vaccine Trial for the Treatment of H3-Mutated Gliomas (INTERCEPT-H3) (**NCT04808245**)	I	Recruiting	Biological: **H3K27M peptide vaccine**, **Tecentriq** (anti-PD-L1 antibody); Drug: **Imiquimod** (virostatic agent)	>= 18
International Cooperative Phase III Trial of the HIT-HGG Study Group (HIT-HGG-2013) (HIT-HGG-2013) (**NCT03243461**)	III	Recruiting	Drug: **Temozolomide** (alkylating agent), **Valproic acid** (HDAC inhibitor)	3-17
C7R-GD2.CAR T Cells for Patients With GD2-expressing Brain Tumors (GAIL-B) (**NCT04099797**)	I	Recruiting	Biological: **(C7R)-GD2.CART cells**, Drugs: **Cyclophosphamide** (alkylating agent), **Fludarabine** (nucleotide analog)	1-21

Table 1 continued

Study title and NCT identifier:	**Phase:**	**Status:**	**Treatment:**	**Age (years):**
A Study of Pomalidomide Monotherapy for Children and Young Adults With Recurrent or Progressive Primary Brain Tumors (**NCT03257631**)	II	Active, not recruiting	Drug: **Pomalidomide** (immune modulator)	1-21
A Study of Bempegaldesleukin (BEMPEG: NKTR-214) in Combination With Nivolumab in Children, Adolescents and Young Adults With Recurrent or Treatment-resistant Cancer (PIVOT IO 020) (**NCT04730349)**	I/II	Completed	Biological: **Nivolumab** (anti-PD-1 antibody), **NKTR-214** (IL2 pathway agonist)	0-30

1.3 Model systems for drug testing in pediatric brain tumors

Disease-specific models such as laboratory animals or cell culture-based systems are essential for preclinical testing of new drug candidates. In recent years, a variety of approaches have been followed for model development, from which the most important in the field of pediatric brain tumors are outlined in more detail below.

1.3.1 H3K27-altered DMG cell lines

Culturing tumor cells to evaluate the efficacy of new therapies is an essential component of current drug testing (Mirabelli et al., 2019). There is a large number of established and well-characterized cell lines available for multiple cancer types. Generating cell lines from pediatric brain tumors has been particularly difficult in the past and it was only after 2000 that there was increasing success in this area, largely due to the use of neurosphere culture (Xu et al., 2015). This culture method allows tumor cells to grow in a 3D-like manner, which preserves tumor-specific gene expression profiles and maintains their tumor-initiating potential. But important factors like the tumor microenvironment (TME) are missing and artificial cell culture conditions can lead to the selection of specific tumor subpopulations (Caragher et al., 2019). Nevertheless, cell lines are particularly valuable for tumor entities with limited tissue availability, like H3K27-alterd DMG. The successful establishment of a patient-derived cell line in this case was first reported in 2011 (Monje et al., 2011). The introduction of biopsy sampling in young DMG patients led to an increase in patient-derived cell lines (Z. Li & Langhans, 2021) and a detailed protocol for cell line generation from autopsy tissue was published in 2017 (Lin & Monje, 2017). The cultivation of DMG cells from biopsy or autopsy samples enabled high-throughput drug testing to identify interesting drug candidates for subsequent clinical trials (Lin et al., 2019).

1.3.2 Orthotopic patient derived xenograft mouse models of H3K27-altered DMGs

Brain tumor xenograft models involve the growth of human brain cancer cells in immunodeficient mice. The intercranial orthotopic injection of tumor cells allows tumor growth in the anatomical site of the mouse brain corresponding to the tumor origin and embeds cells into a specific brain-like TME. These mouse models have contributed significantly to the current knowledge of tumorigenesis and have become an essential component in the development of safe and effective antitumor therapies (Singh & Seed, 2021). Orthotopic patient-derived xenograft (PDX) are of special importance, since a microenvironment that differs from the original anatomical location of the tumor can decisively alter the properties of cancer cells (Katsuta et al., 2020). Since Monje et al., 2011 established biopsy and autopsy samples as cell sources for the first H3K27-altered DMG PDX model system, many orthotopic PDX models have been developed (Harutyunyan et al., 2019; Piunti et al., 2017; Tsoli et al., 2019). These have been used for preclinical testing of promising drug candidates such as panobinostat, marizomib and ONC201 (Duchatel et al., 2021; Lin et al., 2019), providing the data needed for the initiation of clinical trials. In addition to specific antitumor effects, orthotopic PDX models can be used to analyze important parameters for drug use in brain tumor patients, such as BBB permeability and organ-specific toxicities (Hennika et al., 2017). Therefore, the use of the model system is a valuable tool in preclinical drug testing, however, the complex and time-consuming procedure of model generation limits its application in larger drug screens. Furthermore, high variabilities in DMG-PDX generation protocols complicates the comparison of results between different laboratories and between the model and the actual tumor, which led to recent and initial efforts toward standardization of protocols (’t Hart et al., 2023).

1.3.3 Brain tumor organoids

Organoids are playing an increasingly important role in brain tumor research (Z. Li & Langhans, 2021) and the groundwork for their use was done in 2016. Hubert et al. embedded glioblastoma cells from tumor resections into matrigel, which resulted in the formation of glioblastoma organoids (GBO) within a few weeks. To better model the highly invasive growth of glioblastoma cells and to provide a human-like TME, developing cerebral organoids (derived from human embryonic stem cells) were combined with glioblastoma spheres for the first time in 2018 (da Silva et al., 2018). Tumor cells spontaneously infiltrated the organoid, resulting in the formation of glioblastoma corticoids (GLICO). GLICOs exhibited key features of the primary tumor and were therefore used for therapy testing (Linkous et al., 2019). Interestingly, tumor cells grown in the microenvironment of cerebral organoids showed similar resistances to treatments as seen in patients that were absent in conventional 2D cell culture testing. It should be noted, however, that due to the *in vitro* nature of the organoid model system, important physiological components of the brain such as the blood-brain barrier and immune cells are not represented. Nevertheless, the aforementioned realistic response of tumor cells to drugs makes the co-culture model particularly interesting for therapeutic research in childhood brain tumors, which respond poorly to drugs in the clinic as well. To date, there are only a few organoid models of pediatric brain tumors used in research, which particularly concerns pHGGs (Riedel et al., 2022). In the case of H3K27-altered DMGs, there is currently no co-culture model of tumor cells with cerebral organoids available.

1.4 Characterizing tumor tissues and model systems with multiplexed fluorescence imaging

Genomic instability and external environmental conditions lead to a very heterogenous composition of tumor cells in cancer (McGranahan & Swanton, 2017). The emergence and increased use of single-cell analysis, such as single-cell sequencing (RNA or DNA), has helped to also capture the intratumoral heterogeneity in case of DMGs (Nicholson & Fine, 2021). Current single-cell sequencing protocols require the prompt dissociation of freshly collected tissue into single cells, followed by extraction, amplification, and sequencing of DNA or RNA from each cell (Tang et al., 2019). However, the availability of fresh tissue is extremely limited for rare tumor types such as H3K27-altered DMGs that are not treated surgically. The emergence of high-multiplexed tissue imaging (HMTI) in recent years (Einhaus et al., 2023) now allows single-cell analysis of formalin-fixed paraffin-embedded tissue (FFPE), which is more readily available. CO-Detection by indEXing (CODEX) is one of the more recent developments in HMTI and uses DNA oligonucleotide-coupled antibodies that are sequential detected with complementary fluorophore-coupled DNA oligonucleotides (reporters) for protein detection (Black et al., 2021). A detailed method overview is provided in Figure 2. First, suitable antibodies are conjugated with a unique nucleotide-based barcode. FFPE tissue sections can then be stained with a panel of up to 60 antibodies at a time and antibodies are permanently fixed to the tissue. Detection is performed in iterative cycles, with three reporters hybridized, detected and dehybridized per cycle. As many cycles are performed in sequence as necessary to detect all antibodies and the respective proteins. Within the resulting whole-slide image, individual cell segments can be determined, and each individual cell can thus be characterized on the basis of individual protein signals from antibody detection. This means that not only more cells can be characterized at once than with conventional sequencing methods, but also that the tissue architecture is preserved, and spatial aspects can be analyzed. However, fewer markers can be examined at once and the choice of the right antibodies is very important for the analysis.

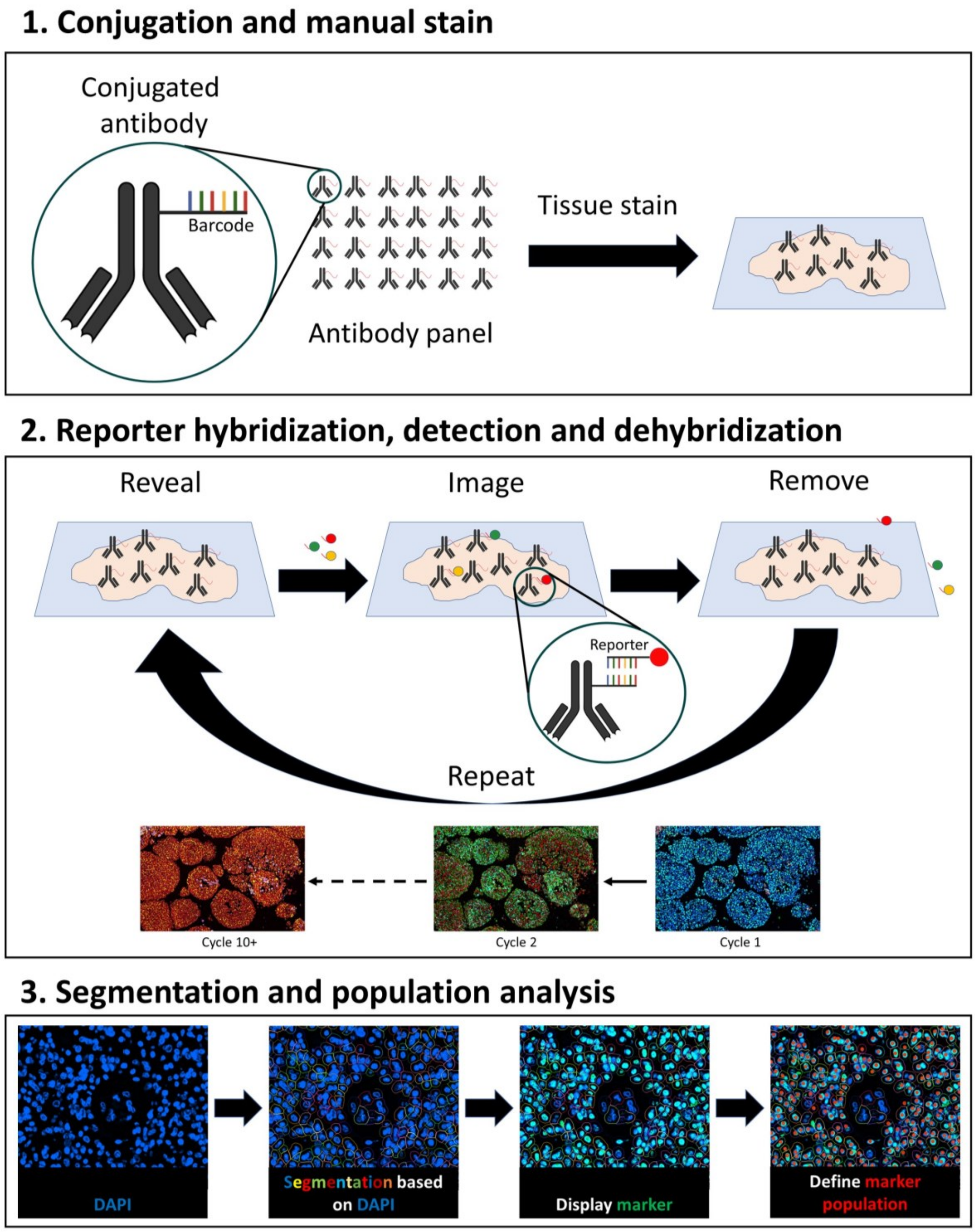

Figure 2: Co-Detection by indEXing (CODEX) procedure. **1**: Conjugation of antibodies with unique DNA barcodes. **2**: Cycle-wise detection of antibodies using complementary DNA reporters coupled with fluorophores. **3**: Marker population analysis based on the acquired fluorescence images.

1.5 Goal of this thesis

Modeling the therapeutic response of tumor cells *in vitro* is a complex and multifactorial task. Interactions between tumor cells and their microenvironment (e.g., non-malignant cells or extracellular matrix (ECM)) influence treatment resistance and progression of malignancies in the brain and must be addressed in 3D models (Da Ros et al., 2018; Langhans, 2018). Furthermore, tumors like H3K27-altered DMGs exhibit a heterogeneous tumor cell composition (Filbin et al., 2018; Liu et al., 2022), which further challenges the identification of treatments to which all subpopulations will respond sufficiently. Aim of this thesis was to develop a new *in vitro* model for drug testing, which provides a human brain-like TME for H3K27-altered DMG cells and exhibits a realistic tumor cell composition (see Figure 3). A protocol was developed to introduce tumor cells into developing cerebral organoids to model a human brain-like TME. To analyze tumor cell composition, the multiplex fluorescence CODEX system was established as part of this work. The generated model could thus be validated on the basis of single-cell analysis data through comparison to primary tumor samples and other commonly used model systems. In addition, a treatment protocol for drug testing was developed and the effects of promising drug candidates on tumor cells were analyzed based on decrease in tumor burden, proliferation inhibition and remaining tumor cell composition. By providing a new and realistic tumor model, this thesis was intended to increase the predictive power of preclinical drug screens for future treatment of H3K27-altered DMGs.

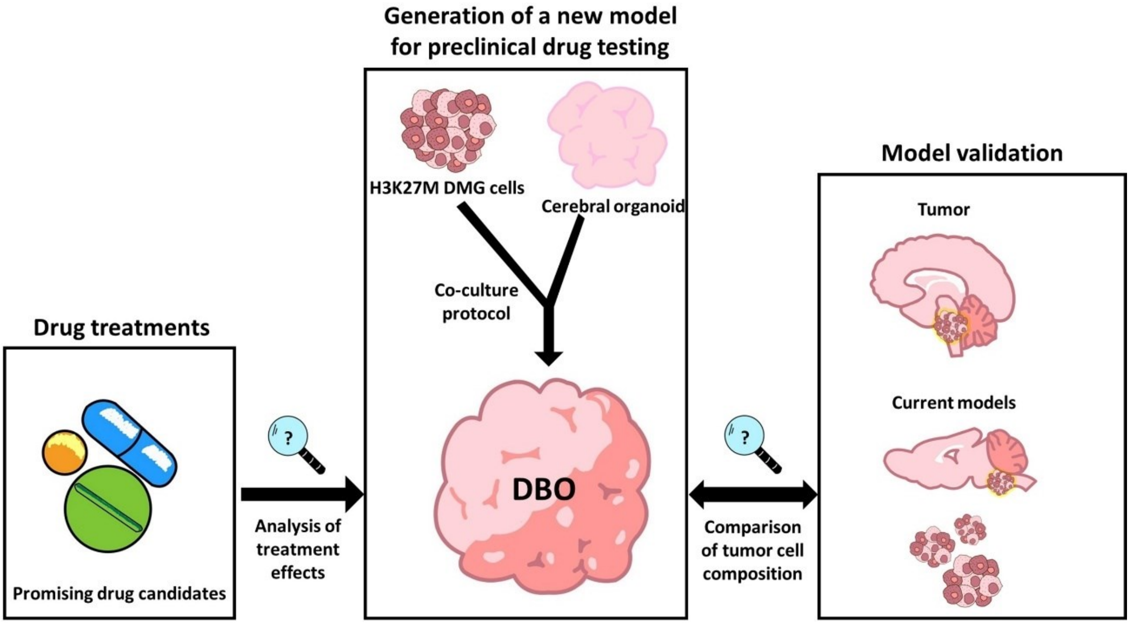

Figure 3: A new H3K27-altered DMG model for preclinical drug testing. H3K27M tumor cells were introduced into cerebral organoids to generate DMG brain organoids (DBO). The model system was validated by comparison (tumor cell composition) with primary tumor samples and other DMG models and used for analysis of treatment effects induced by promising drug candidates.

2. Material and Methods

2.1 Cell culture

2.1.1 DMG tumor cells

ZsGreen labeled H3.3K27-mutated BT869 cells were provided by the Ligon Lab (Dana-Farber Cancer Institute) and cultured as neurospheres in a humidified incubator at 37°C with 5 % CO_2 using vented T75 culture flasks. For complete culture medium, a base medium was first prepared (tumor stem media (TSM) Base), to which temperature-sensitive components were added immediately before use. The TSM Base medium consisted of a 1:1 mixture of Neurobasal-A medium and DMEM/-12. HEPES Buffer, MEM Sodium Pyruvate, MEM Non-essential Amino Acid, GlutaMax and Antibiotic-Antimycotic solutions were added to a 1x end concentration. TSM Base was then passed through a sterile 0,2 µm filter and stored at 4°C. For the complete culture medium (TSM Full), B-27 without vitamin A (1x working concentration) and growth factors EGF, FGF (20 ng/ml) and PDGF-AA, PDGF-BB (10 ng/ml) were supplemented to the base medium. Finally, heparin was added to a concentration of 2 µg/ml and the medium was strained through a sterile 0,2 µm filter. TSM Full medium was stored at 4°C and needed volumes were warmed up to 37°C immediately before use in the water bath. BT869 cells were regularly (every 2-3 days) supplied with fresh medium and split to avoid acidotic culture conditions. Therefore, a part of the cell suspension was aspirated and fresh, warmed TSM Full medium was carefully added to the remaining cells in the flask.

For cryopreservation, neurosphere suspension was removed from the flask and transferred in a 15 ml conical tube. After centrifugation for 3 min at 300x g, the supernatant was discarded, and the pellet was gently resuspended in cold freezing medium (TSM Base with 10 % DMSO) without destroying the tumor cell spheres. The suspension was then transferred to cryovials and frozen in a freezing container at -80°C. After two days cells were moved to storage boxes at -80°C. Usually one ml with a couple of million cells was frozen per cryovial.

For thawing cryopreserved cells, cryovials were retrieved from -80°C and quickly thawed at 37°C in a water bath. Thawed cells were carefully transferred in a 15 ml conical tube containing 9 ml of pre-warmed DMEM/F-12 and centrifuged at 300x g for 3 min. Supernatant was discarded and tumor spheres were gently resuspended in pre-warmed TSM Full. The suspension was transferred into a culture flask and incubated at 37°C and 5 % CO_2. Depending on thawed sphere numbers, T25 or T75 culture flasks were used with 8-15 ml TSM Full for culture initiation.

2.1.2 iPSC culture

The human induced pluripotent stem cell (iPSC) line HMGU (received from Helmholtz Center Munich) was cultured in mTesR Plus medium, using matrigel-coated 6-well plates under standard cell culture conditions (37°C, 5 % CO_2). When reaching 80 % confluency, iPSCs were passaged to ensure continuous cell growth. At least 3 h before passaging, 6-well plates were coated with matrigel. For this purpose, matrigel was thawed on ice and diluted 1:100 in cold DMEM/F-12. Typically, 1 ml of the matrigel-DMEM mixture was used to coat one well of the culture plate. The 6-well plates were then placed in the incubator and stored at 37°C until use. Coated wells were washed with warm DMEM/F-12 and 1,5 ml of pre-warmed mTesR Plus were added per well. iPSCs were retrieved from the incubator and consumed medium was removed. Cells were carefully washed with pre-warmed DMEM/F-12. After removing the washing solution, 1 ml ReLeSR was added per well to detach the cell colonies. After 30-40 sec of incubation at room temperature, ReLeSR was removed, iPSC plates were transferred to an incubator and incubated at 37°C for 7-10 min. 2 ml DMEM/F-12 were added per well using a 5 ml serological pipette to gently wash cells from the surface. Floating colonies were transferred to a conical tube and additional 5-20 ml of DMEM-F-12 were used to collect the entire well of iPSCs. After pelleting cells at 300x g for 5 min, the supernatant was aspirated, and the pellet was carefully resuspended in warm mTeSR Plus. 500 µl of cell suspension was transferred to each well of the 6-well plate to reach a final volume of 2 ml. The mTeSR Plus medium was changed every second day (2 ml) and double feedings of 4 ml mTeSR Plus per well were performed for longer incubation periods of maximum 3 days.

To freeze iPSCs, colonies were detached from wells as described above. After pelleting, colonies were resuspended in Bambanker freezing medium. Cell solutions were transferred to cryovials and placed in a freezing container. After two days at -80°C cryovials were placed in storage boxes at -80°C.

For thawing iPSCs, matrigel-coated 6-well plates were prepared as described above. After washing, 1,5 ml of warm mTeSR Plus were added per well along with 2 µl of 10 mM Rock inhibitor solution. iPSCs were removed from the -80°C freezer and quickly thawed in the water bath. The cell solution was then transferred to a 15 ml conical tube containing 10 ml pre-warmed DMEM/F-12. After pelleting at 300x g for 5 min, the supernatant was aspirated and warm mTeSR Plus was added to the pellet. By gently snapping the tube with fingers, the pellet was resuspended. 500 µl of iPSC solution was added per well of the 6-well plate to achieve a final volume of 2 ml with 10 µM Rock inhibitor. After 24 h medium was replaced with 2 ml of mTeSR Plus without Rock inhibitor, and the cells were cultured for further use.

2.1.3 DMG brain organoid generation

BT869 cells were co-cultured with cerebral organoids to form brain tumor organoids. An adapted protocol from Lancaster & Knoblich, 2014 by STEMCELL Technologies (STEMdiff Cerebral Organoid Kit) was used to differentiate cerebral organoids. To increase the quantity of DBO generation, the Assist Plus pipetting robot and multichannel pipettes from Integra were used. A schematic representation of the co-culture protocol is shown in Figure 8.

Day 0: Seeding of iPSCs for EB formation

At the start of the co-culture protocol, 50 ml of embryoid body (EB) formation medium were prepared by combining 40 ml Basal Medium I with 10 ml Supplement A to generate EBs out of iPSCs. To ensure survival of the HMGU iPSCs after seeding, EB seeding medium was prepared by adding 10 µM of Rock inhibitor to EB formation medium. iPSCs were used, when showing large colonies (confluency around 80 %) with smooth edges and dense centers. Medium was aspirated from cells and wells were washed with pre-warmed DMEM/F-12. After removing the wash solution, 1 ml of Gentle Cell Dissociation Reagent was added per well and iPSC plates were incubated at 37°C for 8-10 min. Using 1 ml of pre-warmed DMEM/F-12, cells were gently rinsed off and transferred to a conical tube. Wells were rinsed with additional milliliters of DMEM-F-12 and cells were added to the conical tube. After centrifugation at 300x g for 5 min, the supernatant was aspirated and iPSCs were resuspended in EB seeding medium. Cells were counted using a Countess cell counter. 9000 cells in 100 µl EB seeding medium were seeded per well of an ultra-low 96-well U-bottom plate using the Assist Plus Pipetting Robot. Plates were transferred to an incubator and left undisturbed for at least 24 h at 37°C. On day 2 and 4, 100 µl of EB formation medium were added per well and iPSCs formed EBs until day 5 with round, smooth edges.

Day 0: Tumor cell seeding

BT869 cells were transferred to a 50 ml conical tube and centrifuged for 5 min at 300x g. After aspirating the supernatant, cells were resuspended in 1 ml of TrypLE and incubated for 2-3 min at room temperature. 9 ml of pre-warmed DMEM/F-12 were added afterwards. To remove undissociated tumor spheres, the cell solution was strained though a 70 µm cell strainer and collected in a fresh 50 ml conical tube. The tube was centrifuged at 300x g for 5 min and the resulting supernatant was aspirated. After resuspending cells in 1 ml of warm TSM Full medium, cell numbers were measured with a Countess cell counter. 5000 cells in 100 µl TSM Full per well were seeded into an ultra-low 96-well U-bottom plate using the Assist Plus Pipetting Robot. Plates were placed in the incubator at 37°C and 100 µl of TSM Full per well were added on the following days 2 and 4. During this incubation time, BT869 cells formed one big tumor sphere per well.

Day 5: Neural induction in EBs

To induce neural ectoderm in EBs, 50 ml of induction medium was prepared by adding 0,5 ml Supplement B to 49,5 ml Basal Medium I. 300 µl of pre-warmed induction medium per well was transferred to a fresh ultra-low 96-well U-bottom plate. One EB per well was transferred (using wide bore tips) to the induction medium containing 96-well plate. Plates were cultivated at 37°C until day 7 and EBs developed optically translucent edges.

Day 7: Expansion of neuroepithelia in early cerebral organoids and co-culture start with tumor spheres

For expanding neuroepithelia in early cerebral organoids, 25 ml of cold expansion medium was prepared. 0,5 ml thawed matrigel (mechanical support for expansion), 0,5 ml Supplement D, together with 0,25 ml Supplement C were added to 24,25 ml of Basal Medium II. 245 µl expansion medium per well were transferred to a fresh ultra-low 96-well U-bottom plate. One EB and one tumor sphere were transferred to each well using wide bore pipetting tips. Plates were incubated at 37°C until day 10.

Day 10: DBO maturation

On day 10, early DBOs were embedded in matrigel to further support maturation and expansion of neuroepithelia. Therefore, matrigel was thawed on ice and organoid embedding sheets were placed in sterile 100 mm dishes. Before starting the embedding process, 6-well plates were filled with 3 ml of warm cerebral maturation medium (COMAT) per well. COMAT consists of a 1:1 mixture of Neurobasal-A medium and DMEM/F-12. Furthermore, GlutaMax, B-27, MEM Non-essential Amino Acid and N2 supplements were added to a final 1x concentration. After adding 2,5 µg/ml Insulin and 50 µM of 2-mercaptoethanol, the medium was strained through an 0,2 µm sterile filter. Using a pipette with wide bore tip, DBOs were carefully transferred to the embedding sheet and excess medium around DBOs was removed. To each, DBO 20 µl of matrigel was added. Organoids were then positioned in the center of the matrigel drop and sheets were incubated at 37°C for 10-15 min inside the petri dishes. To avoid early polymerization of the matrigel, a maximum of 12 organoids were embedded simultaneously. After solidification of the matrigel droplets, sheets were grasped with sterile tweezers and positioned over the COMAT-filled 6-well plates. DBOs were gently rinsed of the sheet with warm COMAT. An amount of six organoids were added per well. 6-well plates were incubated at 37°C for 24 h undisturbed and then placed on an orbital shaker in the incubator with constant shaking at 80 rpm. DBOs were cultivated on the shaker for at least 50 additional days. Organoids were checked regularly under the microscope. Medium was changed every 2-3 days using either TSM Full medium to support tumor cell growth or COMAT to promote organoid maturation.

2.2 DBO treatment scheme

Fully matured DBOs were thoroughly inspected to ensure good organoid quality. Drug treatment was performed in 6-well plates with three organoids and 3 ml COMAT medium per well. A total of 30 compounds was tested and the drug selection was based on a recent preclinical high-throughput drug screen with H3K27-alterd DMG cells (Lin et al., 2019). To further limit the number of drugs, potent compounds from this screening were assessed by most recent information available from clinical trials at onset of the project (planned or present use in DMG trials) and selected for DBO treatment. Two different concentrations per drug and the corresponding controls were tested. After distribution of DBOs to the wells, drugs were added in desired volumes and plates were stored at 37°C in an incubator under constant shaking (80 rpm). To ensure consistent drug potency and nutrient delivery over time, the medium was completely aspirated on day 4, 7 and 10 and replaced with fresh drug-added medium. DBOs were treated for 14 days. A detailed scheme of the treatment protocol is shown in Figure 12A.

2.3 Fixation and paraffin embedding

DBOs were directly transferred in biopsy embedding cassettes on treatment day 14. In contrast, BT869 spheres had to be matrigel embedded beforehand as following: Spheres were centrifuged at 300x g for 5 min and after aspiration of the supernatant, cells were carefully resuspended in thawed matrigel. Matrigel-sphere solution was gently pipetted on organoid embedding sheets and matrigel polymerized for 15 min at 37°C. Droplets were rinsed of the sheet and transferred to biopsy embedding cassettes. Cassettes containing DBOs or cell spheres were fixed in 4 % formaldehyde solution for 4-5 h and then transferred stepwise to liquid paraffin using a fatty tissue processor. For this purpose, the cassettes were incubated for 10 min each in 4 % formaldehyde, 70 % ethanol and three times in 96 % ethanol. This was followed by three incubations in 100 % isopropanol and two in 100 % xylene. Subsequently, the cassettes could be placed in heated liquid paraffin.

Using a modular tissue embedding station, heated molds were filled with liquid paraffin. Fixed material was carefully removed from cassettes and placed in the prepared molds. To solidify the paraffin, molds were placed on a cooling plate and left there undisturbed for 20-30 min. Paraffin blocks were carefully demolded and stored at room temperature.

Fixation and paraffin embedding was only performed for all DBO and DMG cell samples. Primary tissue and PDX samples were kindly provided as ready-to use paraffin blocks by the Filbin (Dana-Farber Cancer Institute, Boston) and Monje laboratories (Stanford university). The PDX sample was generated by intercranial, stereotactic injection of dissociated BT869 cells from sphere culture in the pons of 6-week-old female NSG^{TM} mice (Filbin laboratory).

2.4 Sample sectioning

For immunofluorescence staining, paraffin embedded samples were cut using a sledge microtome. Pre-cooled paraffin blocks were sectioned with a thickness of 2.5 µm. The sections were transferred to a warm water bath (45°C) using moistened paper strips. Floating sections smoothed out on the warm water surface and were carefully mounted on slides. Special care was taken to ensure that no water inclusions formed between slide and paraffin section, otherwise the sample would detach more easily during staining. After an overnight incubation at 60°C, slides were ready for antibody staining. In case of all DBO samples, one representative section from the thickest/middle part was used per DBO for staining (for immunofluorescence microscopy and CODEX). To avoid using more than necessary of the valuable/rare samples, one representative section was used for CODEX stainings in the case of primary tissue and PDX samples.

2.5 Immunofluorescence microscopy

Immunofluorescence (IF) staining evaluation was used to analyze drug-specific effects on tumor cells in DBOs. The detailed procedures of staining, imaging and analysis are described below.

2.5.1 DBO antibody staining and image acquisition

Slides with DBO treatments were incubated on a heating plate for 20-25 min and then left at room temperature to cool down. For deparaffinization, slides were placed in a rack of a manual staining station and incubated twice for 5 min in Histoclear. This was followed by a stepwise rehydration in a descending ethanol series of 100 % (twice), 90 %, 70 %, 50 % and 30 %. Slides were left in each ethanol dilution for 5 min. After washing slides two times in ddH_2O, antigen retrieval was performed using a pressure cooker. For this purpose, the slides were placed in a beaker containing 1x citrate buffer solution (pH 6) and the pressure cooker was filled with approximately 1,2 l of water. The beaker was sealed with aluminum foil and placed in the pressure cooker. A 20 min incubation was performed using the "high pressure" protocol of the cooker. Pressure was then slowly released to avoid bubble formation and slides were removed from the cooker to cool them down to room temperature. After two washing steps in ddH2O of 10 min each, autofluorescence was quenched. Therefore, autofluorescence quenching solution was prepared by combining 1x phosphate buffered saline (PBS) with 30 % H_2O_2 (final concentration 4,5 % w/v) and 1M NaOH solution (final concentration of 20 mM). 30 ml of quenching solution was poured in per lid of a 6-well plate and slides were fully submerged in the solution. Lids were covered with a second 6-well plate lid and sandwiched between two broad spectrum LED lamps. Bleaching was performed for 45 min with 20.000-25.000 LUX. After the first incubation, the quenching solution was replaced by a fresh one and another bleaching step of 45 min followed. To remove the quenching solution, slides were washed once in 1x PBS for 3-5 min. Blocking of the samples was performed in a humidity chamber with 5 % goat serum and 0,3 % Triton X-100 in 1x PBS. After adding 200 µl blocking solution, slides were covered with parafilm to prevent samples from drying out. The blocking took 60 min at room temperature. Blocking solution was removed by gently decanting slides onto a paper towel and 200 µl primary antibody solution was added per slide. Antibodies were diluted in blocking solution and incubation was performed overnight at 4°C. Slides were therefore again covered with parafilm and placed in the humidity chamber. On the next day, antibody solution was washed away twice for 2 min with 1x PBS. 200 µl of blocking solution with secondary antibodies was added per sample. Covered with parafilm, slides were incubated for 60 min at room temperature in the dark. Two washing steps of 5 min with 1x PBS and DAPI staining followed. DAPI stock solution (1mg/ml) was diluted 1:1000 in 1x PBS and pipetted onto the sections. After incubation for 30 min at room temperature in the dark, the slides were washed again twice for 5 min with 1x PBS. Mounting medium was applied and cover slips were placed on the samples. After the medium had dried for 30 min at room temperature in the dark, slides were sealed with transparent nail polish. Once the nail polish was dry, the samples were ready for microscopy. For later imaging, stained slides were stored at 4°C in the dark. Using a Keyence microscope, DBO sections were imaged in all stained channels with a 10x magnification. Single images with different channels were stitched with the BZ-X800 Viewer software to get one complete picture of each organoid section.

2.5.2 DBO image evaluation and statistics

The BZ-X800 Analyzer software with the included hybrid cell count module (area extraction function) was used for DBO treatment evaluation. The total areas of nuclei with H3K27M-signal in organoid sections were measured, together with the respective proportions of KI67-positive regions within H3K27M areas. Since the H3K27M-signal is tumor cell specific, only the BT869 cells within the DBOs were analyzed. Measurements were exported to excel and normalized to the controls. Changes in H3K27M-areas served as a measurement for tumor burden reduction after treatments. In addition, changes in tumor cell proliferation rates within the malignant cells were measured by KI67-positive H3K27M areas. Six DBOs (one section per DBO from thickest/middle part) were analyzed per drug concentration from two independent differentiation/treatment rounds of three organoids each. For statistical analysis unpaired two-sided t-tests were performed using excel.

2.6 CODEX: Multiplexed immunofluorescence imaging

2.6.1 Antibody selection for CODEX conjugation

Since the CODEX system detects proteins in an antibody-based manner, suitable antibodies were first selected. For this purpose, the RNAseq data from Filbin et al., 2018 were used to choose subpopulation-specific markers with sufficiently high expression levels. Appropriate monoclonal antibodies were then selected and validated using regular FFPE IF-staining. Ordered antibody solutions had to be free of bovine serum albumin (BSA) and sodium azide, otherwise these components would interfere with the subsequent conjugation of antibody and barcode. During validation, also the optimum dilution and exposure times of individual antibodies were determined.

2.6.2 CODEX antibody conjugation

Only a few useful barcode-conjugated antibodies were available from Akoya (anti-KI67, -CD31, -PCNA and -CD44 antibody) and therefore the remaining once had to be manually conjugated. For this purpose, the Akoya Biosciences conjugation reagent kit was used (all antibody barcode combinations are listed in Table 2). Antibodies were first purified using a 50 kDa MWCO filter. Filters were placed in collection tubes and blocked with 500 µl of filter blocking solution. After a centrifugation step of 12.000x g for 2 min, the flow-through was discarded. 50 µg of each antibody was pipetted onto a filter in a total volume of 100 µl. If the corresponding volume of the antibody stock solution was less than 100 µl, the volume was adjusted to 100 µl with 1x PBS. The filters were centrifuged at 12,000x g for 2 min and the flow-through was discarded. Disulfide bridges between heavy antibody chains were reduced using an antibody reduction master mix. The master mix consisted of 6,6 µl reduction solution 1 and 275 µl reduction solution 2 for each reduction reaction. After addition of 260 µl master mix, each filter was vortexed for 3 sec and incubated at room temperature for 30 min. Filters were then centrifuged at 12,000x g for 8 min and the flow-through was discarded. 450 µl of conjugation solution was pipetted onto filters and another centrifugation step of 12,000xg for 8 min followed. In the meantime, barcodes from Akoya were resuspended in 10 µl of nuclease-free water. To each resuspended barcode, 210 µl of conjugation solution was added and the resulting solution was mixed by careful pipetting up and down. The flow-through in the collection tubes was discarded and the complete barcode solution was pipetted onto the appropriate filter. After vortexing the filters for 3 sec, the actual conjugation reaction took place at room temperature for 2 h. Afterwards, the conjugated antibodies were purified. For this purpose, the filters were centrifuged at 12,000x g for 8 min. After discarding the flow-through, 450 µl of the purification solution was added to the top of each filter. Again, filters were centrifuged at 12,000x g for 8 min and the flow-through discarded. Purification solution was added to filters two more times with subsequent centrifugation. After discarding the last flow-through of purification solution, 100 µl of the antibody storage solution was added to each filter. To collect the conjugated antibodies, each filter was placed upside down in a 50 ml conical tube and centrifuged at 3,000xg for 2 min. Antibody solutions were then transferred to sterile 1,5 ml tubes and stored at 4°C for further use.

Table 2: Antibody barcode combinations for CODEX detection of different marker proteins and used antibody dilutions.

Antibody against:	**Marker for:**	**Conjugated barcode:**	**Dilution:**
H3K27M	Tumor cells	BX004	1:50
KI67	Cycling cells	BX047	1:200
CD31	Vasculature	BX001	1:100
GFAP	AC-like	BX030	1:50
CD44	AC-like	BX005	1:50
APOE	AC-like	BX010	1:50
SIRT2	OC-like	BX019	1:50
BCAS1	OC-like	BX027	1:50
BIN1	OC-like	BX014	1:100
SOX10	OPC-like	BX026	1:50
PDGFRα	OPC-like	BX054	1:25
PCNA	OPC-like	BX036	1:50

2.6.3 Sample preparation for CODEX staining

Paraffin embedded samples were sectioned and mounted on slides as described under 2.4. Since the CODEX system requires a special sample slide format, 22 x 22 mm coverslips were coated with poly-L-lysine for proper section attachment. For this purpose, 100 mm dishes were filled with 0,1 % poly-L-lysine solution and coverslips were completely submerged in the liquid. Care was taken to prevent bubble formation and to avoid overlapping of the coverslips to ensure a homogeneous coating. Dishes were sealed with parafilm and incubated over night at room temperature. On the next day, the poly-L-lysine solution was poured slowly out of the dishes and MilliQ water was added to the coverslips. After swirling, coverslips were left in the water for a maximum of 30 sec and water was carefully decanted afterwards. This washing step was repeated 4-6 times. Coverslips were leaned against the wall of the cell culture dish lids and dried overnight. Next, the coated coverslips were stored in covered petri dishes at room temperature for no longer than 2 months.

2.6.4 CODEX antibody staining and detection

Procedures of deparaffinization, hydration, antigen retrieval and autofluorescence quenching were performed as described under 2.5.1. Since coverslips with samples for CODEX staining were significantly smaller than normal slides, the autofluorescence quenching was performed in wells of a 6-well plate. The CODEX staining kit was used for the following protocol steps.

After autofluorescence quenching, coverslips were washed twice with ddH_2O. For each sample, two wells of a 6-well plate were prepared with 5 ml of hydration buffer and one well with 5 ml of staining buffer. The coverslips were immersed with tweezer in wells containing hydration buffer for 2 min each, followed by a 30 min equilibration step in the staining buffer. Meanwhile, a CODEX blocking buffer was prepared. 181 µl of staining buffer were combined with 4,75 µl of blocker solutions N, G, J, and S for each coverslip. To create the final antibody cocktail, all antibodies were diluted in blocking buffer (dilution factors are listed in Table 2). At least 60 % of the cocktail had to consist of blocking buffer to ensure sufficient masking of non-specific binding sites. Coverslips were removed from staining buffer and transferred into a humidity chamber. 190 µl of antibody cocktail was dispensed on each sample and primary antibody incubation was performed overnight at 4°C. The next day, 6-well plates for the post-staining steps were prepared. For each sample, two wells with staining buffer, one well with post-staining fixing solution and three wells with 1x PBS were filled with an individual volume of 5 ml. The post-staining fixing solution was prepared by combining 0,5 ml of 16 % paraformaldehyde (PFA) with 4,5 ml storage buffer per sample. Furthermore, 5 ml ice-cold methanol was added to one well. Samples were washed in the prepared staining buffer wells for two min each and fixed for 10 min in post-staining fixing solution at room temperature. Afterwards, coverslips were immersed sequentially in the three 1x PBS wells for a few seconds and then incubated in ice-cold methanol for 5 min. To completely remove the methanol, samples were again washed three times in 1x PBS and placed in a humidity chamber.

For the final fixation, 200 µl of fixation solution (1 ml PBS with 20 µl fixative reagent) was dispensed on each coverslip and incubated for 20 min. Three more washing steps in 1x PBS followed and finally the samples were stored in storage buffer at 4°C. CODEX detection was either started directly or the slides were stored for a maximum of 5 days.

For CODEX detection, reporter mixtures had to be prepared in a 96-well format. First, a reporter stock solution was created in an aluminum-wrapped 15 ml conical tube. For 10 cycles, 2,44 ml of nuclease-free water was added with 300 µl 10x CODEX buffer, 250 µl assay reagent and 10 µl nuclear stain. The tube was gently inverted a few times. For each cycle, a reporter master mix was pipetted into a black 1,5 amber tube. In addition, two tubes containing blank cycles were prepared. While only 250 µl of reporter stock solution was needed for each blank cycle tube, the same volume of individual reporter master mix solutions was prepared for marker detection cycles. For this purpose, the reporters were diluted 1:50 in reporter stock solution. A maximum of three reporters with different wavelengths (AF488, ATTO550 or CY5) were combined per cycle and tube. Since each well of the 96-well plate corresponded to one cycle of the experiment, 245 µl were pipetted from one tube into one well. The first and the last well/cycle were thereby assigned to the blank cycles. After the solutions from all tubes were pipetted into the corresponding wells, the 96-well plate was carefully sealed with a light-proof plate foil and placed in the CODEX instrument. After priming the instrument, the coverslip was sandwiched between the CODEX stage and a premoistened sealing gasket. CODEX buffer containing 1:1500 diluted nuclear stain was pipetted onto the sample and incubated for a few min. After setting the microscope parameters (CODEX Instrument Manager and the Keyance BZ-X800 software), CODEX image acquisition was started. The resulting image data were exported with the instrument manager and processed using the CODEX Processor software. In this step, the images were stitched, and cell segmentation based on nuclear signals was performed, providing one large image with all markers ready for analysis.

2.6.5 CODEX quantification and statistics

The CODEX images of all experiments were analyzed using the ImageJ plugin CODEX Multiplex Analysis Viewer (MAV). Once the nucleus-based segmentation was verified, marker-positive cell populations could be identified. Markers were sequentially gated and signal intensity values were defined that corresponded only to the marker-positive cell segments. A table containing each cell segment with the corresponding intensities of all markers was exported to excel. In case of the primary tissues, CD31-positive cell segments (areas of blood vessels) were initially excluded, as they exhibited strong autofluorescence that would bias the results. Within the tumor cell segments (H3K27M-positive), the respective marker-positive cell numbers were quantified using the defined intensity gates and consequently subpopulation composition was determined. Cell numbers of three markers were pooled per subpopulation. While GFAP, CD44, and APOE were used for the AC-like subpopulation, the OPC-like subpopulation was formed by SOX10-, PCNA-, and PDGFRα-positive cells. For the OC-like population, SIRT2-, BCAS1-, and BIN1-positive cells were combined.

For primary tissue samples, sections (one per tumor) from seven different H3K27M DMGs were analyzed with a total of 1.26 million tumor cells (number of analyzed tumor cells per section varied between 31.000 and 518.000 cells). 230.000 and 50.000 BT869 tumor cells were analyzed from sphere culture and the PDX (one section per sample), respectively. In case of DBO co-culture analysis, between 4.000 to 30.000 tumor cells were analyzed per time point (one section of one DBO per time point). For DBO treatment analysis, four DBOs (one section each) were analyzed per drug concentration from two independent differentiation/treatment rounds (between 32.000 and 120.000 analyzed tumor cells per DBO).

2.7 Material

The following tables provide lists of all materials, equipment, chemicals, drugs, and software used.

2.7.1 Plastic consumables

Product	Company	Catalog number
T25 cell culture flask	Sarstedt	833.910.002
T75 cell culture flask	Sarstedt	833.911.002
Nunc™ 6-well plate	ThermoFisher Scientific	140675

Product	**Company**	**Catalog number**
Ultra Low Cluster, 96 Well, With Lid round Bottom, Ultra Low Attachment Polysterene plate	Corning	7007
TC Dish 100, Cells+ (10 cm dish)	Sarstedt	833.902.300
96-Well Plates reporter black	Akoya	232527
Vacuum filtration unit Filtropur V100, 1000 ml, PES membrane, 0.22 µm pore size	Sarstedt	833.942.001
Vacuum filtration unit Filtropur V50, 500 ml, PES membrane, 0.22 µm pore size	Sarstedt	833.941.001
70 µm Nylon Cell Strainer	VWR	732-2758
Collection Vessel 1000 ml	Sarstedt	833.942.005
Collection Vessel 500 ml	Sarstedt	833.941.005
Tube 15 ml	Sarstedt	62.554.502
Tube 50 ml	Sarstedt	62.547.254
Tube 0,5 ml	Sarstedt	72,704
Tube 1,5 ml	Sarstedt	72,706
Tube 2 ml	Sarstedt	72.695.500
LiteSafe Black Microtubes 1,5 ml	Argos Technologies	T7100BK
CryoTube Vials	ThermoFisher Scientific	368632
Cool Cell® LX Freezing Container	Corning	432001
Serological Pipette 50 ml	Sarstedt	861.256.001
Serological Pipette 25 ml	Sarstedt	861.685.001
Serological Pipette 10 ml	Sarstedt	861.254.001
Serological Pipette 5 ml	Sarstedt	861.253.001
Aspiration Pipette 2 ml	Sarstedt	861.252.011
Pipette Tips 1250 µl	Integra	3444
Pipette Tips 300 µl	Integra	3434
Pipette Tips 300 µl, wide bore	Integra	6635
Pipette Tips 125 µl	Integra	3427
Pipette Tips 12,5 µl LONG	Integra	3404

Product	Company	Catalog number
Pipette Tips 1250 µl, robot	Integra	6444
Pipette Tips 300 µl, robot	Integra	6434
Pipette Tips 125 µl, robot	Integra	6464
Pipette Tips 12,5 µl LONG, robot	Integra	6406
Pierce Protein Concentrators PES, 50k MWCO, 0,5 ml	ThermoFisher scientific	88504
Gaskets	Akoya	7000010
Plate Seals	Akoya	232528
Parafilm	Bemis Curwod	PM-996
Biopsie-/Einbettkassetten Microsette™ M503	VWR	720-0961
Small biopsy processing/embedding cassettes, Microscreen™	VWR	SIMPM520-2
Countess™ cell counting chamber	ThermoFisher scientific	C10228
Organoid Embedding Sheet	STEMCELL Technologies	08579
Clear Advantage Reagent Reservoirs	INTEGRA	4332

2.7.2 Glass consumables

Product	Company	Catalog number
SuperFrost Plus slides (Mengel Gläser) 24x75x1,0 mm	ThermoScientific	J1800MNZ
Cover slip 25x75x1,0 mm	R. Langenbrinck	01-2460/M
Glass Cover Slips 22 x 22mm	Electron Microscopy Sciences	72204-01

2.7.3 Chemicals, solutions, and media components

Product	Company	Catalog number
Neurobasal-A medium	ThermoFisher Scientific	10888-022
DMEM/F-12 (1:1) (1X)	ThermoFisher Scientific	11330-032
HEPES Buffer Solution (1M)	ThermoFisher Scientific	15630-080

Product	**Company**	**Catalog number**
Sodium Pyruvate (100 mM) (100X)	ThermoFisher Scientific	11360-070
MEM Non-Essential Amino Acids Solution (MEM NEAA) (100X)	ThermoFisher Scientific	11140-035
GlutaMAX-I Supplement (100x)	ThermoFisher Scientific	35050-061
Antibiotic-Antimycotic (100X)	ThermoFisher Scientific	15240-062
B-27 Supplement without Vitamin A (50x)	ThermoFisher Scientific	12587001
hEGF	BIOZOL	SHD-100-26
hFGF-basic-154	PeproTech	100-18B
hPDGF-AA	PeproTech	100-13A
HPDGF-BB	PeproTech	100-14B
Heparin Solution (0,2 %)	STEMCELL Technologies	7980
mTeSR Plus Basal Medium	STEMCELL Technologies	100-0274
mTeSR Plus 5x Supplement	STEMCELL Technologies	100-0275
GlutaMAX supplement (100×)	ThermoFisher Scientific	15070-063
Penicillin-streptomycin (100×)	ThermoFisher Scientific	15240062
B27 supplement (50x)	ThermoFisher Scientific	17504-001
MEM NEAA (100x)	ThermoFisher Scientific	11140-050
N2 supplement (100x)	ThermoFisher Scientific	17502001
Human insulin solution	Sigma	I9278
2-Mercaptoethanol (1000x)	ThermoFisher Scientific	21985-023
ReLeSR	StemCell	5872
Gentle Cell Dissociation reagent	StemCell	07174
TrypLE	Gibco	12604013
Basal Medium I	STEMCELL Technologies	8572
Basal Medium II	STEMCELL Technologies	8573
Supplement A	STEMCELL Technologies	8574
Supplement B	STEMCELL Technologies	8575
Supplement C	STEMCELL Technologies	8576
Supplement D	STEMCELL Technologies	8577

Product	**Company**	**Catalog number**
Matrigel Matrix hESC qualified	Corning	354277
Bambanker Serum-Free Cell Freezing Media	Nippon Genetics Europe	BB01
Rock inhibitor solution (Y-27632)	Selleckchem	S1049
Dimethyl sulfoxide (DMSO)	Sigma-Aldrich	D2650
Formaldehyde solution 4 %	Microcos gmbH	50-00-0
Histoclear (HistChoice Clearing Agent)	VWR Life Science	H103-4L
Ethanol	Carl Roth	K928.4
10x sodium citrate buffer	Sigma	C9999-1000ml
10x PBS	Gibco	70013016
Sodium hydroxide (NaOH)	SIGMA-ALDRICH	S8045
Hydrogen peroxide solution 30 %	SIGMA-ALDRICH	216763
Goat serum	Sigma	G9023-5ml
Triton X-100	Carl Roth	3051.4
DAPI	ThermoFisher Scientific	62248
Fluoroshield mounting medium	Sigma	F6182-20ml
Nail polish (clear)	Manhatten	010 clear
Filter blocking solution	Akoya	232113
Reductionnsolution 1	Akoya	232194
Reductionnsolution 2	Akoya	232115
Antibody storage	Akoya	232118
Conjugation solution	Akoya	232116
Ambion Nuclease-Free Water	Invitrogen	AM9930
Poly-L-lysine solution	SIGMA-ALDRICH	P8920-100ML
Hydration buffer	Akoya	232105
Staining Buffer	Akoya	232106
Storage Buffer	Akoya	232107
Fixative reagent	Akoya	232112
N Blocker	Akoya	232108

Product	Company	Catalog number
J Blocker	Akoya	232110
S Blocker	Akoya	232111
G Blocker	Akoya	240199
Paraformaldehyde 16 %	Electron Microscopy Sciences	15710-250
Methanol	Sigma-Aldrich	322415
10x CODEX buffer	Akoya	232119
Assay reagent	Akoya	232120
Nuclear stain	Akoya	232121

2.7.4 Antibodies, CODEX barcodes, and reporters

Product	Company	Catalog number	Dilution
Recombinant Anti-Histone H3 (mutated K27M) antibody [EPR18340]	abcam	ab190631	1:500
Purified Mouse Anti-Ki-67 antibody [B56]	BD Biosciences	550609	1:200
Goat anti-Mouse IgG (H+L) Cross-Adsorbed Secondary Antibody, Alexa Fluor™ 555	Invitrogen	A21422	1:200
Goat anti-Rabbit IgG (H+L) Cross-Adsorbed Secondary Antibody, Cyanine5	Invitrogen	A10523	1:500
Recombinant Anti-Histone H3 (mutated K27M) antibody [EPR18340]-ChIP Grade-BSA and Azide free	Abcam	ab240310	1:50
Purified anti-SOX10 antibody [BSB-62]	Biolegend	847202	1:50
Recombinant Anti-PDGFR alpha antibody [EPR22059-270] - BSA and Azide free	Abcam	ab234965	1:50
Purified anti-SIRT2 antibody [W16205A]	Biolegend	650202	1:50
BCAS1 antibody	Santa Cruz	sc-136342	1:50
Purified anti-Bin1 antibody [99D]	Biolegend	655602	1:100
Recombinant Anti-Apolipoprotein E antibody [EP1373Y] - BSA and Azide free	Abcam	ab171357	1:50

Product	**Company**	**Catalog number**	**Dilu-tion**
GFAP Monoclonal Antibody [2.2B10]	ThermoFisher Scientific	13-0300	1:50
KI67-BX047 (B56)—Atto 550-RX047	Akoya	4250019	1:200
CD31-BX001 (EP3095)—Alexa Fluor 488-RX001	Akoya	4150017	1:100
Anti-Hu CD44(AKYP0073)-BX005—Atto 550	Akoya	4450041	1:50
Anti-Hu PCNA(AKYP0085)-BX036—Cy5	Akoya	4450054	1:25
BX004—Alexa Fluor 488-RX004	Akoya	5450014	/
BX030—Cy5-RX030	Akoya	5550012	/
BX019—Alexa Fluor 488-RX019	Akoya	5150002	/
BX027—Cy5-RX027	Akoya	5550011	/
BX010—Alexa Fluor 488-RX010	Akoya	5450016	/
BX026—Atto 550-RX026	Akoya	5250004	/
BX054—Atto 550-RX054	Akoya	5250010	/
BX014—Atto 550-RX014	Akoya	5450025	/

2.7.5 Drugs

Name	**Company**	**Catalog number**
5-Azacytidine	MedChemExpress	HY-10586
Adavosertib	MedChemExpress	HY-10993
Alvespimycin	MedChemExpress	HY-12024
AUY922	Adooq Biosciences	A10659
Belinostat	MedChemExpress	HY-10225
Carfilzomib	MedChemExpress	HY-10455
Cevipabulin	MedChemExpress	HY-14949
Daporinad	MedChemExpress	HY-50876
Delanzomib	TargetMol	T6027/847499-27-8
Dinaciclib	Adooq Biosciences	A11129-5
Filanesib	MedChemExpress	HY-15187

Name	Company	Catalog number
Fimepinostat	Selleckchem	S2759
Ganetispib	MedChemExpress	HY15205
Gedatolisib	TargetMol	T1970/1197160-78-3
Geldanamycin	TargetMol	T6342/30562-34-6
Gemcitabine	MedChemExpress	HY-17026
GMX-1778	TargetMol	T1998/200484-11-3
HSP-990	Adooq Biosciences	A12850
Marizomib	Sigma-Aldrich	SML1916
ONC201	AbMole BioScience	M3068
ONC206	MedChemExpress	HY135147
Panobinostat	MedChemExpress	404950-80-7
Paxalisib	Selleckchem	S8163
PF-03814735	MedChemExpress	HY-14574
Quisinostat	MedChemExpress	HY-15433
Rigosertib	MedChemExpress	HY-12037A
Romidepsin	MedChemExpress	HY-15149
Sapanisertib	Selleckchem	S2811
Vistusertib	MedChemExpress	HY-15247
Zotiraciclib	Adooq Biosciences	A11962

2.7.6 Equipment and pipettes

Product	Company	Catalog number
Microtome	Leica	SM2010R
IHC manual staining station	IHC world	IW-2510
Insert for dyeing basins, glass + hanger	BRAND	472000 and 473100
Dyeing basin with lid, glass	BRAND	472200
Dyeing basin with lid, PMP	Roth	2292.2
EVOLVE Pipette 1-Ch, 0,2-2 µl	INTEGRA	3011
EVOLVE Pipette 1-Ch, 1-10 µl	INTEGRA	3012

Product	Company	Catalog number
EVOLVE Pipette 1-Ch, 2-20 µl	INTEGRA	3013
EVOLVE Pipette 1-Ch, 10-100 µl	INTEGRA	3015
EVOLVE Pipette 1-Ch, 20-200 µl	INTEGRA	3016
EVOLVE Pipette 1-Ch, 100-1000 µl	INTEGRA	3018
6 Channel VOYAGER pipette 10-300 µl	Integra	4763
6 Channel VOYAGER pipette 50-1250 µl	Integra	4764
8 Channel VOYAGER pipette 0,5-12,5 µl	Integra	4721
8 Channel VOYAGER pipette 10-300 µl	Integra	4723
8 Channel VOYAGER pipette 50-1250 µl	Integra	4724
S1 Pipet filler	Thermo Scientific	245138

2.7.7 Technical devices

Product	Company	Catalog number
MAXISAFE 2030i laminar flow hood	Thermo Scientific	51033115
Precision GP 10 water bath	Thermo Scientific	TSGP10
Vacusafe cell culture pump	INTEGRA	158320
UNIMAX 1010 shaker	Heidolph Instruments	543-12310-00
Centrifuge 5804 R	Eppendorf	580510137
MC6 Minicentrifuge	Sarstedt	90.186.100
HERACELL VIOS 250i incubator	ThermoFisher Scientific	51030965
Countess 3 cell counter	ThermoFisher Scientific	/
Assist Plus Pipetting Robot	Integra	4505
Communication Module for Integra electronic pipettes	Integra	4221
EVOS XL Core microscope	Invitrogen	AMEX1000
IncuCyte S3	Sartorius	4763
Keynece BZ-X810E microscope	Keyence	BZ-X810E
Histological water bath	Leica	HI1210
Heating plate	Medax Nagel Gmbh	/

Product	**Company**	**Catalog number**
Drying oven	WTB BInder	FD 720
LED lamp	Thsinde	/
InstantPot duo	InstantPot	Duo 06
Fatty tissue processor	Sakura	Tissue-Tek VIP
Paraffin embedding station	Thermo Scientific	EC350

2.7.8 Software

Name	**Company**	**Version**
ImageJ Fiji	imageJ	ImageJ-win64
CODEX Multiplex Analysis Viewer	ImageJ/Akoya	1.4.0.3
CODEX Processor	Akoya	/
CODEX Instrument Manager	Akoya	1.30.0.12
BZ-X800 Viewer	Keyence	/
BZ-X800 Analyzer with Hybrid cell count	Keyence	/
GraphPad Prism 9	GraphPad	9.5.1

3. Results

In this work, the DBO culture was developed in order to create a new H3K27-altered DMG model for preclinical drug testing. Using the new CODEX system, tumor cell composition of DBOs was compared with that of primary tumor samples and other DMG models for validation. In addition, DBOs were used to characterize the treatment effects of promising drug candidates. All results are presented in the following sections.

3.1 Tumor cell composition of H3K27-altered diffuse midline gliomas

To assess the tumor biology of H3K27M-altered DMGs, seven primary tumors were analyzed using the CODEX multiplexed fluorescence imaging system. AC-, OC- and OPC-like tumor cells were present in all DMG samples with varying percentages (Figure 4). Four of seven tumors (DMG1, DMG2, DMG3 and DMG4) were composed mostly of AC-like cells with 85 % to 42 %. In samples DMG2 and DMG3, OPC-like cells formed the second largest subpopulation with 30 % and 35 %, while OC-like cells were the least represented subpopulation (5 % and 12 %). DMG4 showed a higher OC-like proportion with 37 % and OPC-like cells accounted for the smallest subpopulation here with 21 %. In DMG1, which showed the highest AC-like proportion over all (85%), OPC-like and OC-like cells were represented relatively equally with percentages around 8 %. In contrast, DMG5 and DMG7 showed OPC-like cells as largest tumor fraction with 41 % and 46 %, followed by AC-like (31 % to 41 %) and OC-like cells (18 % to 23 %). Only in DMG6, OC-like cells were the most represented cell type with 39 %, while the AC-like tumor fraction accounted for 32 % and OPC-like cells for 29 %.

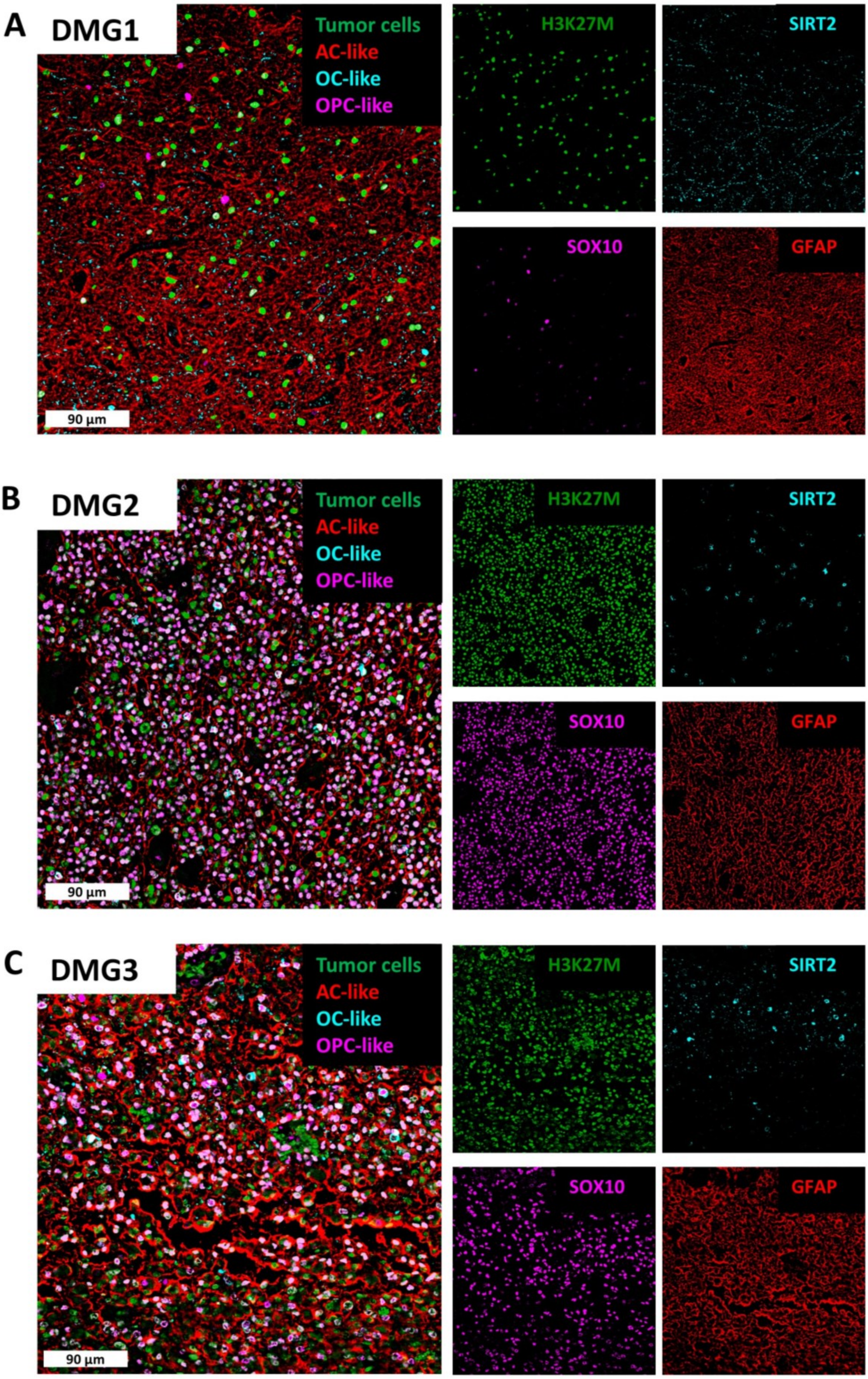

Figure 4, part 1: Tumor cell composition of H3K27M-altered DMGs. For description see page 55.

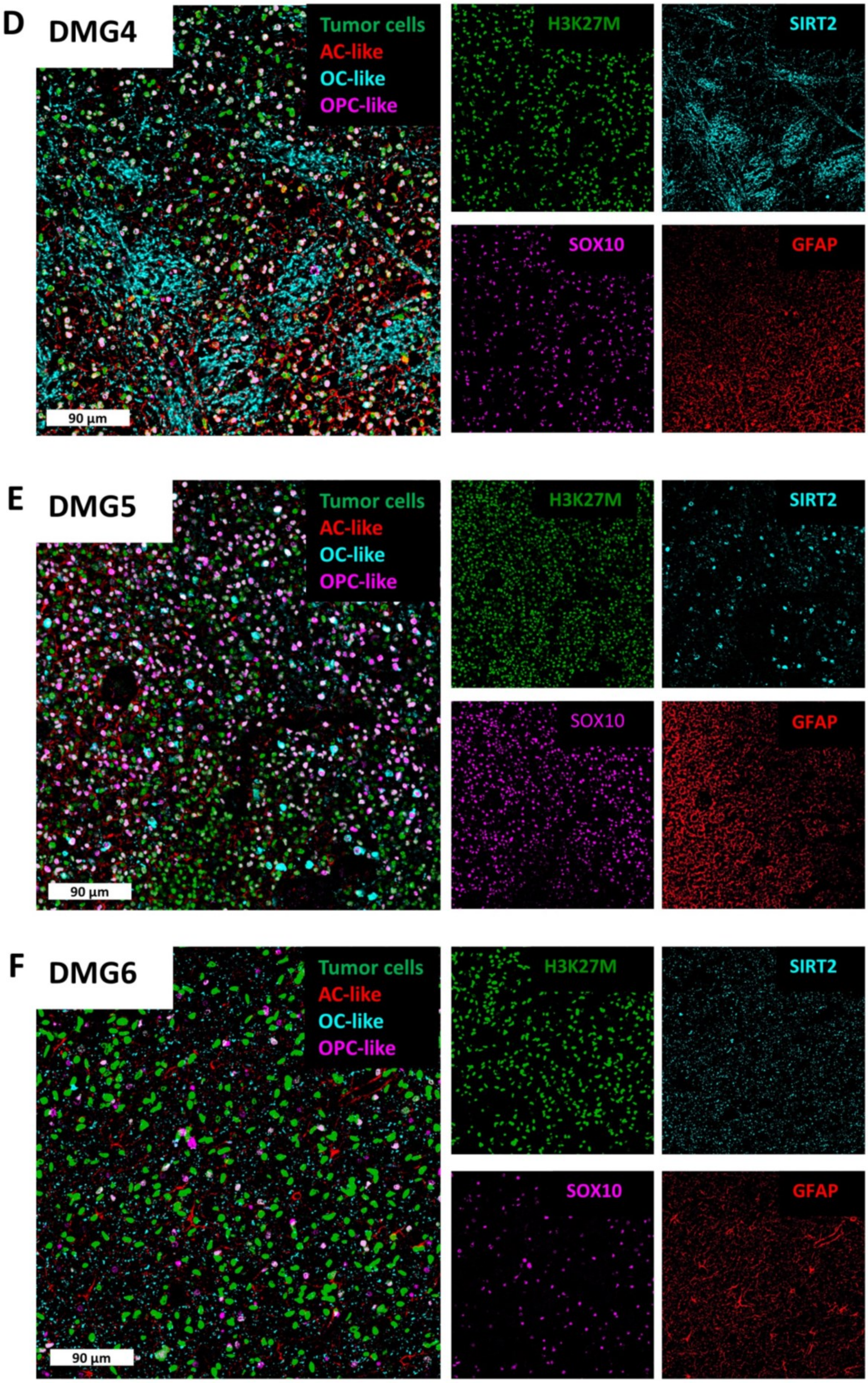

Figure 4, part 2: Tumor cell composition of H3K27M-altered DMGs. For description see page 55.

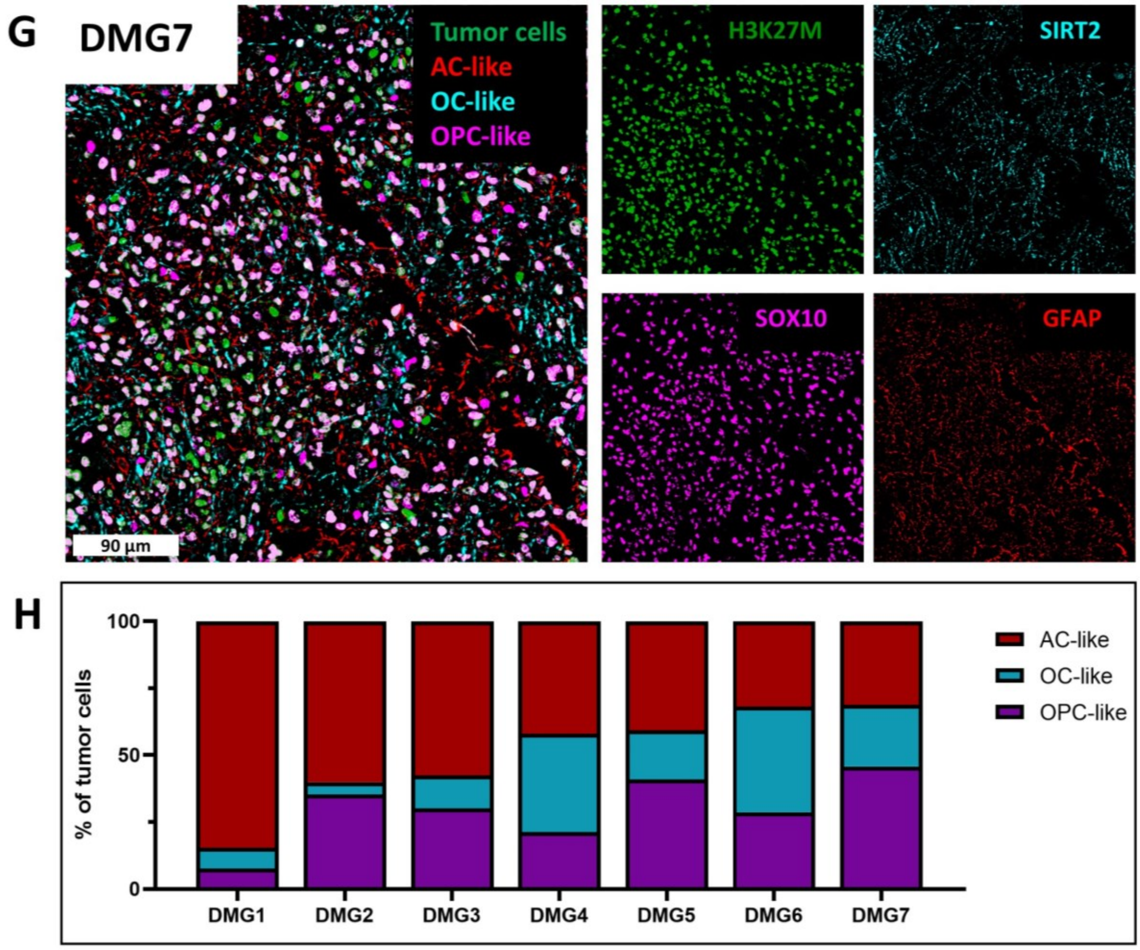

Figure 4, part 3: Tumor cell composition of H3K27M-altered DMGs. ***A*-*G*:** Representative multiplexed CODEX images of subpopulation composition in sections of seven primary human DMGs. H3K27M tumor cells are displayed in green. Representative for OPC-like cells, SOX10 is shown in magenta, while for OC-like cells SIRT2 is shown in cyan. GFAP in red indicates AC-like cells. ***H*:** Tumor composition of whole primary human DMG sections detected with the CODEX system. For each subpopulation cell counts from three individual markers where combined. Number of analyzed tumor cells per section varied between 31.000 and 518.000 cells.

Numbers of actively cycling cells were also analyzed. Proportions of proliferating tumor cells marked by KI67 expression were highest in DMG3 with 16 % and lowest in DMG4 and DMG1 with 5 % to 7 % (Figure 5). The remaining tumor sections showed tumor cell proliferation rates around 11 %.

Altogether, across all tumor samples, the AC-like and OPC-like populations were found to be the most prevalent subpopulations, followed by OC-like with the lowest proportions. On average, about 10 % of the tumor cells were proliferating.

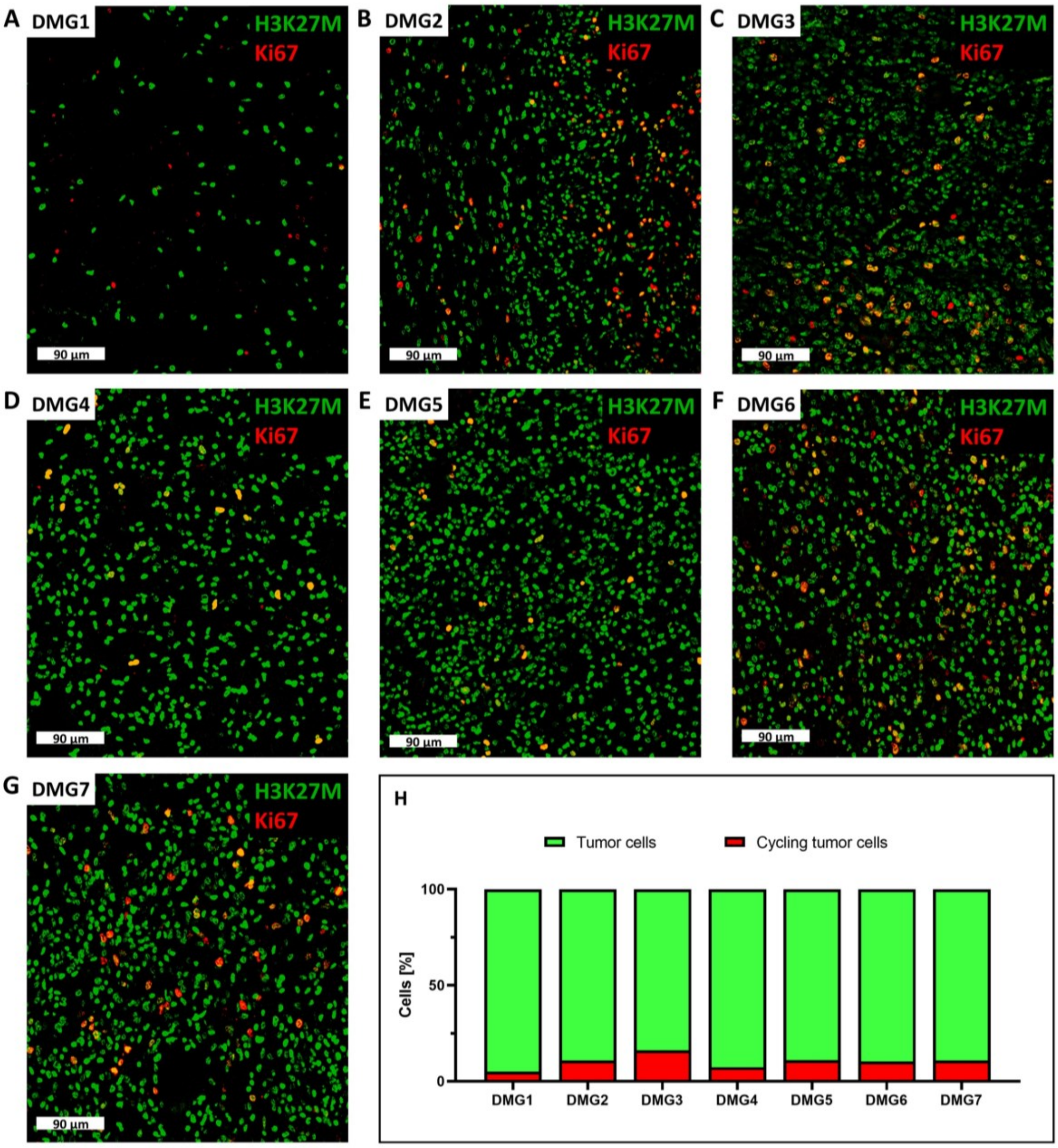

Figure 5: Cycling tumor cells in H3K27M-altered DMGs. A-G: Representative CODEX images of cycling tumor cells in seven primary human DMG sections. Tumor cells are shown in green and marked by the H3K27 mutation. Proliferating cells are labelled in red by KI67. H: Total percentages of cycling tumor cells across whole tumor sections. Number of analyzed tumor cells per section varied between 31.000 and 518.000 cells.

3.2 Tumor cell composition of current DMG models

To evaluate the cellular heterogeneity of current preclinical DMG models, the composition of H3K27-mutated cells (BT869) was examined in sphere culture as well as in the mouse model (PDX) using the CODEX system.

BT869 cell composition in sphere culture consisted mostly of OPC-like cells (80 %). Only 19 % of OC-like tumor cells where present and AC-like cells were barely detectable with a percentage of 1 % (Figure 6A-B). With 97 %, almost all cells in the sphere culture were in active cell division (Figure 6C-D).

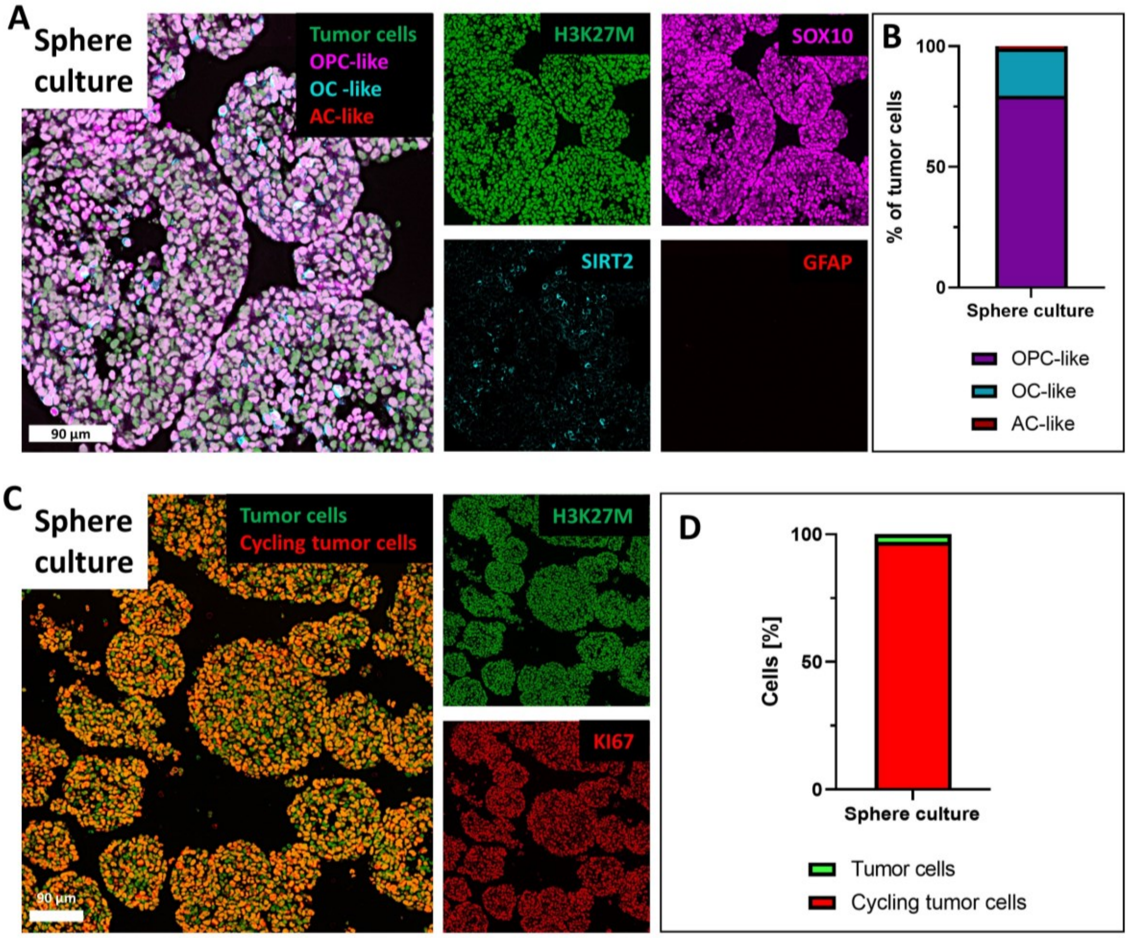

Figure 6: Tumor cell composition and proportion of cycling cells in the H3K27M BT869 sphere culture. **A** shows representative multiplexed CODEX images from BT869 spheres. All tumor cells are labelled in green by the H3K27M signal. SOX10 is shown in magenta as a representative for the OPC-like fraction, while SIRT2 in cyan represents OC-like cells. GFAP in red indicates AC-like cells. The cellular composition is presented in **B**. Each population contains cell numbers from three independent markers. **C** shows representative images of actively cycling cells. Tumor cells are again shown in green (H3K27M), while the proliferation marker KI67 is shown in red. The corresponding overall analysis of proliferation rate is given in **D**. A total of 230.000 tumor cells were analyzed for the calculation of subpopulations and proliferation rates.

When analyzing the same cell line stereotactically injected into the pons of the mouse brain (PDX), the major proportion of BT869 cells exhibited OC-like characteristics with a proportion of 48 %. OPC-like cells were the second largest population at nearly 30 %, closely followed by the AC-like cells at 22 % (Figure 7A-B). Only 34 % of the tumor cells were actively cycling in the PDX model system (Figure 7C-D).

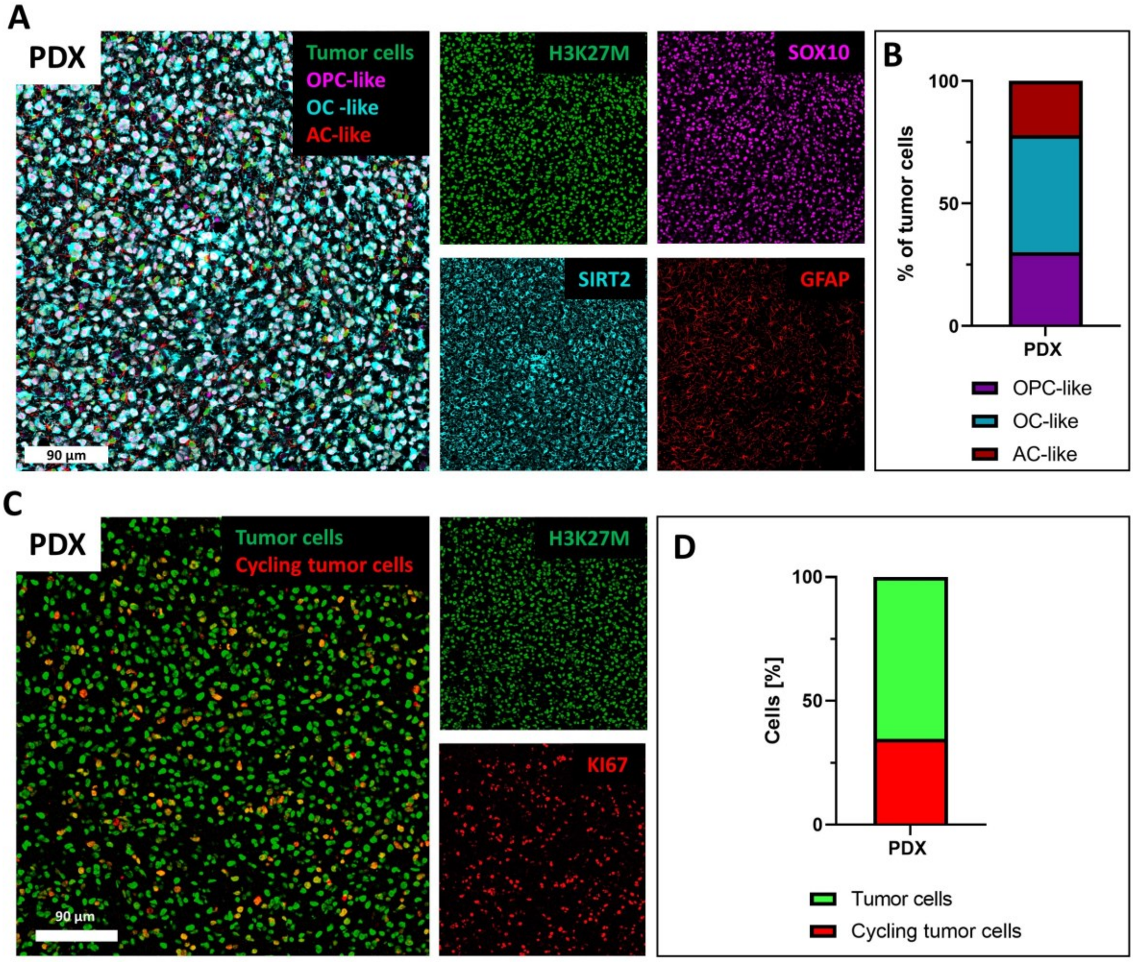

Figure 7: Tumor cell subpopulations and proliferation rates in BT869 derived PDX. **A** shows representative multiplexed CODEX images of an orthotopic PDX mouse model. BT869 tumor cells are colored in green by the H3K27M signal. Representative for OPC-like tumor cells, SOX10 is shown in magenta. SIRT2 in cyan represents OC-like cells, while AC-like cells are indicated by GFAP in red. Results of the cellular composition analysis are presented in **B**, with each population containing cell counts from three marker proteins. Representative images of proliferating BT869 cells are shown in **C**. Human tumor cells are highlighted in green by H3K27M and the proliferation marker KI67 is shown in red. The associated CODEX analysis of proliferation rate is shown in **D**. 50.000 BT869 tumor cells were analyzed from one PDX sample.

3.3 A new preclinical model system: DMG brain organoids

3.3.1 DBO generation protocol

To introduce DMG cells into a brain-like microenvironment, tumor spheres were co-cultured with developing cerebral organoids (Figure 8A). Human induced pluripotent stem cells were first differentiated to embryoid bodies (EBs) in which neuroepithelium was subsequently induced. In parallel, BT869 cells were seeded and grown to sufficiently large spheres. From day seven, the EB and the tumor sphere were co-cultivated in a multiwell plate. By using an expansion medium with matrigel, the neuroepithelium of the early cerebral organoid was further expanded, while the tumor cells began to fuse with it, starting the DBO formation. After embedding in matrigel droplets on day 10, DBOs were expanded for at least 50 additional days with constant shaking in 6 well plates. During this period, the tumor cells completely fused with the cerebral organoid and formed approximately 3 mm thick DMG brain organoids (Figure 8B-C).

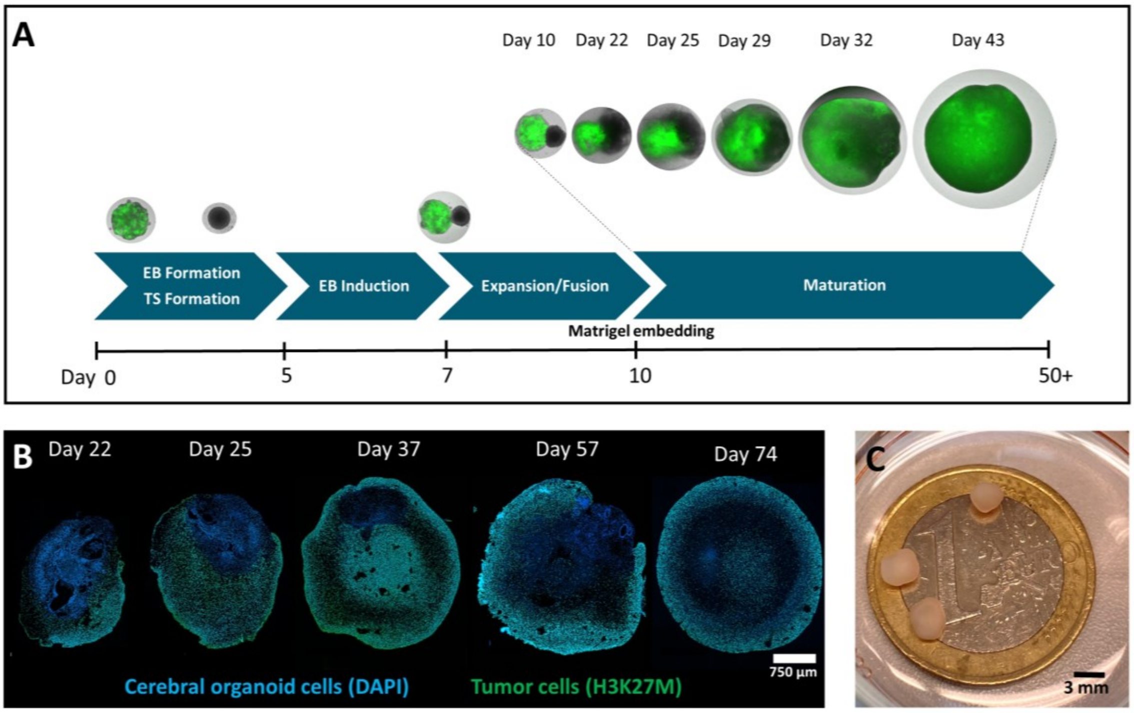

Figure 8: Generation of DMG brain organoids. **A**: Schematic of DBO generation by co-culturing tumor cell spheres (BT869 ZsGreen labelled cells) with developing cerebral organoids. **B**: CODEX images of different DBO cultivation time points. Shown are DBO sections with tumor cells in green (H3K27M) fusing with the cerebral organoid in blue (DAPI) with increasing co-culture time. **C**: Representative image of fully fused DBOs.

3.3.2 Co-culture effects on tumor cell composition in DBOs.

To monitor the effects of co-culture on tumor cell populations, DBO sections from different culture time points were analyzed using the CODEX system. In the early stages of co-culture, BT869 tumor cells were mainly composed out of OPC-like cells (85 %). Only 11 % showed OC-like characteristics, while AC-like cells represented the smallest population at 3 % (Figure 9). This composition changed over time and OPC-like cell levels steadily decreased to a percentage of 40 % by day 74. Meanwhile, the AC-like population increased to approximately 40 %, whereas the OC-like population only increased slightly, fluctuating between 21 % and 29 % from day 43.

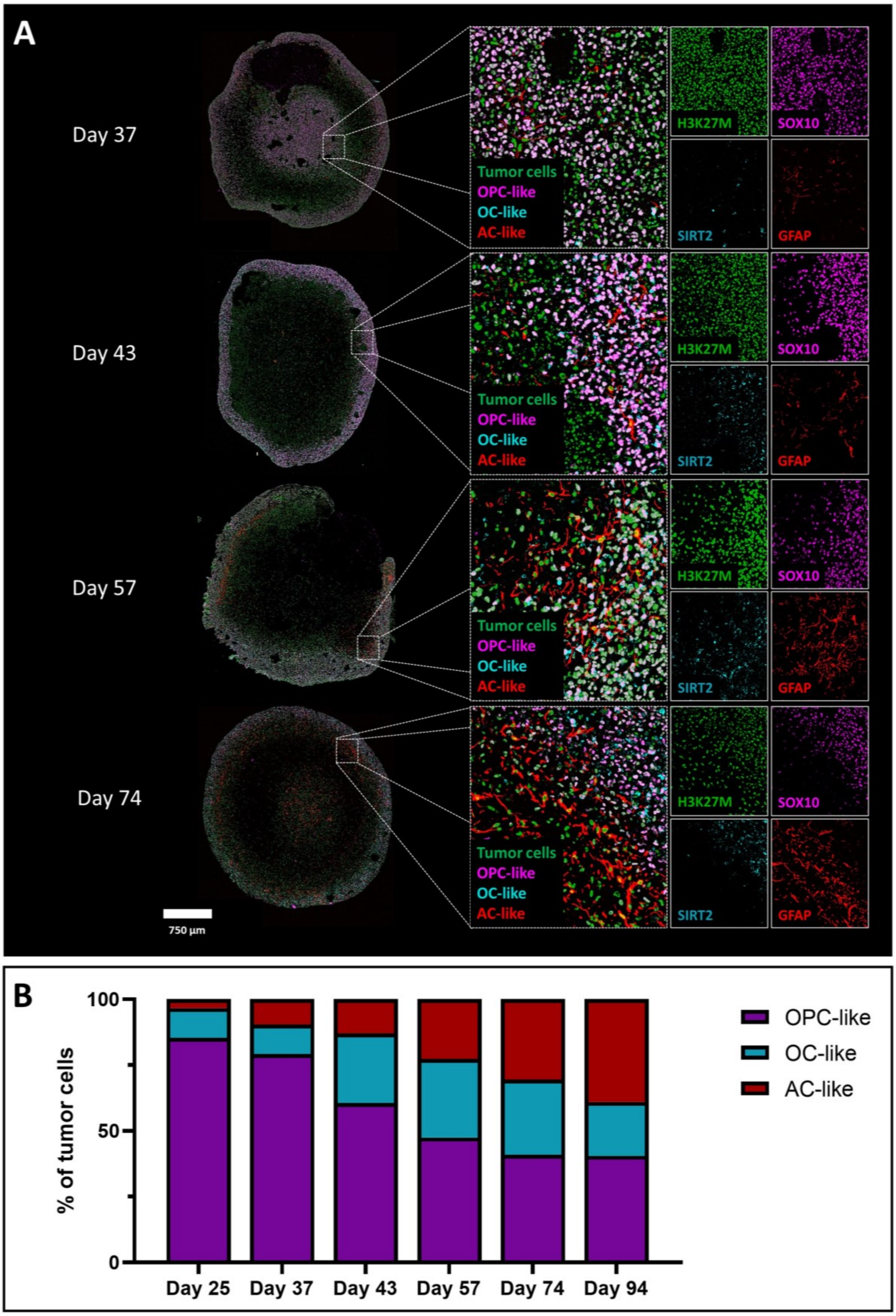
A
Day 37
Day 43
Day 57
Day 74
Tumor cells
OPC-like
OC-like
AC-like
H3K27M
SOX10
SIRT2
GFAP
750 µm
B
100
50
0
% of tumor cells
Day 25
Day 37
Day 43
Day 57
Day 74
Day 94
OPC-like
OC-like
AC-like

Figure 9: Changes of tumor cell composition during DBO culture. **A**: Representative CODEX images of DBO sections from different time points during the culture period. Tumor cells (BT869) are shown in green (H3K27M signal), while GFAP in red represents AC-like cells, SIRT2 in cyan represents OC-like cells, and SOX10 in magenta represents OPC-like cells. **B**: Assessment of tumor cell composition during DBO culture. Between 4.000 to 30.000 tumor cells were analyzed per time point (one section from one DBO per time point), combining cell numbers from three different protein markers for each population calculation.

The number of actively proliferating cells also showed dynamic fluctuations. While approximately 66 % of tumor cells were proliferating on day 25, this percentage decreased to 25 % by day 57 (Figure 10).

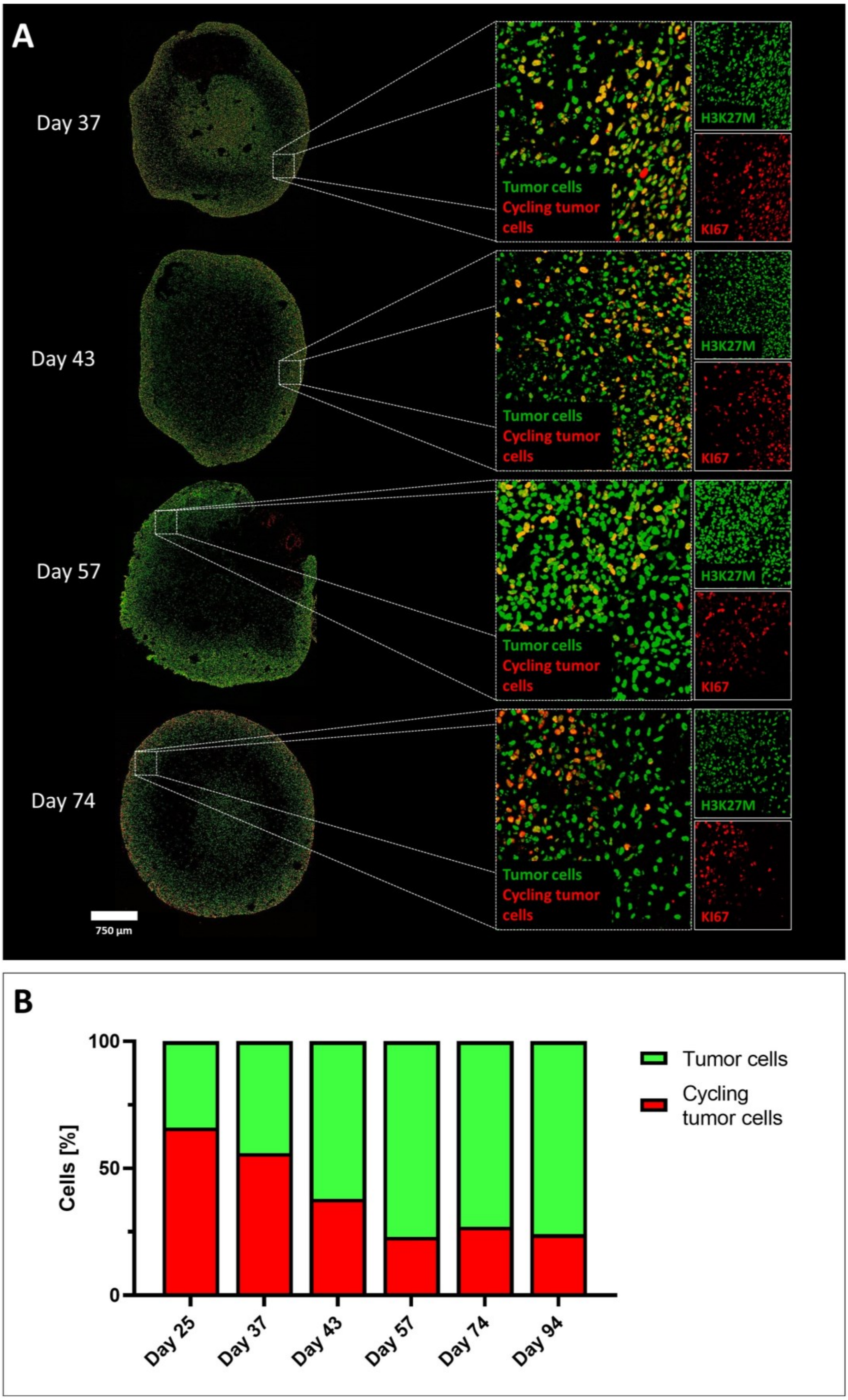

Figure 10: Tumor cell proliferation rates during DBO culture. **A** shows CODEX images from early to late time points of DBO culture. While BT869 tumor cells are shown in green (H3K27M), the proliferation marker KI67 is displayed in red. **B**: Bar graphs of total tumor cell proliferation rates. For quantification, 4.000 to 30.000 cells were analyzed from one section of one DBO per time point.

3.4 Comparing cell composition of DMG models to primary tumor samples.

To evaluate the newly generated DBO model, tumor cell composition data from CODEX analysis was compared with data from primary DMG tumors and already established model systems such as sphere culture and the PDX model. In case of all DMG models, the BT869 cell line was used. The main populations in the primary DMG samples were AC-like and OPC-like tumor cells. AC-like cells accounted for 46 % of tumor cells and OPC-like cells followed with 31 %. OC-like cell fractions represented 23 % as the smallest subpopulation (Figure 11). When looking at the composition of tumor cells in the DBO model, a similar picture was observable with AC-like (36 %) and OPC-like (37 %) cells being predominantly present. Less AC-like cells were detectable compared to the tumor and the population size was rather comparable to the one of the OPC-like cells. Similar to the tumor samples, OC-like cells accounted for the smallest subpopulation in DBOs with a percentage of 27 %. Observing BT869 cells in sphere culture or in the PDX model showed population shifts compared to the primary tumor (Figure 11). A substantially increased proportion of BT869 tumor cells in sphere culture exhibited OPC-like properties (80 %). OC-like cells were slightly less detectable at 19 %, while almost no cells could be assigned to the AC-like population (1 %). In the PDX mouse model, however, the OC-like subpopulation dominated and was twice as high as in the tumor with 48 %. Comparable 30 % of OPC-like cells and only half as many AC-like tumor cells (22 %) could be identified.

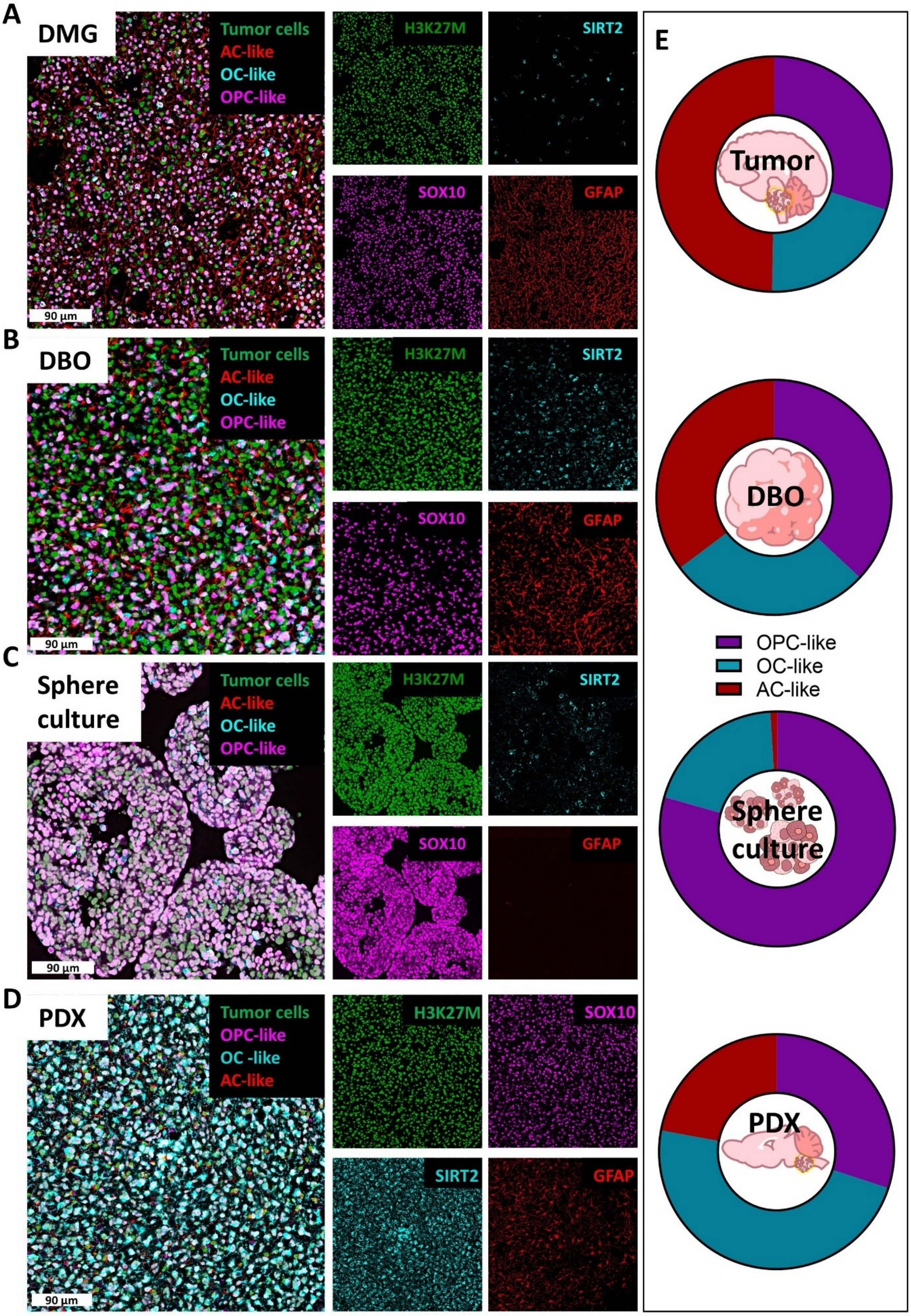
A
DMG
Tumor cells
AC-like
OC-like
OPC-like
H3K27M
SIRT2
SOX10
GFAP
90 µm
B
DBO
Tumor cells
AC-like
OC-like
OPC-like
H3K27M
SIRT2
SOX10
GFAP
90 µm
C
Sphere culture
Tumor cells
AC-like
OC-like
OPC-like
H3K27M
SIRT2
SOX10
GFAP
90 µm
D
PDX
Tumor cells
OPC-like
OC -like
AC-like
H3K27M
SOX10
SIRT2
GFAP
90 µm
E
Tumor
DBO
OPC-like
OC-like
AC-like
Sphere culture
PDX

Figure 11: Comparison of cellular composition between primary DMG tumors, the new DBO model, and current DMG models (sphere culture, PDX). **A**-**D** show representative CODEX images from a primary DMG tumor and the analyzed model systems (DBO, sphere culture and PDX). Tumor cells are labeled in green by H3K27M. OPC-like tumor cells are indicated by SOX10 in magenta. OC-like cells are represented by SIRT2 in cyan and AC-like tumor cells by GFAP in red. **E**: CODEX evaluation of tumor cell composition of primary DMGs and model systems. The tumor pie chart summarizes cell numbers of all seven tumors (Figure 4) with a total 1.26 million analyzed DMG cells. For the DBO pie chart, six tumor organoids from four different batches were analyzed (150.000 analyzed tumor cells). Sphere culture and PDX analysis from Figures 6 and 7 are displayed as pie charts. All subpopulations combine cell numbers from three different marker proteins.

3.5 Drug treatment regimen and effect evaluation using the DBO culture system

3.5.1 Drug effects on tumor burden and cycling tumor cells

To analyze individual treatment effects of potentially interesting drug candidates for DMG therapy, a 14-day long treatment regimen with regular re-treatments for consistent drug efficacy was developed (see Figure 12A and methods 2.2). Two parameters based on the evaluation of fluorescence microscopic images of DBO sections (representative images in Figure 12) were used as read out for individual drug effects: tumor burden reduction and proliferation rate of the remaining tumor cells. Decrease in tumor burden of DBOs was measured based on the change in areas occupied by H3K27M-positive (specific tumor cell marker) nuclei relative to the control DBOs (see overview in Figure 13A). Tumor burden was decreased drug-specific by values ranging from not significant 5 % with 100 nM adavosertib, to highly significant ($p \leq 0{,}0005$) reductions of 50 % with 100 nM gemcitabine and 97 % with 100 nM delanzomib (images in Figure 12B-E and analysis in Figure 13A). Furthermore, the number of tumor cell nuclei with positive proliferation marker (KI67) staining was determined to assess the proliferation ability of DMG cells after drug treatment (see overview in Figure 13B). While around 34 % of malignant cells were actively cycling in control DBOs, drug treatments were able to significantly inhibit proliferation down to 1 % and below (e.g. panobinostat and delanzomib at 100 nM, $p \leq 0{,}0005$). A total of 30 drugs were used for DBO treatments in two different concentrations each. Generally, the drug selection was based on a recent preclinical high-throughput drug screen with H3K27-alterd DMG cells that identified portent compounds (Lin et al., 2019) and on and most recent information available from clinical trials at onset of the project. Overall, individual drugs showed dose dependent effects on tumor burden and cell proliferation (Figure 13A and B).

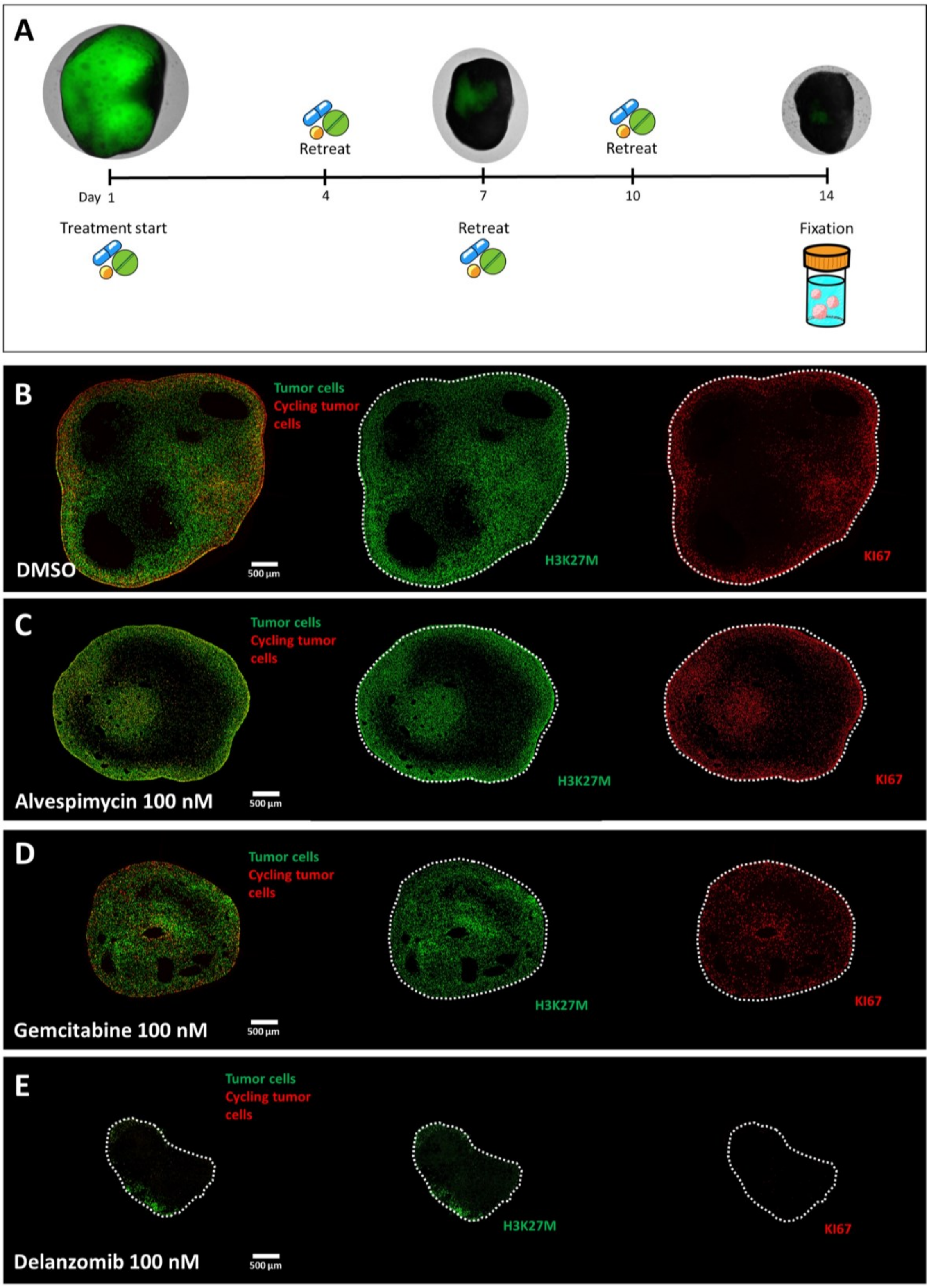

Figure 12: Drug treatment regimen and drug-specific effects on DMG tumor cells in DBO culture. **A**: Overview of the 14-day drug treatment regimen. The images show a DBO during different time points of treatment. Green signal originates from ZsGreen-labeled DMG cells (BT869). **B-E**: Representative fluorescence stainings of DBOs after treatments with 100 nM alvespimycin (C), 100 nM gemcitabine (D) or 100 nM delanzomib (E). B shows a DMSO treated control DBO. Tumor cells are stained in green by the H3K27M signal, while proliferating cells are shown in red by KI67.

Most potently, the higher concentrations of ten drugs used reduced tumor mass significantly to 25 % and less (Figure 13C). This group was led by the compounds daporinad (94 % reduction) and romidepsin (85 % reduction) in low concentrations of 10 nM, followed by delanzomib (representative image see 12E) and GMX-1778 with tumor mass reductions of 97 % and 90 % at 100 nM, respectively. Treatments with 1000 nM dinaciclib, rigosertib, cevipabulin, ON206 or PF-03814735 also greatly reduced tumor burden by levels between 80 % to 95 %.

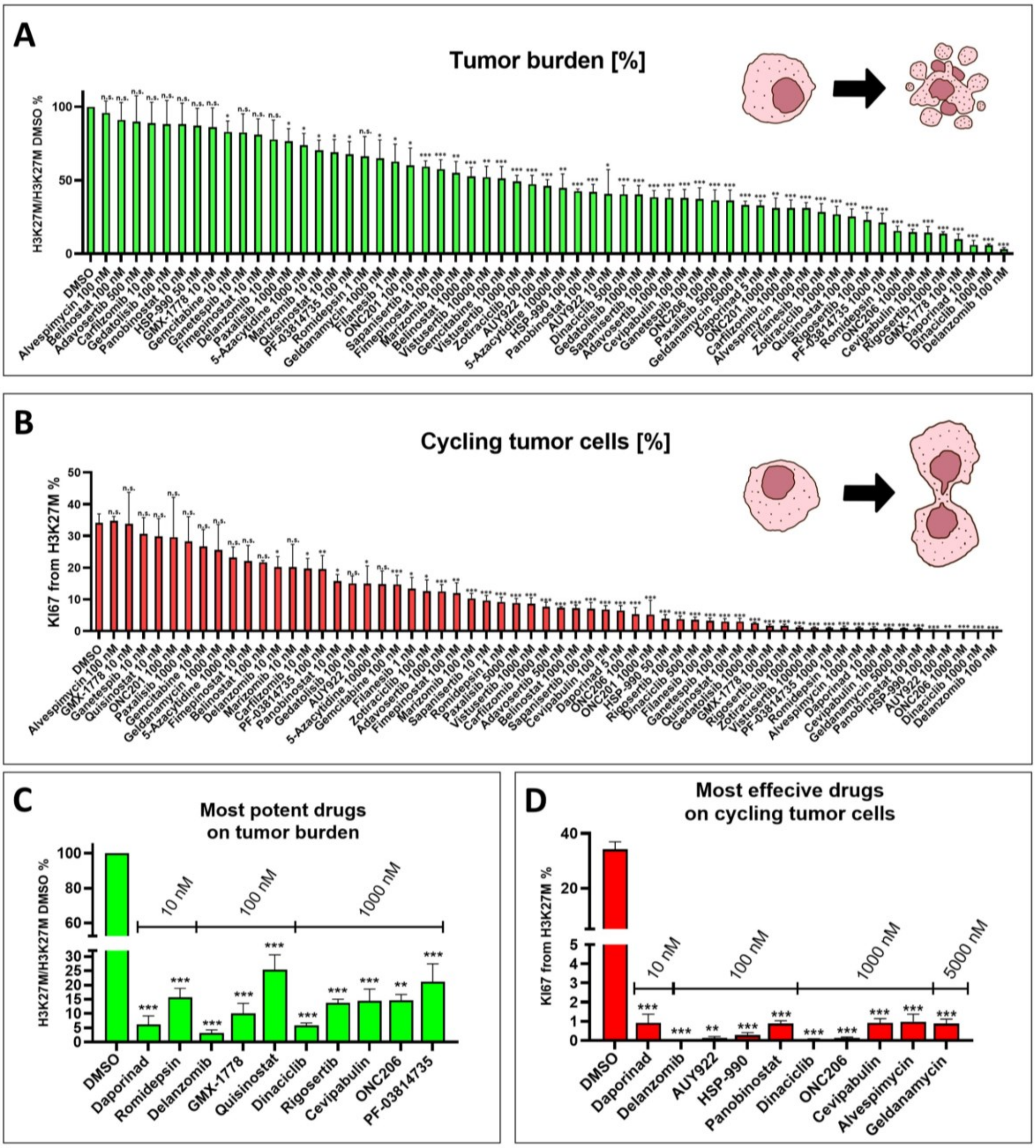

Figure 13: Drug effects on DBO tumor burden and proliferation. A: Decrease in DBO tumor burden relative to control (DMSO) as measured by the area of the tumor cell specific H3K27M fluorescent signal in DBO sections. A total of 30 different drugs in two different concentrations are listed. The ten most potent drugs are summarized in C, sorted by concentration. B shows the decreasing proliferation rates of all 30 drug treatments, and the ten drugs that induce the strongest inhibition of proliferation are grouped by concentration in D. Shown is the percentage of proliferation marker (KI67) positive tumor area (H3K27M signal) of the normalized tumor burden values. n = six DBOs per drug concentration from two independent differentiation and treatment rounds (three DBOs per treatment round). Error bars represent the standard error of the mean (SEM). Unpaired two-sided t-tests were performed to compare treatments with the DMSO controls: n.s. = not significant; * = p ≤ 0,05; ** = p ≤ 0,005; *** = p ≤ 0,0005.

Most of the just mentioned drugs were also found among the top 10 compounds significantly inhibiting the proliferation of tumor cells (less than 1 % of cycling tumor cells, Figure 13D). However, the compounds AUY922, HSP990, panobinostat, alvespimycin and geldanamycin also showed low proliferating tumor cell fractions in this range, but tumor burden was reduced by only about half (Figure 13A-B). This observation led to the introduction of the proliferation ratio value to provide better insight into the relation of total tumor mass to proliferative tumor cells. Values were calculated by dividing the individual tumor mass proportion by the percentage of proliferating tumor cells. As the value increases, the proportion of dividing tumor cells decreases in relation to the tumor mass, allowing easier conclusions about the proliferation-inhibiting effect of individual drugs. High proliferation ratios were predominantly observed at the highest dose of each drug (the corresponding values are shown in Table 3). Half of the drugs showed at least a fivefold increase in proliferation ratio compared to the control, indicating enhanced proliferation inhibition of remaining tumor cells. This drug pool consisted largely of the drug candidates with strong tumor burden and or proliferation reducing abilities (from Figure 13C and D). When looking at the drug-specific mechanisms of action, all five HSP90 inhibitors used in this project were found under those candidates. The HSP90 inhibitor AUY922 exhibited the strongest inhibitory effect of all drugs with a value of 370,9, followed by HSP90 inhibitor HSP-990 with 154,6. A relatively heterogeneous mix of mechanisms of action was found for the remaining potent drug candidates. Both the proteasome inhibitor delanzomib and the DRD2 antagonist ONC206 showed strong proliferation inhibitory effects with ratios of 129,7 and 119,1. However, drugs such as the cyclin-dependent kinase (CDK) inhibitor dinaciclib and the HDAC inhibitor panobinostat also stood out here with high values of 87,4 and 48,2.

Table 3: Antiproliferative drug effects on DMG cells in DBO culture. The table shows all drugs tested, sorted by their antiproliferative activity. The proliferation inhibition ratios were calculated by dividing the percentages of tumor burden by the percentages of proliferating tumor cells. Main mechanisms of action are noted, as well as used drug concentrations.

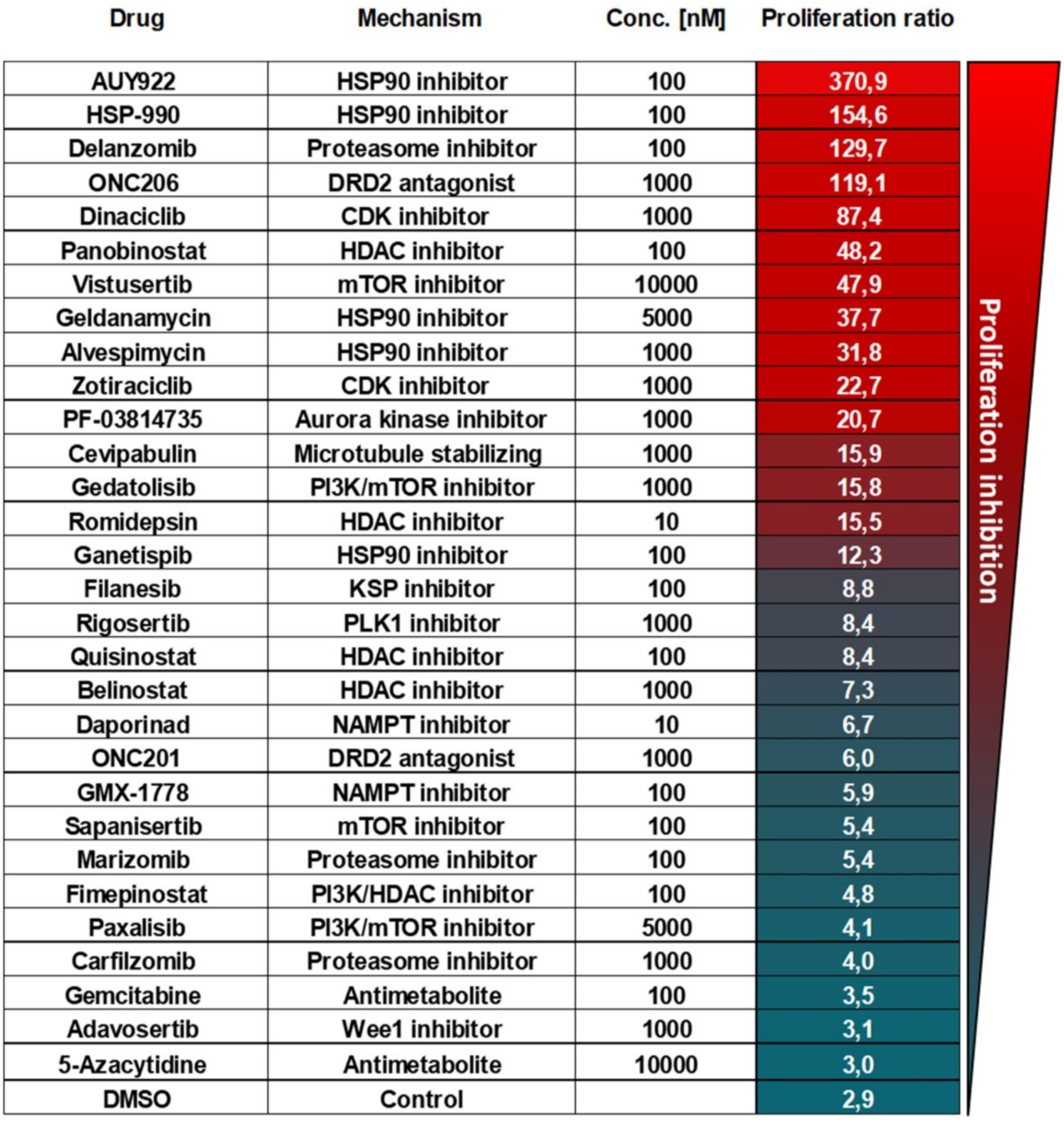

Drug	Mechanism	Conc. [nM]	Proliferation ratio
AUY922	HSP90 inhibitor	100	370,9
HSP-990	HSP90 inhibitor	100	154,6
Delanzomib	Proteasome inhibitor	100	129,7
ONC206	DRD2 antagonist	1000	119,1
Dinaciclib	CDK inhibitor	1000	87,4
Panobinostat	HDAC inhibitor	100	48,2
Vistusertib	mTOR inhibitor	10000	47,9
Geldanamycin	HSP90 inhibitor	5000	37,7
Alvespimycin	HSP90 inhibitor	1000	31,8
Zotiraciclib	CDK inhibitor	1000	22,7
PF-03814735	Aurora kinase inhibitor	1000	20,7
Cevipabulin	Microtubule stabilizing	1000	15,9
Gedatolisib	PI3K/mTOR inhibitor	1000	15,8
Romidepsin	HDAC inhibitor	10	15,5
Ganetispib	HSP90 inhibitor	100	12,3
Filanesib	KSP inhibitor	100	8,8
Rigosertib	PLK1 inhibitor	1000	8,4
Quisinostat	HDAC inhibitor	100	8,4
Belinostat	HDAC inhibitor	1000	7,3
Daporinad	NAMPT inhibitor	10	6,7
ONC201	DRD2 antagonist	1000	6,0
GMX-1778	NAMPT inhibitor	100	5,9
Sapanisertib	mTOR inhibitor	100	5,4
Marizomib	Proteasome inhibitor	100	5,4
Fimepinostat	PI3K/HDAC inhibitor	100	4,8
Paxalisib	PI3K/mTOR inhibitor	5000	4,1
Carfilzomib	Proteasome inhibitor	1000	4,0
Gemcitabine	Antimetabolite	100	3,5
Adavosertib	Wee1 inhibitor	1000	3,1
5-Azacytidine	Antimetabolite	10000	3,0
DMSO	Control		2,9

A closer look at the fluorescence data off all drugs with a proliferative value above 10 revealed two different treatment effects at drug-specific doses. On the one hand, antiproliferative drugs that reduced tumor mass by only 50 % to 70 %, but almost completely inhibited proliferation of remaining tumor cells (Figure 14D). The most potent members of this class of drugs were AUY922, HSP-990, panobinostat, and ganetespib at 100 nM. On the other hand, drugs were found that also strongly inhibited proliferation, but primarily reduced tumor mass by at least 80 % (Figure 14E). This was observed with the drug treatments of romidepsin at a low concentration of 10 nM, delanzomib at 100 nM and dinaciclib, cevipabulin, ONC206, and PF-03814735 at 1000 nM.

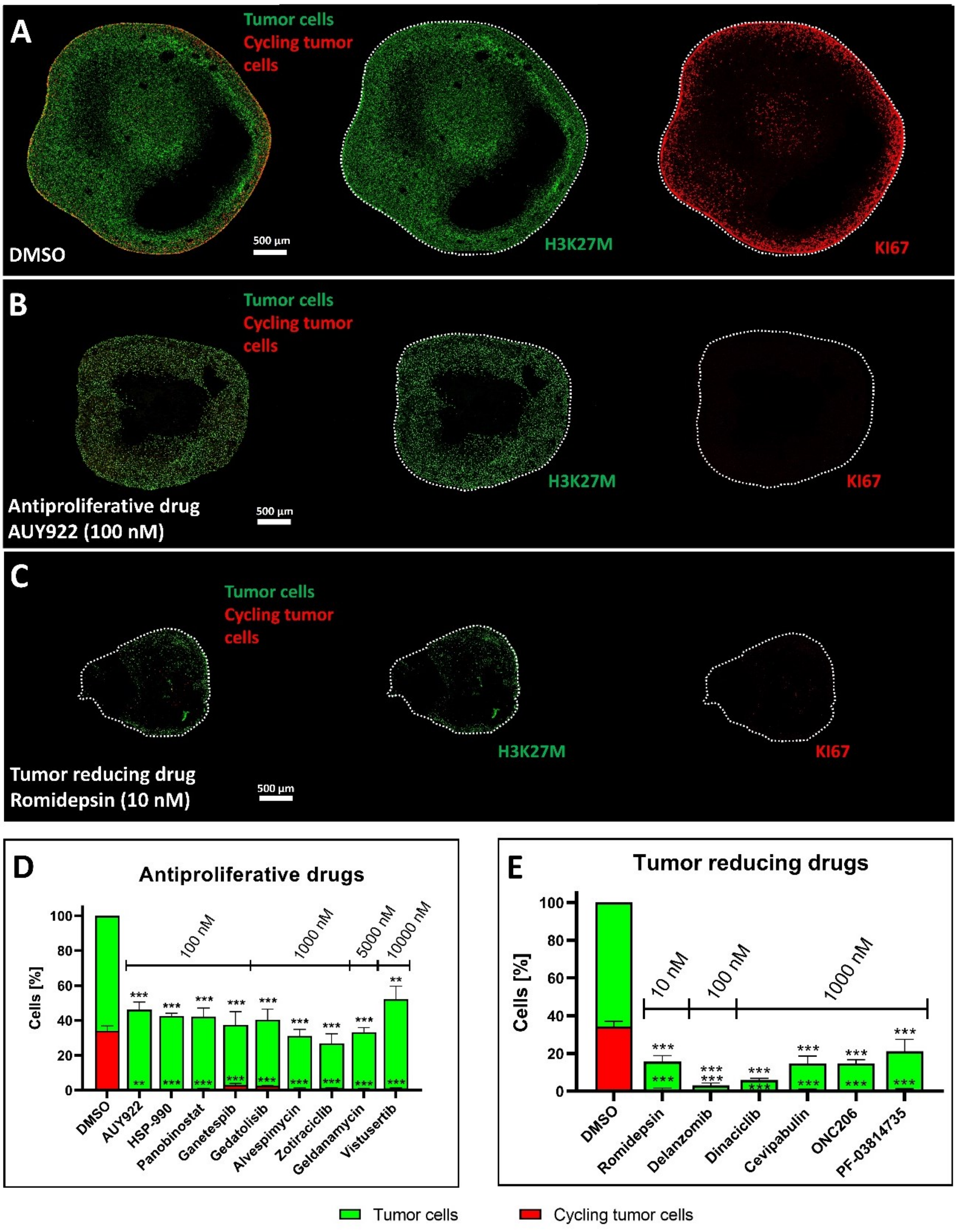

Figure 14: Tumor reducing and antiproliferative drug candidates. **A** to **C** show representative fluorescence images of DBO treatments. While A shows a control DBO, B represents an example of antiproliferative drug action with AUY922. An example of strong tumor mass reduction is shown under C with daporinad. Tumor cells are stained in green by the H3K27M signal, while proliferating cells are shown in red by the KI67 stain. A bar graph of all antiproliferative drugs sorted by concentration is presented in **D**, whereas **E** shows the same for drugs with a tumor reducing effect. In both cases, tumor mass is normalized to the control and shown in green. The corresponding proportions of proliferating tumor cells are shown in red. n = six DBOs per drug concentration, originating from two independent differentiation and treatment rounds (three organoids per treatment round). Error bars represent the standard error of the mean (SEM). Unpaired two-sided t-tests were performed to compare treatments with the DMSO controls regarding tumor burden and proliferation reduction: n.s. = not significant; * = p ≤ 0,05; ** = p ≤ 0,005; *** = p ≤ 0,0005.

3.5.2 Drug-specific treatment effects on DBO tumor cell composition

In order to further characterize the drug-specific effects, the cell composition in DBOs was also investigated after treatment using the CODEX system. A total of seven drugs were selected for this purpose, which were of particular interest from clinical perspective at the time of analysis. To reliably analyze drug-specific effects on tumor cell subpopulations, an individual concentration was chosen for each drug based on data from the DBO treatments (Figure 13A and B), which left sufficient tumor cell numbers for the CODEX analysis. All drug treatments reduced individual subpopulation to varying degrees, resulting in altered tumor cell compositions (Figure 15).

It was found that 100 nM marizomib reduced mainly OC- and OPC-like populations. While OC-like cells were reduced by 73% and OPC-like cells by 68%, the number of AC-like cells only halved compared to the controls. Consequently, the composition of DBO tumor cells after marizomib treatment showed a higher percentage of AC-like cells (51%) and lower proportions of OPC- and OC-like tumor cells (32% and 17%) compared to the control DBOs. In contrast, 100 nM of zotiraciclib and ONC206 reduced all subpopulations relatively equally. Both drugs induced greater reductions in AC-like cells when compared to marizomib (ranging between 56 % and 58 %), while OC-like and OPC-like cells were less affected (OC-like reduction 65 % - 66 % and OPC-like reduction 58 % - 60 %). Tumor cell composition remained relatively unchanged after zotiraciclib treatment compared to the control DBOs, while ONC206 showed a slight shift towards AC-like cells (42 %). Paxalisib caused greater population reductions compared to the compounds just mentioned, but at a significantly higher concentration of 5000 nM. While OPC-like was the most affected tumor subpopulation here (reduced by 80 %), AC-like cells were least affected with 65 % of reduction. Therefore, compared with controls, the DBO cell composition contained an increased proportion of AC-like cells (47%), whereas the OPC-like population was less represented at 26%. In the case of 100 nM fimepinostat, there was a sharp decrease in OC-like cells by 80%. The second most reduced subpopulation here was the OPC-like (by 79%), and the AC-like cells were the least affected with a decrease of 67%. This resulted in a tumor cell composition with increased AC-like proportions (50%) and reduced OC-like proportions of 15% compared to DMSO-treated DBOs. This low proportion of OC-like cells was further reduced by the administration of 100 nM panobinostat, which had the highest reduction rate of 99.3% compared to all drugs. OPC-like and AC-like cells were reduced to a greater extent compared to fimepinostat at 99% and 72%, again with AC-like cells being reduced the least within the panobinostat treatment. Thus, tumor cell composition shifted strongly toward AC-like cells (63%), while the proportion of OC-like cells (14%) decreased compared to control DBOs, followed by OPC-like cells at 22%. 1000 nM of ONC201 reduced especially OPC-like cells by a high 99 %, while the OC-like population was slightly less impacted than with panobinostat, but also strongly reduced by 88 %. AC-like cells were reduced the least within the ONC201 treatment (by 73%), resulting in a tumor cell composition with increased AC-like proportions of 63% compared to control DBOs. Both OC- and OPC-like populations were comparatively less represented here at 14% and 22%, respectively.

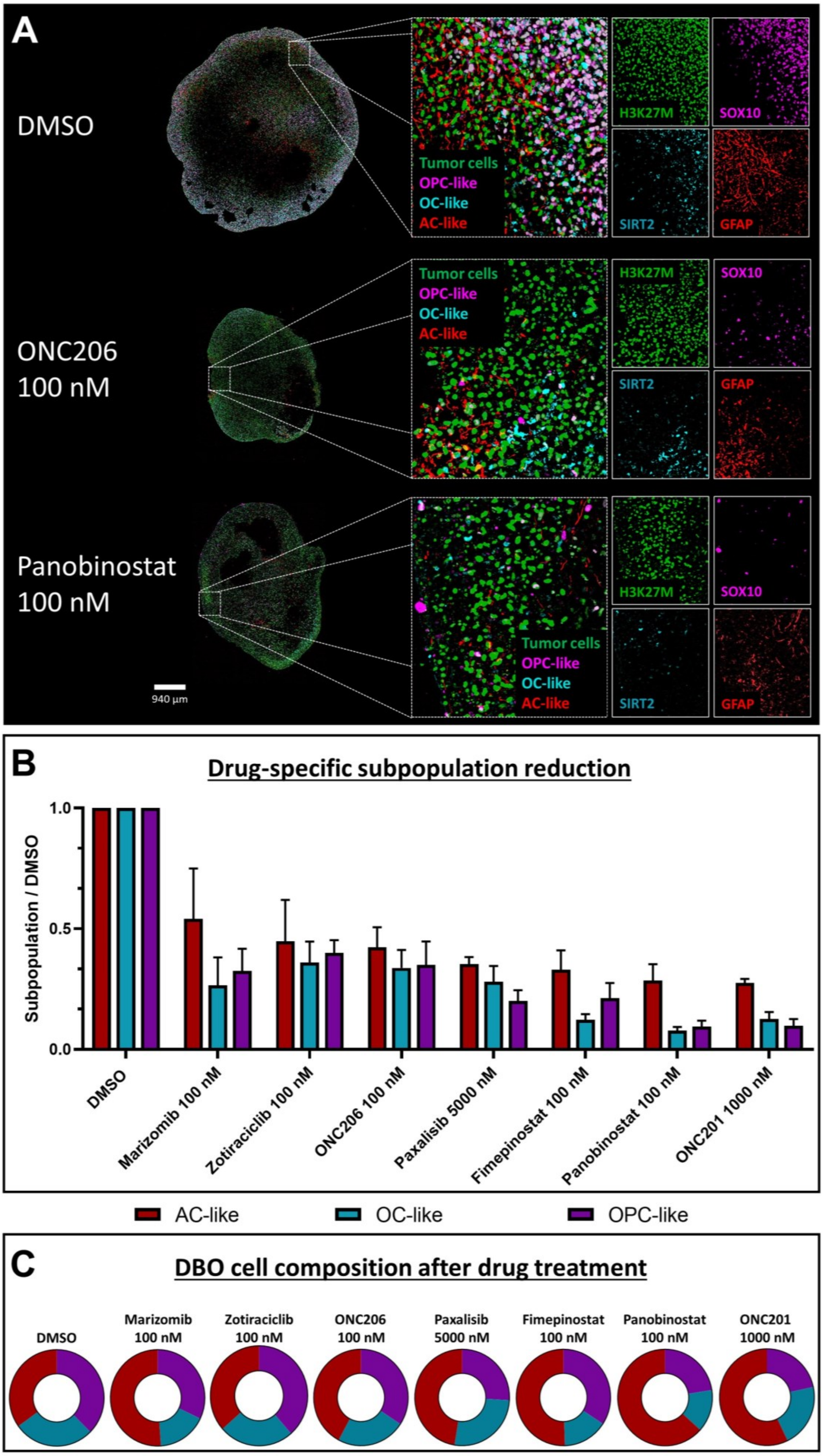
A
DMSO
Tumor cells
OPC-like
OC-like
AC-like
H3K27M
SOX10
SIRT2
GFAP
ONC206
100 nM
Panobinostat
100 nM
940 µm
B
Drug-specific subpopulation reduction
Subpopulation / DMSO
1.0
0.5
0.0
DMSO
Marizomib 100 nM
Zotiraciclib 100 nM
ONC206 100 nM
Paxalisib 5000 nM
Fimepinostat 100 nM
Panobinostat 100 nM
ONC201 1000 nM
AC-like
OC-like
OPC-like
C
DBO cell composition after drug treatment
DMSO
Marizomib
100 nM
Zotiraciclib
100 nM
ONC206
100 nM
Paxalisib
5000 nM
Fimepinostat
100 nM
Panobinostat
100 nM
ONC201
1000 nM

Figure 15: Effects of drug treatment on DMG cell composition in DBO culture. **A** shows representative CODEX images of DBO treatments (control, panobinostat, ONC206). Tumor cells are labeled with H3K27M signal in green, the subpopulation of AC-like tumor cells is represented by GFAP in red and OC-like tumor cells are shown in cyan by SIRT2 signal. The cells of the OPC-like fraction are represented by SOX10 in magenta. **B** and **C** show CODEX analysis data of DBO treatments. In B, the cell numbers of each subpopulation are normalized to the DMSO controls to quantify the reduction in each population. C shows the tumor cell compositions after treatment. All subpopulations contain the cell numbers of three different markers. n = four DBOs per drug from two independent differentiation and treatment rounds were used. Analyzed tumor cell numbers: DMSO 120.000, Marizomib 46.000, Zotiraciclib 71.000, ONC206 72.000, Paxalisib 40.000, Fimepinostat 33.000, Panobinostat 32.000, ONC201 37.000. Error bars represent the standard error of the mean (SEM).

4. Discussion

The goal of this work was to develop a new H3K27-altered DMG *in vitro* model for drug testing. By providing a human brain-like TME for tumor cells and generating a tumor cell composition comparable to that of primary tumor samples, a realistic drug response should be achieved. This could contribute to improve the predictive power of preclinical drug testing, enhancing the translation of drug candidates into DMG treatment schemes.

4.1 DBOs as representative model for H3K27-altered DMG

Previous single-cell RNA-seq data revealed the composition of tumor cells in H3K27-altered DMGs and showed AC-like, OC-like, and OPC-like populations (Filbin et al., 2018). The presented CODEX tumor cell analysis of primary H3K27-altered DMGs also showed this specific composition of AC-, OC- and OPC-like cell fractions, with the AC-like population being the most abundant malignant cell type on average. In contrast, OPC-like cells represented the most prevalent cell type in the publication from Filbin et al., 2018. The reason for this difference in population distribution could be the use of different analysis systems (single-cell RNA- seq vs. CODEX). Thus, an increased occurrence of AC-like tumor cells in H3K27-alterd DMGs was also observed in the newest work from the Filbin lab, where spatial transcriptomics and CODEX analysis were used in addition to single cell (sc)RNA-sequencing (Liu et al., 2022). Interestingly, in contrast to the RNA-seq data, significantly more AC-like cells were detected with the spatial transcriptomics and CODEX approaches. Liu et al. hypothesized that this might be due to the fact, that AC-like cells tend to form more cell interconnections, which makes them specifically vulnerable to cell dissociation for sequencing. Therefore, it is possible that more OPC-like cells survived the dissociation, leading to biased scRNA-seq data. This highlights the strength of the used CODEX system, which leaves the tissue architecture untouched for single cell analysis and thus avoids potential enrichment of a single subpopulation by dissociation. Nevertheless, OPC-like cells still accounted for large numbers of malignant cells in the analyzed H3K27-altered DMGs and their undifferentiated, stem-like tumor driving role likely contributes to the aggressiveness of the tumor and the poor therapy response. Numbers of actively dividing tumor cells ranged from 5 % to 16 % in the presented data. Filbin et al., 2018 also found similar proliferation rates in the majority of cases, but H3K27-altered DMGs with rates above 20 % were also present. This could indicate an intertumoral variation in proliferation rates.

In this work, two standard H3K27-altered DMG model systems for drug testing were analyzed for their individual tumor cell composition and compared to primary tumor samples. The analysis of patient derived tumor cells, either cultured as spheres or in an orthotopic PDX model, revealed clear subpopulation shifts compared to primary tumor samples.

Sphere cultured BT869 cells almost entirely consisted out of more de-differentiated OPC-like and actively cycling cells compared to primary tumor samples. This indicates that the special conditions of cell culture, such as growth outside of a natural microenvironment or factors from cell culture medium, can have a decisive influence on the tumor cell composition. This finding is consistent with data from glioblastoma cells, where sphere culture specifically enriches a more de-differentiated, stem cell-like tumor cell state (Joseph et al., 2021). The use of patient-derived cell lines offers many advantages for drug testing (Ferreira et al., 2013). The simple and cheap handling, as well as the availability of almost unlimited numbers of cells for experiments, is especially relevant for rare tumor entities such as H3K27-altered DMG, where tissue availability is severely limited. However, the different cell composition and proliferation status could affect drug efficacy, as seen in other cancer cells (Granada et al., 2020). Therefore, considering the decisively differed tumor composition of sphere cultures, the predictive power in terms of tumor response to drugs should be taken with caution here.

A characteristic feature that is missing in sphere culture is the brain specific TME. The TME has a very heterogenous composition and contains cellular (e.g. non-malignant cell types like cells of the nervous system, immune cells, vascular cells, stroma cells) as well as non-cellular components (e.g. ECM). Properties of the ECM like stiffness and direct/indirect interactions (e.g. neuronal activity) with various non-malignant cell types can have a decisive influence in the characteristics of tumor cells (Langhans, 2018; Venkatesh et al., 2015). Therefore, it is conceivable that tumor cell differentiation and thus the subpopulation composition can be crucially influenced by the TME. This was also indicated by the CODEX analysis of the BT869 cells from sphere culture injected in the microenvironment of the mouse pons (PDX model was generated by the Filbin laboratory). In contrast to sphere culture, the PDX model showed a significantly more differentiated and less proliferative composition of BT869 cells in the presented data. This suggests that factors and components from the *in vivo* mouse brain environment significantly influence tumor cell state and are able to restore a more tumor-like cell composition. However, the OC-like population was much more prevalent compared to the primary tumor tissue. Causal for the OC-like population shift in the analyzed DMG PDX model could be the mouse specific microenvironment, influencing tumor cell states in a specific way. Indeed, results from Ben-David et al. 2017 suggest that PDX culture of fresh tumor cells over a prolonged period of time can promote a mouse-specific tumor evolution that differs from primary tissue. The non-human mouse environment can therefore lead to tumor subclone selection (Ben-David et al., 2017; Sun et al., 2021), thus shifting the tumor cell composition and potentially altering the drug response of malignant cells. However, it should be noted that access to mouse material was limited and analysis of additional PDX samples would be of interest to see if the tumor cell population shift frequently occurs.

To bring the phenotype of the BT869 cells even closer to tumor-specific differentiation patterns, they were placed in a human brain-like microenvironment. Therefore, the DMG cells were co-cultured with human cerebral organoids. The generation procedure of cerebral organoids has been available since 2013 and is a well characterized and standardized iPSC differentiation protocol (Lancaster et al., 2013; Lancaster & Knoblich, 2014). Cells recapitulate the essential steps of human brain development and form functional neurons as well as a realistic tissue organization (Lancaster et al., 2013). BT869 cells infiltrated the developing cerebral organoid over time, resulting in DMG brain organoids (DBOs). These altered culture conditions caused a decrease of more de-differentiated OPC-like and highly proliferating cell fractions, while the number of more differentiated AC-like tumor cells increased. Thus, the DBO culture led to a closer reflection of tumor cell composition as seen in primary DMG tumor samples. Similar effects on tumor cell states were observed with the use of glioblastoma cell lines. Pine et al. 2020 analyzed glioblastoma cells fused with cerebral organoids (GLICO model from Linkous et al., 2019) and were able to detect similar cell compositions compared to primary tumor tissue. The observed heterogeneity of malignant cells was present only in the GLICO model when compared to other model systems (e.g. conventional 2D cell culture), as a direct consequence of the human brain-like microenvironment. This could also be the cause for the tumor-like cell composition in case of the presented DBO model. Properties of the TME (e.g. stiffness and composition) are known to influence tumor cell phenotypes (Langhans, 2018) and might therefore contribute to the more pronounced differentiation of tumor cells in the DBO model. In addition, concentration gradients (e.g. oxygen, pH, nutrients), as a result of the 3D structure of the DBOs, might also mediate mechanisms which influence the tumor cell composition (Langhans, 2018; Qiu et al., 2017).

In conclusion, DBOs closely resembled the tumor cell composition of primary tumor tissue, thus providing a representative organoid model for H3K27-altered DMGs. Due to the *in vitro* nature of the system, no complicated implantation procedures into a nonspecies microenvironments of animal models are needed and consequent ethical issues are avoided. Furthermore, artificial conditions and associated, undesirable influences on tumor cell composition of standard *in vitro* culture are minimized, while maintaining the relative ease of use. However, the DBO model system is just an approximation of reality and the provided TME for tumor cells is still simplified in composition. Furthermore, decisive brain-specific features such as a blood-brain barrier are missing in comparison to the PDX model. Adding further components like vasculature or immune cells would therefore further improve the model. In addition, it would be of interest for future experiments to analyze if the DBO culture system also induces tumor specific cell compositions in other patient derived cell line. As the presented data only show results for BT869 cells, analysis of additional DMG cell lines or other brain tumor cell lines would be beneficial to further confirm the observed effects on tumor cell composition.

4.2 Antitumor properties of drugs in the DBO culture system

To investigate how H3K27M cells in DBO culture respond to different drugs, DBOs were treated for 14 days with a selection of 30 interesting drug candidates. Potent compounds, identified in a high-throughput screening by Lin et al., 2019 were evaluated for DBO treatment selection using the latest information available from clinical trials at start of the project (e.g. planned or present use in DMG trials). Readouts from DBO treatments based on fluorescence imaging, not only allowed a detailed assessment of individual drug potencies (tumor mass reduction) but also revealed effects on treatment surviving cells (cycling tumor cell numbers and tumor cell composition). This could be beneficial for identifying new drug candidates and/or combinatorial therapy approaches under *in vitro* conditions. Among others, the nicotinamide phosphoribosyltransferase (NAMPT) inhibitors daporinad and GMX-1778 greatly reduced the tumor burden of DBOs, suggesting strong cytotoxic capabilities. Strong tumor burden reductions together with pronounced antiproliferative effects on H3K27M cells were evident with the HDAC inhibitor romidepsin, the proteasome inhibitor delanzomib, the DRD2 antagonist ONC206 and the CDK inhibitors dinaciclib and zotiraciclib. An interesting model feature regarding the more therapy-resistant behavior of H3K27-altered DMGs in the clinic compared to preclinical testing, was observed in the DBOs with several drugs showing less pronounced tumor burden reduction than expected based on published sphere culture tests (Grasso et al., 2015; Lin et al., 2019). These drugs were found to primarily inhibit proliferation of H3K27M cells at the concentrations used. Drugs like the HDAC inhibitor panobinostat, the proteasome inhibitor marizomib as well as the HSP90 inhibitors AUY922 and HSP990 need to be mentioned here. This resistant tumor cell behavior in DBOs could help to improve the predictive power of *in vitro* drug tests by more closely reflecting a tumor-like cell response compared to sphere culture. In the following paragraphs, individual drug candidates and their effects on DBOs are discussed in more detail.

Two representatives of the NAMPT inhibitor class, daporinad and GMX1778, were found under the most potent drugs and greatly reduced the tumor burden of treated DBOs. Daporinad even showed the most potent effect across all tested drug candidates, with a reduction of tumor burden of 94 % at a concentration of only 10 nM. GMX1778 was less potent in comparison, demonstrating strong tumor burden reductions of 90 % at 100 nM. The NAMPT enzyme plays a key role in nicotinamide adenine dinucleotide (NAD+) recycling and NAMPT inhibition leads to depletion of intracellular NAD+. This results in a delayed cell death in cancer cells, that exhibit increased NAD+ consumption due to high metabolic rates, which might explain the strong effects on DBOs (Hasmann & Schemainda, 2003; Xie et al., 2020). Daporinad and GMX1778 were already proven for their potent preclinical anticancer activities in multiple entities, including glioblastoma cells (Barraud et al., 2016; Biniecka et al., 2023; Hjarnaa et al., 1999; Tateishi et al., 2015; P. Yang et al., 2015). Consistent with the DBO data presented, both drugs have also been identified in a large drug screen as potent agents against H3K27-altered DMG cells grown in cell culture with predicted blood-brain barrier permeability (Lin et al., 2019). However, in case of GMX1778, anticancer activity against solid tumors was not observed at same efficiency as seen in preclinical studies, which might also limit the drug`s translation into pDMG therapy (Biniecka et al., 2023; Heideman et al., 2009; Hovstadius et al., 2002). Based on the DBO data and the mentioned findings from other groups, daporinad, with its higher potency, has greater potential for clinical use and may be an interesting approach for pDMG treatment, but possible dose limiting toxicities must be considered here.

Also, the FDA approved HDAC inhibitor romidepsin showed one of the most potent reductions in tumor mass overall, together with a strong proliferation inhibition. A nanomolar potency of the inhibitor was also observed using biopsy-derived H3K27-altered DMG cultures (Vitanza et al., 2021), which further confirms the strong anti-tumor effect of the drug against this tumor entity *in vitro*. Until now, the potent effects of romidepsin are not present in HGG *in vivo* models and a phase I/II clinical trial using romidepsin against adult high-grade glioma showed no significant effects in patients (Iwamoto et al., 2011; Vitanza et al., 2021). One possible explanation for the lack of antitumor activity in the clinic may be a severely limited ability of the drug to overcome the BBB, which cannot be modeled in the presented DBO system. Results from *in vivo* experiments already indicated limitations in BBB permeability (Vitanza et al., 2021), which would certainly restrict the drug’s use in DMG therapy. However, strategies to improve BBB permeability, such as conjugation of the drug with BBB trafficking molecules or convection-enhanced delivery (CED), could help to exploit the potent antitumor effects in clinical use (Vitanza et al., 2021; Wang & Guo, 2015; Zhou et al., 2017). Surprisingly, less potent effects on DBO tumor burden compared to romidepsin were observable with panobinostat. 100 nM of the FDA approved HDAC inhibitor halved the tumor burden after 14-days of treatment. Stronger reductions would have been expected here, as studies with H3K27-altered DMG cells showed that cell viability decreased by more than 50 % with 100 nM panobinostat after only 72 hours (Grasso et al., 2015; Hennika et al., 2017; Lin et al., 2019). This may indicate a lower sensitivity of H3K27M cells in DBOs, which could be due to the realistic DMG subpopulation composition induced by DBO culture. The treatment data showed further that predominantly OPC- and OC-like cells were reduced, while the AC-like subpopulation was less affected. Nevertheless, one of the strongest proliferation inhibitions was induced by panobinostat, which could be the result of downregulated proliferation-associated genes, as observed in other studies (Grasso et al., 2015; Hennika et al., 2017). The capability to specifically reduce proliferating and potentially tumor initiating, undifferentiated OPC-like cells could be a very interesting feature of panobinostat, possibly leading to beneficial effects in the clinic. Second line treatments, which are capable to eliminate the remaining non proliferating and mostly AC-like differentiated tumor cells would be of special interest here to increase tumor cell reduction. When considering therapeutic regimens with higher concentrations of panobinostat to increase tumor shrinkage, the question is whether they can be used in children without causing intolerable toxicity. *In vivo* studies with daily panobinostat administration achieved concentrations higher than 500 nM in the mouse brain stem, but excessive toxicities made a dose de-escalation necessary. Unfortunately, well-tolerated concentrations of panobinostat did not prolong overall survival of mice, which could indicate that the use of higher panobinostat concentrations is limited (Hennika et al., 2017). Whether the reduced sensitivity of cancer cell fractions also occurs in patients and potentially affects treatment outcomes remains to be investigated but would fit the current picture that H3K27-altered DMGs generally respond poorly to many drug interventions in the clinic. The ability of panobinostat to reach DMG cells by crossing the BBB seems to be limited but existing (Aziz-Bose & Monje, 2019; Grasso et al., 2015). This makes the inhibitor an interesting drug candidate for the future treatment of H3K27-altered DMG patients and the results of current clinical trials can be eagerly awaited.

A compound that showed particularly strong effects on DBOs was the second-generation proteasome inhibitor delanzomib. Here, the overall strongest reduction of DBO tumor burden by 97 % was observed with 100 nM and proliferation rates were drastically reduced. The degradation of regulatory proteins by the proteasome is often deregulated in cancer (Kitagawa et al., 2009). Therefore, an upregulation of proteasome activity is a known mechanism in cancer cells to avoid cell death induced by the accumulation of defectively synthesized proteins (Rashid & Niklison-Chirou, 2019). The inhibition of proteasome activity by delanzomib might therefore greatly reduce this survival mechanism in H3K27M cells and explain the strong antitumor effects observed in DBOs. Consistent with the presented DBO data, delanzomib also demonstrated strong potency against several malignancies, including H3K27-altered DMG cells *in vitro* (Lin et al., 2019; Piva et al., 2008). This further supports delanzomib as an interesting candidate for the treatment of H3K27-altered DMGs. However, BBB permeability as well as potential limiting toxicities still need to be investigated. A different proteasome inhibitor which in the case of H3K27-altered DMGs has become more central in therapy research is marizomib. A high-throughput drug screening and xenograft studies identified marizomib as a potent agent and BBB penetrable properties were demonstrated *in vivo* (Di et al., 2016; Lin et al., 2019). A phase I clinical trial is currently running evaluating the combination of marizomib and panobinostat in H3K27-altered DMGs (Table1, NCT04341311). The presented DBO data showed that 100 nM of marizomib reduced tumor burden only about half after 14 days. This finding is surprising, since H3K27-altered sphere culture showed IC50 values around 17 nM post 72 hours incubation (Lin et al., 2019). Similar to panobinostat, this may suggest lower sensitivity of tumor cells in DBOs due to realistic subpopulation compositions induced by DBO culture. OC- and OPC-like cells were again affected more compared to AC-like cells, leading to increased AC-like proportions, which could be an interesting feature for drug combinations. Nevertheless, it remains to be clarified whether such lower sensitivities also occur in the clinic and affect treatment outcomes. Higher concentrations of marizomib could increase the overall antitumor effects, but information from the clinic regarding dose limiting toxicities are consequently important here.

The CDK inhibitors dinaciclib and zotiraciclib strongly inhibited proliferation of tumor cells at 1 µM with dinaciclib especially showing pronounced tumor reducing abilities in DBOs (tumor burden reduction of 95 %). CDKs are key regulators of cell cycle checkpoints and the inhibition of this protein class is already in clinical use for treating malignancies (Zhang et al., 2021). H3K27-alterd DMG samples revealed amplifications in cell cycle associated genes, including CDKs (Paugh et al., 2011), and clinical studies to investigate CDK-inhibition in this tumor entity were already initiated (Becher, 2019). Dinaciclib and zotiraciclib were tested by Lin et al., 2019 on H3K27M DMG cells and showed promising effects with dinaciclib being the more potent agent. These findings were also supported by the results of this work. The strong antiproliferative effects of dinaciclib and zotiraciclib can most likely be explained by the central role of CDKs in cell cycle control. Tumor cell composition analysis after zotiraciclib treatment showed a relatively equally distributed reduction of all subpopulations. This prevented the enrichment of one specific and less sensitive subpopulation, which could be beneficial for clinical use. However, it is important to mention that a concentration of 100 nM was used here, as 1 µM would have resulted in excessive tissue debris and insufficient cell numbers, consequently complicating the analysis. Therefore, changes of the observed subpopulation reduction pattern at other concentrations cannot be excluded. Overall, due to the tumor reducing and antiproliferative effects presented here, dinaciclib and zotiraciclib are interesting candidates for future clinical trials, with particular emphasis to dinaciclib due to its increased potency. Both drugs are theoretically able to cross the BBB (Lin et al., 2019), which increases their translational potential. However, this needs to be further validated and considered along with potential dose limiting toxicities regarding the therapeutical use in pediatric patients.

The DRD2 antagonist ONC206 led to drastic tumor burden reduction and an almost complete proliferation inhibition in the DBO model at 1 µM. Thereby, ONC206 exceeded the effects of its analogue ONC201 at the same concentration. In line with these findings, several preclinical studies also showed increased potency of ONC206 over ONC201 (El-Soussi et al., 2021; Ishida et al., 2018; Wagner et al., 2017). ONC201 already induced objective tumor responses in H3K27-altered DMGs during clinical use (Chi et al., 2019; Hall et al., 2019). Considering the similar structural and mechanistic properties of ONC206 and ONC201 (El-Soussi et al., 2021), it is likely that the enhanced antitumor capabilities of ONC206 will also be reflected in clinical application. ONC206 could therefore not only lead to greater tumor regression in the clinic compared to ONC201 but could eventually benefit the progression-free survival of patients. Furthermore, ONC206 showed a quite balanced reduction of all subpopulations in DBOs. It is important to note that a lower concentration of 100 nM was used as 1 µM of ONC206 would have complicated the analysis by low cell numbers and tissue debris. The more equally distributed reduction of subpopulations by ONC206 could counteract a possible selection of a more treatment-insensitive tumor subpopulation. However, it remains questionable whether higher concentrations of the drug would not increasingly affect specific subpopulations. This was observable in case of ONC201, were especially the OPC-like and OC-like cell populations were affected at 1 µM. This strong reduction of a possible tumor driving population within an *in vivo* achievable intratumoral drug concentration could explain the particularly strong and persistent response observed in individual patients with H3K27-altered DMGs (Arrillaga-Romany et al., 2020; Chi et al., 2019). Overall, the DBO data, together with the mentioned findings from other preclinical experiments and clinical trials, suggest that the DRD2 antagonists, and ONC206 in particular, have a strong translational potential and are therefore promising drug candidates for the treatment of H3K27-altered DMGs.

As mentioned earlier, paxalisib is a particularly interesting drug for the treatment of pDMGs due to its preclinical antitumor activity and BBB permeability. DBO treatments with paxalisib led to tumor burden reductions of around 60 %, but only when using a high concentration of 5 µM. Paxalisib has therefore been exceeded in potency by several compounds that demonstrated DBO tumor burden reductions of 80 % or greater at concentrations of 10 – 1000 nM (e.g. daporinad, delanzomib or ONC206). However, orthotopic glioblastoma xenograft mouse models showed, that the BBB permeability of paxalisib at tolerable doses is sufficient to reach concentrations around 5 µM in the brain, resulting in similar tumor reduction of around 70 % as seen in the treated DBOs (Salphati et al., 2016). Results from a phase II clinical trial with glioblastoma patients showed encouraging antitumor effects, further supporting the finding that the drug could reach clinically active concentrations in the brain (Wen et al., 2022). Combination therapies could be a way to increase antitumor effects of paxalisib. DBOs showed for example, that subpopulation reductions mainly affected the potentially tumor driving OPC-like subpopulation, shifting the cell composition more toward AC-like cells. Combination therapies of paxalisib with other drug candidates that enhance effects on paxalisib insensitive tumor cells could therefore further increase the tumor shrinkage. Recent preclinical and clinical data already showed promising effects by combining paxalisib with ONC201 in H3K27-altered DMGs (Jackson et al., 2023). Another dual inhibitor that was included in DBO treatments based on an increased interest from a clinical perspective is fimepinostat, with a phase I trial ongoing in H3K27-altered DMG patients (Table 1: NCT03893487). The PI3K/HDAC inhibitor already demonstrated potency against H3K27M-altered cells in concentrations below 20 nM *in vitro* after 72 hours (Lin et al., 2019; Pal et al., 2018). Interestingly, the strong effect of fimepinostat could not be found in the data shown here. Tumor burden was only halved after 14 days of treatment with 100 nM. The reduced tumor burden reduction potentially suggests a lower sensitivity of H3K27M cells in DBO culture, when considering the aforementioned nanomolar potencies after 72 hours. Therefore, higher concentrations of fimepinostat would certainly be needed here to increase antitumor effects, but it is questionable, if sufficient levels of the drug can be achieved in the brain, as the BBB permeability seems to be limited (Pal et al., 2018). Nevertheless, 100 nM fimepinostat reduced specifically OC- and OPC-like cells, which may be of interest for combination therapies that are more likely to target the less affected tumor cells. *In vivo* experiments showed that especially the combination of fimepinostat and irradiation significantly prolonged survival of H3K27-altered DMG xenograft mice (Pal et al., 2018), which further supports the potential benefit of combination therapy here.

HSP90 inhibitors substantially reduced proliferation of H3K27M DMG cells in DBOs. All used drug members of this inhibitor class were therefore found among the most potent antiproliferative agents. In particular, AUY922 and HSP990 demonstrated the highest antiproliferative potencies here with almost complete proliferation inhibition at 100 nM. The strong antiproliferative properties are potentially a result of cell cycle arrest, as observed in *in vitro* studies with several human cancer cell lines, including glioblastoma cells (Eccles et al., 2008; Wachsberger et al., 2014). The tumor burden reductions of DBOs were less pronounced than expected with HSP990, AUY922 and alvespimycin. High-throughput drug screens using H3K27M-DMG cells have identified the HSP90 inhibitors as being cytotoxic at significantly lower nanomolar concentrations (Grasso et al., 2015; Lin et al., 2019). In particular, AUY922 and HSP990 excelled here with IC50 values below 30 nM after a 72-hour treatment period. 31 % to 46 % of tumor cells were still present after two weeks of DBO treatments with 100 nM to 1000 nM of the drugs. The lower sensitivity of DMG cells to HSP90 inhibitors may indicate that the tumor-like cell composition in DBOs results in a different response to drugs than compared to conventional cell culture models. This finding further emphasizes the importance of more realistic models for drug testing, to potentially increase the translation of preclinical drug testing. Nevertheless, the strong anti-proliferative effect of HSP90 inhibition is of particular interest for rapidly growing tumors such as H3K27-altered DMGs and could have a positive impact on clinical outcomes. Combinations with other therapeutic agents to increase cytotoxicity would be conceivable. Especially AUY922 and HSP990 could be of value due to their potent effects at relative low concentrations, but clinical studies investigating the antitumor effectiveness of both drugs in brain tumor patients are lacking so far. In this context, HSP990 would be of particular interest, as it is assumed that the drug can cross the BBB, which remains questionable in the case of AUY922 (Babi et al., 2022; Lin et al., 2019).

4.3 Conclusion

The aim of this work was to develop a representative *in vitro* H3K27M model system for drug testing. This was achieved by co-culturing cerebral organoids with H3K27M DMG tumor spheres, resulting in the formation of DBOs. CODEX analysis revealed a tumor cell composition in DBOs that more closely reflects the situation found in primary tumor samples compared to common model systems. Subsequently, a treatment regimen was developed to characterize the effects of promising drug candidates from current research. As demonstrated by the presented treatment results, DBOs could be a useful tool for detailed analysis of individual therapeutic effects. The possibility to analyze treatment surviving cells potentially helps to identify new combinatorial therapies. Compared to published results from conventional cell culture based *in vitro* assays, H3K27M DMG cells in DBOs showed lower sensitivity to several drugs, which might be an intriguing model feature for therapy-resistant tumor behavior in the clinic. This could help to increase the predictive power of preclinical drug screens.

Bibliography

Allen, J. E., Krigsfeld, G., Mayes, P. A., Patel, L., Dicker, D. T., Patel, A. S., Dolloff, N. G., Messaris, E., Scata, K. A., Wang, W., Zhou, J. Y., Wu, G. S., & El-Deiry, W. S. (2013). Dual inactivation of Akt and ERK by TIC10 signals Foxo3a nuclear translocation, TRAIL gene induction, and potent antitumor effects. *Science Translational Medicine*, *5*(171). https://doi.org/10.1126/scitranslmed.3004828

Arrillaga-Romany, I., Odia, Y., Prabhu, V. V., Tarapore, R. S., Merdinger, K., Stogniew, M., Oster, W., Allen, J. E., Mehta, M., Batchelor, T. T., & Wen, P. Y. (2020). Biological activity of weekly ONC201 in adult recurrent glioblastoma patients. *Neuro-Oncology*, *22*(1), 94–102. https://doi.org/10.1093/NEUONC/NOZ164

Aziz-Bose, R., & Monje, M. (2019). Diffuse intrinsic pontine glioma: Molecular landscape and emerging therapeutic targets. *Current Opinion in Oncology*, *31*(6), 522–530. https://doi.org/10.1097/CCO.0000000000000577

Babi, A., Menlibayeva, K., Bex, T., Doskaliev, A., Akshulakov, S., & Shevtsov, M. (2022). Targeting Heat Shock Proteins in Malignant Brain Tumors: From Basic Research to Clinical Trials. *Cancers*, *14*(21). https://doi.org/10.3390/cancers14215435

Barraud, M., Garnier, J., Loncle, C., Gayet, O., Lequeue, C., Vasseur, S., Bian, B., Duconseil, P., Gilabert, M., Bigonnet, M., Maignan, A., Moutardier, V., Garcia, S., Turrini, O., Delpero, J.-R., Giovannini, M., Grandval, P., Gasmi, M., Ouaissi, M., … Dusetti, N. (2016). A pancreatic ductal adenocarcinoma subpopulation is sensitive to FK866, an inhibitor of NAMPT. *Oncotarget*, *7*(33), 53783–53796. www.impactjournals.com/oncotarget/

Becher, O. J. (2019). CDK4/6 and diffuse intrinsic pontine glioma - Evaluate at diagnosis? *EBioMedicine*, *44*, 16–17. https://doi.org/10.1016/j.ebiom.2019.04.043

Ben-David, U., Ha, G., Tseng, Y. Y., Greenwald, N. F., Oh, C., Shih, J., McFarland, J. M., Wong, B., Boehm, J. S., Beroukhim, R., & Golub, T. R. (2017). Patient-derived xenografts undergo mouse-specific tumor evolution. *Nature Genetics*, *49*(11), 1567–1575. https://doi.org/10.1038/ng.3967

Bender, S., Tang, Y., Lindroth, A. M., Hovestadt, V., Jones, D. T. W., Kool, M., Zapatka, M., Northcott, P. A., Sturm, D., Wang, W., Radlwimmer, B., Højfeldt, J. W., Truffaux, N., Castel, D., Schubert, S., Ryzhova, M., Şeker-Cin, H., Gronych, J., Johann, P. D., … Pfister, S. M. (2013). Reduced H3K27me3 and DNA Hypomethylation Are Major Drivers of Gene Expression in K27M Mutant Pediatric High-Grade Gliomas. *Cancer Cell*, *24*(5), 660–672. https://doi.org/10.1016/j.ccr.2013.10.006

Biniecka, P., Matsumoto, S., Belotti, A., Joussot, J., Bai, J. F., Majjigapu, S. R., Thoueille, P., Spaggiari, D., Desfontaine, V., Piacente, F., Bruzzone, S., Cea, M., Decosterd, L. A., Vogel, P., Nencioni, A., Duchosal, M. A., & Nahimana, A. (2023). Anticancer Activities of Novel Nicotinamide Phosphoribosyltransferase Inhibitors in Hematological Malignancies. *Molecules*, *28*(4). https://doi.org/10.3390/molecules28041897

BioSpace. (2022). *US FDA awards orphan drug designation (ODD) to paxalisib for AT/RT, a rare form of childhood brain cancer. Press release.* https://bit.ly/3A5VicX

Black, S., Phillips, D., Hickey, J. W., Kennedy-Darling, J., Venkataraaman, V. G., Samusik, N., Goltsev, Y., Schürch, C. M., & Nolan, G. P. (2021). CODEX multiplexed tissue imaging with DNA-conjugated antibodies. *Nature Protocols*, *16*(8), 3802–3835. https://doi.org/10.1038/s41596-021-00556-8

Broniscer, A., Laningham, F. H., Sanders, R. P., Kun, L. E., Ellison, D. W., & Gajjar, A. (2008). Young age may predict a better outcome for children with diffuse pontine glioma. *Cancer*, *113*(3), 566–572. https://doi.org/10.1002/cncr.23584

Buczkowicz, P., & Hawkins, C. (2015). Pathology, molecular genetics, and epigenetics of diffuse intrinsic pontine glioma. *Frontiers in Oncology*, *5*(147), 1–9. https://doi.org/10.3389/fonc.2015.00147

Buczkowicz, P., Hoeman, C., Rakopoulos, P., Pajovic, S., Letourneau, L., Dzamba, M., Morrison, A., Lewis, P., Bouffet, E., Bartels, U., Zuccaro, J., Agnihotri, S., Ryall, S., Barszczyk, M., Chornenkyy, Y., Bourgey, M., Bourque, G., Montpetit, A., Cordero, F., … Hawkins, C. (2014). Genomic analysis of diffuse intrinsic pontine gliomas identifies three molecular subgroups and recurrent activating ACVR1 mutations. *Nature Genetics*, *46*(5), 451–456. https://doi.org/10.1038/ng.2936

Caragher, S., Chalmers, A. J., & Gomez-Roman, N. (2019). Glioblastoma's next top model: Novel culture systems for brain cancer radiotherapy research. *Cancers*, *11*(1). https://doi.org/10.3390/cancers11010044

Chang, R., Tosi, U., Voronina, J., Adeuyan, O., Wu, L. Y., Schweitzer, M. E., Pisapia, D. J., Becher, O. J., Souweidane, M. M., & Maachani, U. B. (2019). Combined targeting of PI3K and MEK effector pathways via CED for DIPG therapy. *Neuro-Oncology Advances*, *1*(1). https://doi.org/10.1093/noajnl/vdz004

Chi, A. S., Tarapore, R. S., Hall, M. D., Shonka, N., Gardner, S., Umemura, Y., Sumrall, A., Khatib, Z., Mueller, S., Kline, C., Zaky, W., Khatua, S., Weathers, S. P., Odia, Y., Niazi, T. N., Daghistani, D., Cherrick, I., Korones, D., Karajannis, M. A., … Mehta, M. P. (2019). Pediatric and adult H3 K27M-mutant diffuse midline glioma treated with the selective DRD2 antagonist ONC201. *Journal of Neuro-Oncology*, *145*(1), 97–105. https://doi.org/10.1007/s11060-019-03271-3

Da Ros, M., De Gregorio, V., Iorio, A. L., Giunti, L., Guidi, M., de Martino, M., Genitori, L., & Sardi, I. (2018). Glioblastoma chemoresistance: the double play by microenvironment and blood-brain barrier. *International Journal of Molecular Sciences*, *19*(10). https://doi.org/10.3390/ijms19102879

da Silva, B., Mathew, R. K., Polson, E. S., Williams, J., & Wurdak, H. (2018). Spontaneous Glioblastoma Spheroid Infiltration of Early-Stage Cerebral Organoids Models Brain Tumor Invasion. *SLAS Discovery*, *23*(8), 862–868. https://doi.org/10.1177/2472555218764623

Dalle Ore, C., Coleman-Abadi, C., Gupta, N., & Mueller, S. (2023). Advances and Clinical Trials Update in the Treatment of Diffuse Intrinsic Pontine Gliomas. *Pediatric Neurosurgery*. https://doi.org/10.1159/000529099

Di, K., Lloyd, G. K., Abraham, V., Maclaren, A., Burrows, F. J., Desjardins, A., Trikha, M., & Bota, D. A. (2016). Marizomib activity as a single agent in malignant gliomas: Ability to cross the blood-brain barrier. *Neuro-Oncology*, *18*(6), 840–848. https://doi.org/10.1093/neuonc/nov299

Duchatel, R. J., Mannan, A., Woldu, A. S., Hawtrey, T., Hindley, P. A., Douglas, A. M., Jackson, E. R., Findlay, I. J., Germon, Z. P., Staudt, D., Kearney, P. S., Smith, N. D., Hindley, K. E., Cain, J. E., André, N., la Madrid, A. M., Nixon, B., de Iuliis, G. N., Nazarian, J., … Dun, M. D. (2021). Preclinical and clinical evaluation of German-sourced ONC201 for the treatment of H3K27M-mutant diffuse intrinsic pontine glioma. *Neuro-Oncology Advances*, *3*(1). https://doi.org/10.1093/noajnl/vdab169

Eccles, S. A., Massey, A., Raynaud, F. I., Sharp, S. Y., Box, G., Valenti, M., Patterson, L., Brandon, A. D. H., Gowan, S., Boxall, F., Aherne, W., Rowlands, M., Hayes, A., Martins, V., Urban, F., Boxall, K., Prodromou, C., Pearl, L., James, K., … Workman, P. (2008). NVP-AUY922: A novel heat shock protein 90 inhibitor active against xenograft tumor growth, angiogenesis, and metastasis. *Cancer Research*, *68*(8), 2850–2860. https://doi.org/10.1158/0008-5472.CAN-07-5256

Einhaus, J., Rochwarger, A., Mattern, S., Gaudillière, B., & Schürch, C. M. (2023). High-multiplex tissue imaging in routine pathology—are we there yet? *Virchows Archiv*. https://doi.org/10.1007/s00428-023-03509-6

El-Khouly, F. E., Veldhuijzen van Zanten, S. E. M., Santa-Maria Lopez, V., Hendrikse, N. H., Kaspers, G. J. L., Loizos, G., Sumerauer, D., Nysom, K., Pruunsild, K., Pentikainen, V., Thorarinsdottir, H. K., Rutkauskiene, G., Calvagna, V., Drogosiewicz, M., Dragomir, M., Deak, L., Kitanovski, L., von Bueren, A. O., Kebudi, R., … van Vuurden, D. G. (2019). Diagnostics and treatment of diffuse intrinsic pontine glioma: where do we stand? *Journal of Neuro-Oncology*, *145*(1), 177–184. https://doi.org/10.1007/s11060-019-03287-9

El-Soussi, S., Hanna, R., Semaan, H., Khater, A.-R., Abdallah, J., Abou-Kheir, W., & Abou-Antoun, T. (2021). A Novel Therapeutic Mechanism of Imipridones ONC201/ONC206 in MYCN-Amplified Neuroblastoma Cells via Differential Expression of Tumorigenic Proteins. *Frontiers in Pediatrics*, *9*(693145). https://doi.org/10.3389/fped.2021.693145

Ferreira, D., Adega, F., & Chaves, R. (2013). The Importance of Cancer Cell Lines as in vitro Models in Cancer Methylome Analysis and Anticancer Drugs Testing. In *Oncogenomics and Cancer Proteomics - Novel Approaches in Biomarkers Discovery and Therapeutic Targets in Cancer*. InTech. https://doi.org/10.5772/53110

Filbin, M. G., Tirosh, I., Hovestadt, V., Shaw, M. L., Escalante, L. E., Mathewson, N. D., Neftel, C., Frank, N., Pelton, K., Hebert, C. M., Haberler, C., Yizhak, K., Gojo, J., Egervari, K., Mount, C., Van Galen, P., Bonal, D. M., Nguyen, Q. De, Beck, A., … Suvà, M. L. (2018). Developmental and oncogenic programs in H3K27M gliomas dissected by single-cell RNA-seq. *Science*, *360*(6386), 331–335. https://doi.org/10.1126/science.aao4750

Fontebasso, A. M., Papillon-Cavanagh, S., Schwartzentruber, J., Nikbakht, H., Gerges, N., Fiset, P. O., Bechet, D., Faury, D., de Jay, N., Ramkissoon, L. A., Corcoran, A., Jones, D. T. W., Sturm, D., Johann, P., Tomita, T., Goldman, S., Nagib, M., Bendel, A., Goumnerova, L., … Kieran, M. W. (2014). Recurrent somatic mutations in ACVR1 in pediatric midline high-grade astrocytoma. *Nature Genetics*, *46*(5), 462–466. https://doi.org/10.1038/ng.2950

Funato, K., Major, T., Lewis, P. W., Allis, C. D., & Tabar, V. (2014). Use of human embryonic stem cells to model pediatric gliomas with H3.3K27M histone mutation. *Science*, *346*(6216), 1529–1533. https://doi.org/10.1126/science.1253799

Gallitto, M., Lazarev, S., Wasserman, I., Stafford, J. M., Wolden, S. L., Terezakis, S. A., Bindra, R. S., & Bakst, R. L. (2019). Role of Radiation Therapy in the Management of Diffuse Intrinsic Pontine Glioma: A Systematic Review. *Advances in Radiation Oncology*, *4*(3), 520–531. https://doi.org/10.1016/j.adro.2019.03.009

Granada, A. E., Jiménez, A., Stewart-Ornstein, J., Blüthgena, N., Reber, S., Jambhekar, A., & Lahav, G. (2020). The effects of proliferation status and cell cycle phase on the responses of single cells to chemotherapy. *Molecular Biology of the Cell*, *31*(8), 845–857. https://doi.org/10.1091/mbc.E19-09-0515

Grasso, C. S., Tang, Y., Truffaux, N., Berlow, N. E., Liu, L., Debily, M. A., Quist, M. J., Davis, L. E., Huang, E. C., Woo, P. J., Ponnuswami, A., Chen, S., Johung, T. B., Sun, W., Kogiso, M., Du, Y., Qi, L., Huang, Y., Hütt-Cabezas, M., … Monje, M. (2015). Functionally defined therapeutic targets in diffuse intrinsic pontine glioma. *Nature Medicine*, *21*(6), 555–559. https://doi.org/10.1038/nm.3855

Hall, M. D., Odia, Y., Allen, J. E., Tarapore, R., Khatib, Z., Niazi, T. N., Daghistani, D., Schalop, L., Chi, A. S., Oster, W., & Mehta, M. P. (2019). First clinical experience with DRD2/3 antagonist ONC201 in H3 K27M–mutant pediatric diffuse intrinsic pontine glioma: A case report. *Journal of Neurosurgery: Pediatrics*, *23*(6), 719–725. https://doi.org/10.3171/2019.2.PEDS18480

Harutyunyan, A. S., Krug, B., Chen, H., Papillon-Cavanagh, S., Zeinieh, M., de Jay, N., Deshmukh, S., Chen, C. C. L., Belle, J., Mikael, L. G., Marchione, D. M., Li, R., Nikbakht, H., Hu, B., Cagnone, G., Cheung, W. A., Mohammadnia, A., Bechet, D., Faury, D., … Majewski, J. (2019). H3K27M induces defective chromatin spread of PRC2-mediated repressive H3K27me2/me3 and is essential for glioma tumorigenesis. *Nature Communications*, *10*(1). https://doi.org/10.1038/s41467-019-09140-x

Hasmann, M., & Schemainda, I. (2003). FK866, a Highly Specific Noncompetitive Inhibitor of Nicotinamide Phosphoribosyltransferase, Represents a Novel Mechanism for Induction of Tumor Cell Apoptosis. *Cancer Research*, *63*, 7436–7442. https://www.researchgate.net/publication/6858299

Heffron, T. P., Ndubaku, C. O., Salphati, L., Alicke, B., Cheong, J., Drobnick, J., Edgar, K., Gould, S. E., Lee, L. B., Lesnick, J. D., Lewis, C., Nonomiya, J., Pang, J., Plise, E. G., Sideris, S., Wallin, J., Wang, L., Zhang, X., & Olivero, A. G. (2016). Discovery of Clinical Development Candidate GDC-0084, a Brain Penetrant Inhibitor of PI3K and mTOR. *ACS Medicinal Chemistry Letters*, *7*(4), 351–356. https://doi.org/10.1021/acsmedchemlett.6b00005

Heideman, A., Berglund, Å., Larsson, R., & Nygren, P. (2009). Safety and efficacy of NAD depleting cancer drugs: results of a phase I clinical trial of CHS 828 and overview of published data. *Chemotherapy and Pharmacology*, *65*(6). https://doi.org/10.1007/s00280-009-1125-3ï

Hennika, T., Hu, G., Olaciregui, N. G., Barton, K. L., Ehteda, A., Chitranjan, A., Chang, C., Gifford, A. J., Tsoli, M., Ziegler, D. S., Carcaboso, A. M., & Becher, O. J. (2017). Pre-clinical study of panobinostat in xenograft and genetically engineered murine diffuse intrinsic pontine glioma models. *PLoS ONE*, *12*(1). https://doi.org/10.1371/journal.pone.0169485

Hjarnaa, P.-J. V., Jonsson, E., Latini, S., Dhar, S., Larsson, R., Bramm, E., Skov, T., & Binderup, L. (1999). CHS 828, a Novel Pyridyl Cyanoguanidine with Potent Antitumor Activity in Vitro and in Vivo. *Cancer Research*, *59*, 5751–5757.http://aacrjournals.org/cancerres/article pdf/59/22/5751/2472888/5751.pdf

Hoffman, L. M., van Zanten, S. E. M. V., Colditz, N., Baugh, J., Chaney, B., Hoffmann, M., Lane, A., Fuller, C., Miles, L., Hawkins, C., Bartels, U., Bouffet, E., Goldman, S., Leary, S., Foreman, N. K., Packer, R., Warren, K. E., Broniscer, A., Kieran, M. W., … Fouladi, M. (2018). Clinical, radiologic, pathologic, and molecular characteristics of long-term survivors of Diffuse Intrinsic Pontine Glioma (DIPG): A collaborative report from the International and European Society for Pediatric Oncology DIPG registries. *Journal of Clinical Oncology*, *36*(19), 1963–1972. https://doi.org/10.1200/JCO.2017.75.9308

Hovstadius, P., Larsson, R., Jonsson, E., Skov, T., Kissmeyer, A.-M., Krasilnikoff, K., Bergh, J., Karlsson, M. O., Lönnebo, A., Ahlgren, J., & Biosciences, P. (2002). A Phase I Study of CHS 828 in Patients with Solid Tumor Malignancy 1. *Clinical Cancer Research*, *8*, 2843–2850. http://aacrjournals.org/clincancerres/article-pdf/8/9/2843/2083569/df0902002843.pdf

Hubert, C. G., Rivera, M., Spangler, L. C., Wu, Q., Mack, S. C., Prager, B. C., Couce, M., McLendon, R. E., Sloan, A. E., & Rich, J. N. (2016). A three-dimensional organoid culture system derived from human glioblastomas recapitulates the hypoxic gradients and cancer stem cell heterogeneity of tumors found in vivo. *Cancer Research*, *76*(8), 2465–2477. https://doi.org/10.1158/0008-5472.CAN-15-2402

International Agency for Research on Cancer. (2020). *GLOBOCAN 2020*. https://gco.iarc.fr/

Ishida, C. T., Zhang, Y., Bianchetti, E., Shu, C., Nguyen, T. T. T., Kleiner, G., Sanchez-Quintero, M. J., Quinzii, C. M., Westhoff, M. A., Karpel-Massler, G., Prabhu, V. V., Allen, J. E., & Siegelin, M. D. (2018). Metabolic reprogramming by dual AKT/ERK inhibition through imipridones elicits unique vulnerabilities in glioblastoma. *Clinical Cancer Research*, *24*(21), 5392–5406. https://doi.org/10.1158/1078-0432.CCR-18-1040

Iwamoto, F. M., Lamborn, K. R., Kuhn, J. G., Wen, P. Y., Alfred Yung, W. K., Gilbert, M. R., Chang, S. M., Lieberman, F. S., Prados, M. D., & Fine, H. A. (2011). A phase I/II trial of the histone deacetylase inhibitor romidepsin for adults with recurrent malignant glioma: North American brain tumor consortium study 03-03. *Neuro-Oncology*, *13*(5), 509–516. https://doi.org/10.1093/neuonc/nor017

Jackson, E. R., Duchatel, R. J., Staudt, D. E., Persson, M. L., Mannan, A., Yadavilli, S., Parackal, S., Game, S., Chong, W. C., Jayasekara, W. S. N., Grand, M. Le, Kearney, P. S., Douglas, A. M., Findlay, I. J., Germon, Z. P., McEwen, H. P., Beitaki, T. S., Patabendige, A., Skerrett-Byrne, D. A., … Dun, M. D. (2023). ONC201 in Combination with Paxalisib for the Treatment of H3K27-Altered Diffuse Midline Glioma. *Cancer Research*, OF1–OF17. https://doi.org/10.1158/0008-5472.CAN-23-0186

Jansen, M. H., van Zanten, S. E. V., Aliaga, E. S., Heymans, M. W., Warmuth-Metz, M., Hargrave, D., van der Hoeven, E. J., Gidding, C. E., de Bont, E. S., Eshghi, O. S., Reddingius, R., Peeters, C. M., Schouten-Van Meeteren, A. Y. N., Gooskens, R. H. J., Granzen, B., Paardekooper, G. M., Janssens, G. O., Noske, D. P., Barkhof, F., … van Vuurden, D. G. (2015). Survival prediction model of children with diffuse intrinsic pontine glioma based on clinical and radiological criteria. *Neuro-Oncology*, *17*(1), 160–166. https://doi.org/10.1093/neuonc/nou104

Janssens, G. O. R. J., Gidding, C. E. M., van Lindert, E. J., Oldenburger, F. R., Erasmus, C. E., Schouten-Meeteren, A. Y. N., & Kaanders, J. H. A. M. (2009). The Role of Hypofractionation Radiotherapy for Diffuse Intrinsic Brainstem Glioma in Children: A Pilot Study. *International Journal of Radiation Oncology Biology Physics*, *73*(3), 722–726. https://doi.org/10.1016/j.ijrobp.2008.05.030

Joseph, J. v., Blaavand, M. S., Daubon, T., Kruyt, F. A., & Thomsen, M. K. (2021). Three-dimensional culture models to study glioblastoma — current trends and future perspectives. *Current Opinion in Pharmacology*, *61*, 91–97. https://doi.org/10.1016/j.coph.2021.08.019

Katsuta, E., Rashid, O. M., & Takabe, K. (2020). Clinical relevance of tumor microenvironment: immune cells, vessels, and mouse models. *Human Cell*, *33*(4), 930–937. https://doi.org/10.1007/s13577-020-00380-4

Khuong-Quang, D. A., Buczkowicz, P., Rakopoulos, P., Liu, X. Y., Fontebasso, A. M., Bouffet, E., Bartels, U., Albrecht, S., Schwartzentruber, J., Letourneau, L., Bourgey, M., Bourque, G., Montpetit, A., Bourret, G., Lepage, P., Fleming, A., Lichter, P., Kool, M., von Deimling, A., … Hawkins, C. (2012). K27M mutation in histone H3.3 defines clinically and biologically distinct subgroups of pediatric diffuse intrinsic pontine gliomas. *Acta Neuropathologica*, *124*(3), 439–447. https://doi.org/10.1007/s00401-012-0998-0

Kitagawa, K., Kotake, Y., & Kitagawa, M. (2009). Ubiquitin-mediated control of oncogene and tumor suppressor gene products. *Cancer Science*, *100*(8), 1374–1381. https://doi.org/10.1111/j.1349-7006.2009.01196.x

Kluiver, T. A., Alieva, M., van Vuurden, D. G., Wehrens, E. J., & Rios, A. C. (2020). Invaders Exposed: Understanding and Targeting Tumor Cell Invasion in Diffuse Intrinsic Pontine Glioma. *Frontiers in Oncology*, *10*(92), 1–13. https://doi.org/10.3389/fonc.2020.00092

Kyu, H. H., Stein, C. E., Boschi Pinto, C., Rakovac, I., Weber, M. W., Dannemann Purnat, T., Amuah, J. E., Glenn, S. D., Cercy, K., Biryukov, S., Gold, A. L., Chew, A., Mooney, M. D., O'Rourke, K. F., Sligar, A., Murray, C. J. L., Mokdad, A. H., & Naghavi, M. (2018). Causes of death among children aged 5–14 years in the WHO European Region: a systematic analysis for the Global Burden of Disease Study 2016. *The Lancet Child and Adolescent Health*, *2*(5), 321–337. https://doi.org/10.1016/S2352-4642(18)30095-6

Lancaster, M. A., & Knoblich, J. A. (2014). Generation of cerebral organoids from human pluripotent stem cells. *Nature Protocols*, *9*(10), 2329–2340. https://doi.org/10.1038/nprot.2014.158

Lancaster, M. A., Renner, M., Martin, C. A., Wenzel, D., Bicknell, L. S., Hurles, M. E., Homfray, T., Penninger, J. M., Jackson, A. P., & Knoblich, J. A. (2013). Cerebral organoids model human brain development and microcephaly. *Nature*, *501*(7467), 373–379. https://doi.org/10.1038/nature12517

Langhans, S. A. (2018). Three-Dimensional in vitro cell culture models in drug discovery and drug repositioning. *Frontiers in Pharmacology*, *9*(6). https://doi.org/10.3389/fphar.2018.00006

Leszczynska, K. B., Jayaprakash, C., Kaminska, B., & Mieczkowski, J. (2021). Emerging Advances in Combinatorial Treatments of Epigenetically Altered Pediatric High-Grade H3K27M Gliomas. *Frontiers in Genetics*, *12*(742561), 1–11. https://doi.org/10.3389/fgene.2021.742561

Lewis, P. W., Müller, M. M., Koletsky, M. S., Cordero, F., Lin, S., Banaszynski, L. A., Garcia, B. A., Muir, T. W., Becher, O. J., & Allis, C. D. (2013). Inhibition of PRC2 activity by a gain-of-function H3 mutation found in pediatric glioblastoma. *Science*, *340*(6134), 857–861. https://doi.org/10.1126/science.1232245

Li, G., Tian, Y., & Zhu, W. G. (2020). The Roles of Histone Deacetylases and Their Inhibitors in Cancer Therapy. *Frontiers in Cell and Developmental Biology*, *8*(576946). https://doi.org/10.3389/fcell.2020.576946

Li, J., Zhu, S., Kozono, D., Ng, K., Futalan, D., Shen, Y., Akers, J. C., Steed, T., Kushwaha, D., Schlabach, M., Carter, B. S., Kwon, C.-H., Furnari, F., Cavenee, W., Elledge, S., & Chen, C. C. (2014). Genome-wide shRNA screen revealed integrated mitogenic signaling between dopamine receptor D2 (DRD2) and epidermal growth factor receptor (EGFR) in glioblastoma. *Oncotarget*, *5*(4), 882–893. www.impactjournals.com/oncotarget

Li, Z., & Langhans, S. A. (2021). In Vivo and Ex Vivo Pediatric Brain Tumor Models: An Overview. *Frontiers in Oncology*, *11*. https://doi.org/10.3389/fonc.2021.620831

Lin, G. L., & Monje, M. (2017). A protocol for rapid post-mortem cell culture of diffuse intrinsic pontine glioma (DIPG). *Journal of Visualized Experiments*, *2017*(121). https://doi.org/10.3791/55360

Lin, G. L., Wilson, K. M., Ceribelli, M., Stanton, B. Z., Woo, P. J., Kreimer, S., Qin, E. Y., Zhang, X., Lennon, J., Nagaraja, S., Morris, P. J., Quezada, M., Gillespie, S. M., Duveau, D. Y., Michalowski, A. M., Shinn, P., Guha, R., Ferrer, M., Klumpp-Thomas, C., … Monje, M. (2019). Therapeutic strategies for diffuse midline glioma from high-throughput combination drug screening. *Science Translational Medicine*, *11*(519). https://doi.org/10.1126/scitranslmed.aaw0064

Linkous, A., Balamatsias, D., Snuderl, M., Edwards, L., Miyaguchi, K., Milner, T., Reich, B., Cohen-Gould, L., Storaska, A., Nakayama, Y., Schenkein, E., Singhania, R., Cirigliano, S., Magdeldin, T., Lin, Y., Nanjangud, G., Chadalavada, K., Pisapia, D., Liston, C., & Fine, H. A. (2019). Modeling Patient-Derived Glioblastoma with Cerebral Organoids. *Cell Reports*, *26*(12), 3203-3211.e5. https://doi.org/10.1016/j.celrep.2019.02.063

Liu, I., Jiang, L., Samuelsson, E. R., Marco Salas, S., Beck, A., Hack, O. A., Jeong, D., Shaw, M. L., Englinger, B., LaBelle, J., Mire, H. M., Madlener, S., Mayr, L., Quezada, M. A., Trissal, M., Panditharatna, E., Ernst, K. J., Vogelzang, J., Gatesman, T. A., … Filbin, M. G. (2022). The landscape of tumor cell states and spatial organization in H3-K27M mutant diffuse midline glioma across age and location. *Nature Genetics*, *54*(12), 1881–1894. https://doi.org/10.1038/s41588-022-01236-3

Louis, D. N., Perry, A., Wesseling, P., Brat, D. J., Cree, I. A., Figarella-Branger, D., Hawkins, C., Ng, H. K., Pfister, S. M., Reifenberger, G., Soffietti, R., Von Deimling, A., & Ellison, D. W. (2021). The 2021 WHO classification of tumors of the central nervous system: A summary. *Neuro-Oncology*, *23*(8), 1231–1251. https://doi.org/10.1093/neuonc/noab106

McGranahan, N., & Swanton, C. (2017). Clonal Heterogeneity and Tumor Evolution: Past, Present, and the Future. *Cell*, *168*(4), 613–628. https://doi.org/10.1016/j.cell.2017.01.018

Mirabelli, P., Coppola, L., & Salvatore, M. (2019). Cancer cell lines are useful model systems for medical research. *Cancers*, *11*(8). https://doi.org/10.3390/cancers11081098

Monje, M., Mitra, S. S., Freret, M. E., Raveh, T. B., Kim, J., Masek, M., Attema, J. L., Li, G., Haddix, T., Edwards, M. S. B., Fisher, P. G., Weissman, I. L., Rowitch, D. H., Vogel, H., Wong, A. J., & Beachy, P. A. (2011). Hedgehog-responsive candidate cell of origin for diffuse intrinsic pontine glioma. *Proceedings of the National Academy of Sciences of the United States of America*, *108*(11), 4453–4458. https://doi.org/10.1073/pnas.1101657108

Nicholson, J. G., & Fine, H. A. (2021). Diffuse glioma heterogeneity and its therapeutic implications. *Cancer Discovery*, *11*(3), 575–590. https://doi.org/10.1158/2159-8290.CD-20-1474

Nikbakht, H., Panditharatna, E., Mikael, L. G., Li, R., Gayden, T., Osmond, M., Ho, C. Y., Kambhampati, M., Hwang, E. I., Faury, D., Siu, A., Papillon-Cavanagh, S., Bechet, D., Ligon, K. L., Ellezam, B., Ingram, W. J., Stinson, C., Moore, A. S., Warren, K. E., … Nazarian, J. (2016). Spatial and temporal homogeneity of driver mutations in diffuse intrinsic pontine glioma. *Nature Communications*, *7*. https://doi.org/10.1038/ncomms11185

Pal, S., Kozono, D., Yang, X., Fendler, W., Fitts, W., Ni, J., Alberta, J. A., Zhao, J., Liu, K. X., Bian, J., Truffaux, N., Weiss, W. A., Resnick, A. C., Bandopadhayay, P., Ligon, K. L., DuBois, S. G., Mueller, S., Chowdhury, D., & Haas-Kogan, D. A. (2018). Dual HDAC and PI3K inhibition abrogates NFkB- and FOXM1-mediated DNA damage response to radiosensitize pediatric high-grade gliomas. *Cancer Research*, *78*(14), 4007–4021. https://doi.org/10.1158/0008-5472.CAN-17-3691

Patil, N., Kelly, M. E., Yeboa, D. N., Buerki, R. A., Cioffi, G., Balaji, S., Ostrom, Q. T., Kruchko, C., & Barnholtz-Sloan, J. S. (2021). Epidemiology of brainstem high-grade gliomas in children and adolescents in the United States, 2000-2017. *Neuro-Oncology*, *23*(6), 990–998. https://doi.org/10.1093/neuonc/noaa295

Paugh, B. S., Broniscer, A., Qu, C., Miller, C. P., Zhang, J., Tatevossian, R. G., Olson, J. M., Geyer, J. R., Chi, S. N., Da Silva, N. S., Onar-Thomas, A., Baker, J. N., Gajjar, A., Ellison, D. W., & Baker, S. J. (2011). Genome-wide analyses identify recurrent amplifications of receptor tyrosine kinases and cell-cycle regulatory genes in diffuse intrinsic pontine glioma. *Journal of Clinical Oncology*, *29*(30), 3999–4006. https://doi.org/10.1200/JCO.2011.35.5677

Paugh, B. S., Zhu, X., Qu, C., Endersby, R., Diaz, A. K., Zhang, J., Bax, D. A., Carvalho, D., Reis, R. M., Onar-Thomas, A., Broniscer, A., Wetmore, C., Zhang, J., Jones, C., Ellison, D. W., & Baker, S. J. (2013). Novel oncogenic PDGFRA mutations in pediatric high-grade gliomas. *Cancer Research*, *73*(20), 6219–6229. https://doi.org/10.1158/0008-5472.CAN-13-1491

Pine, A. R., Cirigliano, S. M., Nicholson, J. G., Hu, Y., Linkous, A., Miyaguchi, K., Edwards, L., Singhania, R., Schwartz, T. H., Ramakrishna, R., Pisapia, D. J., Snuderl, M., Elemento, O., & Fine, H. A. (2020). Tumor microenvironment is critical for the maintenance of cellular states found in primary glioblastomas. *Cancer Discovery*, *10*(7), 964–979. https://doi.org/10.1158/2159-8290.CD-20-0057

Piunti, A., Hashizume, R., Morgan, M. A., Bartom, E. T., Horbinski, C. M., Marshall, S. A., Rendleman, E. J., Ma, Q., Takahashi, Y. H., Woodfin, A. R., Misharin, A. v., Abshiru, N. A., Lulla, R. R., Saratsis, A. M., Kelleher, N. L., James, C. D., & Shilatifard, A. (2017). Therapeutic targeting of polycomb and BET bromodomain proteins in diffuse intrinsic pontine gliomas. *Nature Medicine*, *23*(4), 493–500. https://doi.org/10.1038/nm.4296

Piva, R., Ruggeri, B., Williams, M., Costa, G., Tamagno, M., Ferrero, D., Giai, V., Coscia, M., Peola, S., Massaia, M., Pezzoni, G., Allievi, C., Pescalli, N., Cassin, M., Giovine, S. Di, Nicoli, P., De Feudis, P., Strepponi, I., Roato, M., … Inghirami, G. (2008). CEP-18770: A novel, orally active proteasome inhibitor with a tumor-selective pharmacologic profile competitive with bortezomib. *Blood*, *111*(5), 2765–2775. https://doi.org/10.1182/blood-2007-07-100651

Qiu, G. Z., Jin, M. Z., Dai, J. X., Sun, W., Feng, J. H., & Jin, W. L. (2017). Reprogramming of the Tumor in the Hypoxic Niche: The Emerging Concept and Associated Therapeutic Strategies. *Trends in Pharmacological Sciences*, *38*(8), 669–686. https://doi.org/10.1016/j.tips.2017.05.002

Rashid, F., & Niklison-Chirou, M. V. (2019). Proteasome inhibition—a new target for brain tumours. *Cell Death Discovery*, *5*(1). https://doi.org/10.1038/s41420-019-0227-x

Riedel, N. C., de Faria, F. W., Alfert, A., Bruder, J. M., & Kerl, K. (2022). Three-Dimensional Cell Culture Systems in Pediatric and Adult Brain Tumor Precision Medicine. *Cancers*, *14*(23). https://doi.org/10.3390/cancers14235972

Salphati, L., Alicke, B., Heffron, T. P., Shahidi-Latham, S., Nishimura, M., Cao, T., Carano, R. A., Cheong, J., Greve, J., Koeppen, H., Lau, S., Lee, L. B., Nannini-Pepe, M., Pang, J., Plise, E. G., Quiason, C., Rangell, L., Zhang, X., Gould, S. E., … Olivero, A. G. (2016). Brain distribution and efficacy of the brain penetrant PI3K inhibitor GDC-0084 in orthotopic mouse models of human glioblastoma. *Drug Metabolism and Disposition*, *44*(12), 1881–1889. https://doi.org/10.1124/dmd.116.071423

Schwartzentruber, J., Korshunov, A., Liu, X. Y., Jones, D. T. W., Pfaff, E., Jacob, K., Sturm, D., Fontebasso, A. M., Quang, D. A. K., Tönjes, M., Hovestadt, V., Albrecht, S., Kool, M., Nantel, A., Konermann, C., Lindroth, A., Jäger, N., Rausch, T., Ryzhova, M., … Jabado, N. (2012). Driver mutations in histone H3.3 and chromatin remodelling genes in paediatric glioblastoma. *Nature*, *482*(7384), 226–231. https://doi.org/10.1038/nature10833

Singh, V. K., & Seed, T. M. (2021). How necessary are animal models for modern drug discovery? *Expert Opinion on Drug Discovery*, *16*(12), 1391–1397. https://doi.org/10.1080/17460441.2021.1972255

Sturm, D., Bender, S., Jones, D. T. W., Lichter, P., Grill, J., Becher, O., Hawkins, C., Majewski, J., Jones, C., Costello, J. F., Iavarone, A., Aldape, K., Brennan, C. W., Jabado, N., & Pfister, S. M. (2014). Paediatric and adult glioblastoma: Multiform (epi)genomic culprits emerge. *Nature Reviews Cancer*, *14*(2), 92–107. https://doi.org/10.1038/nrc3655

Sturm, D., Pfister, S. M., & Jones, D. T. W. (2017). Pediatric Gliomas: Current Concepts on Diagnosis, Biology, and Clinical Management. *Journal of Clinical Oncology*, *35*(21), 2370–2377. https://doi.org/10.1200/JCO.2017

Sun, H., Cao, S., Mashl, R. J., Mo, C. K., Zaccaria, S., Wendl, M. C., Davies, S. R., Bailey, M. H., Primeau, T. M., Hoog, J., Mudd, J. L., Dean, D. A., Patidar, R., Chen, L., Wyczalkowski, M. A., Jayasinghe, R. G., Rodrigues, F. M., Terekhanova, N. v., Li, Y., … Ding, L. (2021). Comprehensive characterization of 536 patient-derived xenograft models prioritizes candidatesfor targeted treatment. *Nature Communications*, *12*(1). https://doi.org/10.1038/s41467-021-25177-3

’t Hart, E., Bianco, J., Besse, H. C., Chin Joe Kie, L. A., Cornet, L., Eikelenboom, K. L., van den Broek, T. J. M., Derieppe, M., Su, Y., Hoving, E. W., Ries, M. G., & van Vuurden, D. G. (2023). Towards Standardisation of a Diffuse Midline Glioma Patient-Derived Xenograft Mouse Model Based on Suspension Matrices for Preclinical Research. *Biomedicines*, *11*(2). https://doi.org/10.3390/biomedicines11020527

Tang, X., Huang, Y., Lei, J., Luo, H., & Zhu, X. (2019). The single-cell sequencing: New developments and medical applications. *Cell and Bioscience*, *9*(1). https://doi.org/10.1186/s13578-019-0314-y

Tateishi, K., Wakimoto, H., Iafrate, A. J., Tanaka, S., Loebel, F., Lelic, N., Wiederschain, D., Bedel, O., Deng, G., Zhang, B., He, T., Shi, X., Gerszten, R. E., Zhang, Y., Yeh, J. R. J., Curry, W. T., Zhao, D., Sundaram, S., Nigim, F., … Cahill, D. P. (2015). Extreme Vulnerability of IDH1 Mutant Cancers to NAD+ Depletion. *Cancer Cell*, *28*(6), 773–784. https://doi.org/10.1016/j.ccell.2015.11.006

Taylor, K. R., Mackay, A., Truffaux, N., Butterfield, Y. S., Morozova, O., Philippe, C., Castel, D., Grasso, C. S., Vinci, M., Carvalho, D., Carcaboso, A. M., de Torres, C., Cruz, O., Mora, J., Entz-Werle, N., Ingram, W. J., Monje, M., Hargrave, D., Bullock, A. N., … Grill, J. (2014). Recurrent activating ACVR1 mutations in diffuse intrinsic pontine glioma. *Nature Genetics*, *46*(5), 457–461. https://doi.org/10.1038/ng.2925

Tsoli, M., Shen, H., Mayoh, C., Franshaw, L., Ehteda, A., Upton, D., Carvalho, D., Vinci, M., Meel, M. H., van Vuurden, D., Plessier, A., Castel, D., Drissi, R., Farrell, M., Cryan, J., Crimmins, D., Caird, J., Pears, J., Francis, S., … Ziegler, D. S. (2019). International experience in the development of patient-derived xenograft models of diffuse intrinsic pontine glioma. *Journal of Neuro-Oncology*, *141*(2), 253–263. https://doi.org/10.1007/s11060-018-03038-2

Ueoka, D. I., Nogueira, J., Campos, J. C., Filho, P. M., Ferman, S., & Lima, M. A. (2009). Brainstem gliomas- Retrospective analysis of 86 patients. *Journal of the Neurological Sciences*, *281*(1–2), 20–23. https://doi.org/10.1016/j.jns.2009.03.009

Venkatesh, H. S., Johung, T. B., Caretti, V., Noll, A., Tang, Y., Nagaraja, S., Gibson, E. M., Mount, C. W., Polepalli, J., Mitra, S. S., Woo, P. J., Malenka, R. C., Vogel, H., Bredel, M., Mallick, P., & Monje, M. (2015). Neuronal activity promotes glioma growth through neuroligin-3 secretion. *Cell*, *161*(4), 803–816. https://doi.org/10.1016/j.cell.2015.04.012

Vitanza, N. A., Biery, M. C., Myers, C., Ferguson, E., Zheng, Y., Girard, E. J., Przystal, J. M., Park, G., Noll, A., Pakiam, F., Winter, C. A., Morris, S. M., Sarthy, J., Cole, B. L., Leary, S. E. S., Crane, C., Lieberman, N. A. P., Mueller, S., Nazarian, J., … Olson, J. M. (2021). Optimal therapeutic targeting by HDAC inhibition in biopsy-derived treatment-naïve diffuse midline glioma models. *Neuro-Oncology*, *23*(3), 376–386. https://doi.org/10.1093/neuonc/noaa249

Wachsberger, P. R., Lawrence, Y. R., Liu, Y., Rice, B., Feo, N., Leiby, B., & Dicker, A. P. (2014). Hsp90 inhibition enhances PI-3 kinase inhibition and radiosensitivity in glioblastoma. *Journal of Cancer Research and Clinical Oncology*, *140*(4), 573–582. https://doi.org/10.1007/s00432-014-1594-6

Wagner, J., Kline, C. L., Ralff, M. D., Lev, A., Lulla, A., Zhou, L., Olson, G. L., Nallaganchu, B. R., Benes, C. H., Allen, J. E., Prabhu, V. V., Stogniew, M., Oster, W., & El-Deiry, W. S. (2017). Preclinical evaluation of the imipridone family, analogs of clinical stage anti-cancer small molecule ONC201, reveals potent anti-cancer effects of ONC212. *Cell Cycle*, *16*(19), 1790–1799. https://doi.org/10.1080/15384101.2017.1325046

Wang, X., & Guo, Z. (2015). Anti-gliomas Effect of Chlorotoxin-Conjugated Onconase at High Dose. *Cell Biochemistry and Biophysics*, *73*(2), 389–392. https://doi.org/10.1007/s12013-015-0634-4

Wen, P. Y., Cloughesy, T. F., Olivero, A. G., Morrissey, K. M., Wilson, T. R., Lu, X., Mueller, L. U., Coimbra, A. F., Ellingson, B. M., Gerstner, E., Lee, E. Q., & Rodon, J. (2020). First-in-human phase I study to evaluate the brain-penetrant PI3K/mTOR inhibitor GDC-0084 in patients with progressive or recurrent high-grade glioma. *Clinical Cancer Research*, *26*(8), 1820–1828. https://doi.org/10.1158/1078-0432.CCR-19-2808

Wen, P. Y., Frederick De Groot, J., Battiste, J., Goldlust, S. A., Garner, J. S., Friend, J., Simpson, J. A., Damek, D., Olivero, A., & Cloughesy, T. F. (2022). Paxalisib in patients with newly diagnosed glioblastoma with unmethylated MGMT promoter status: Final phase 2 study results. *Journal of Clinical Oncology*, *40*(16), 2047.

Wright, S. C. E., Vasilevski, N., Serra, V., Rodon, J., & Eichhorn, P. J. A. (2021). Mechanisms of resistance to PI3K inhibitors in cancer: Adaptive responses, drug tolerance and cellular plasticity. *Cancers*, *13*(7). https://doi.org/10.3390/cancers13071538

Wu, G., Broniscer, A., McEachron, T. A., Lu, C., Paugh, B. S., Becksfort, J., Qu, C., Ding, L., Huether, R., Parker, M., Zhang, J., Gajjar, A., Dyer, M. A., Mullighan, C. G., Gilbertson, R. J., Mardis, E. R., Wilson, R. K., Downing, J. R., Ellison, D. W., … Baker, S. J. (2012). Somatic histone H3 alterations in pediatric diffuse intrinsic pontine gliomas and non-brainstem glioblastomas. *Nature Genetics*, *44*(3), 251–253. https://doi.org/10.1038/ng.1102

Xie, N., Zhang, L., Gao, W., Huang, C., Huber, P. E., Zhou, X., Li, C., Shen, G., & Zou, B. (2020). NAD+ metabolism: pathophysiologic mechanisms and therapeutic potential. *Signal Transduction and Targeted Therapy*, *5*(227). https://doi.org/10.1038/s41392-020-00311-7

Xu, J., Margol, A., Asgharzadeh, S., & Erdreich-Epstein, A. (2015). Pediatric brain tumor cell lines. *Journal of Cellular Biochemistry*, *116*(2), 218–224. https://doi.org/10.1002/jcb.24976

Yang, H., Rudge, D. G., Koos, J. D., Vaidialingam, B., Yang, H. J., & Pavletich, N. P. (2013). MTOR kinase structure, mechanism and regulation. *Nature*, *497*(7448), 217–223. https://doi.org/10.1038/nature12122

Yang, P., Zhang, L., Shi, Q. J., Lu, Y. B., Wu, M., Wei, E. Q., & Zhang, W. P. (2015). Nicotinamide phosphoribosyltransferase inhibitor APO866 induces C6 glioblastoma cell death via autophagy. *Pharmazie*, *70*(10), 650–655. https://doi.org/10.1691/ph.2015.5614

Zarghooni, M., Bartels, U., Lee, E., Buczkowicz, P., Morrison, A., Huang, A., Bouffet, E., & Hawkins, C. (2010). Whole-genome profiling of pediatric diffuse intrinsic pontine gliomas highlights platelet-derived growth factor receptor α and poly (ADP-ribose) polymerase as potential therapeutic targets. *Journal of Clinical Oncology*, *28*(8), 1337–1344. https://doi.org/10.1200/JCO.2009.25.5463

Zhang, M., Zhang, L., Hei, R., Li, X., Cai, H., Wu, X., Zheng, Q., & Cai, C. (2021). CDK inhibitors in cancer therapy, an overview of recent development. *Am J Cancer Res*, *11*(5), 1913–1935. www.ajcr.us/

Zhou, Z., Singh, R., & Souweidane, M. M. (2017). Convection-Enhanced Delivery for Diffuse Intrinsic Pontine GliomaTreatment. *Current Neuropharmacology*, *15*(1), 116–128. https://doi.org/10.2174/1570159X14666160614093

Danksagung

An dieser Stelle möchte ich mich auf das herzlichste bei allen bedanken, die mich während meiner Doktorarbeit begleitet und unterstützt haben.

Mein besonderer Dank gilt Herrn Dr. Alexander Beck, der es mir ermöglicht hat, in seiner Arbeitsgruppe meine Doktorarbeit anzufertigen. Dank seiner guten Betreuung konnte ich viel dazulernen, und ihm verdanke ich zahlreiche Denkanstöße zu meinem spannenden Promotionsprojekt.

Ein großes Dankeschön geht auch an den Institutsleiter des ZNP, Herrn Prof. Dr. Jochen Herms, für seine Bereitschaft, als Erstbetreuer meine Doktorarbeit zu unterstützen und zu begleiten. Ebenfalls möchte ich mich herzlich bei Frau Prof. Dr. Kirsten Lauber und Frau Prof. Dr. Louisa von Baumgarten bedanken, die gleichfalls der Betreuungskommission angehörten und mich stets mit ihren Anregungen unterstützt haben.

Ferner gilt mein Dank Frau Pia Freidel für die vielen anregenden Gespräche und die gute Zusammenarbeit im Labor.

Darüber hinaus danke ich herzlich Herrn Michael Schmidt, Frau Esther Kluj, Frau Christiane Groß und Frau Vanessa Boll, die mir stehts mit Rat und Tat zur Seite standen, wenn es um das Fixieren, Einbetten oder Schneiden von FFPE-Geweben ging.

Herzlichsten Dank an meine lieben Eltern, Erna und Ulrich, die mir stehts den Rücken gestärkt haben und mir das Studium bis zur Promotion überhaupt erst ermöglichten.

Auch möchte ich mich aufs Herzlichste bei meinen lieben Freunden Norbert und Sigrid bedanken, die mich während der gesamten Doktorarbeit stark unterstützt haben.

Zu guter Letzt möchte ich mich herzinniglich bei meiner Frau Daniela und meinem Sohn Marian bedanken, von deren liebevoller Begleitung und Unterstützung ich mich stets getragen fühlen durfte, auch und besonders in den anstrengenden Phasen.

Affidavit

LMU

LUDWIG-
MAXIMILIANS-
UNIVERSITÄT
MÜNCHEN

Promotionsbüro
Medizinische Fakultät

MMRS

Eidesstattliche Versicherung

Klenner, Marbod
Name, Vorname

Ich erkläre hiermit an Eides statt, dass ich die vorliegende Dissertation mit dem Titel:

DMG brain organoids: A new preclinical model for H3K27-altered diffuse midline glioma

selbständig verfasst, mich außer der angegebenen keiner weiteren Hilfsmittel bedient und alle Erkenntnisse, die aus dem Schrifttum ganz oder annähernd übernommen sind, als solche kenntlich gemacht und nach ihrer Herkunft unter Bezeichnung der Fundstelle einzeln nachgewiesen habe.

Ich erkläre des Weiteren, dass die hier vorgelegte Dissertation nicht in gleicher oder in ähnlicher Form bei einer anderen Stelle zur Erlangung eines akademischen Grades eingereicht wurde.

München, 06.02.2024
Marbod Klenner
Ort, Datum
Unterschrift Doktorandin bzw. Doktorand

Publication list

Poster:

ISPNO 2022: **DIPG-39. NEW PRECLINICAL MODELS FOR DIFFUSE MIDLINE GLIOMA.**

Published Poster abstract:

Klenner, M., Freidel, P., Filbin, M. G., & Beck, A. (2011). DIPG-39. NEW PRECLINICAL MODELS FOR DIFFUSE MIDLINE GLIOMA. *Neuro-Oncology*, *24* (Supplement 1).

Journal articles:

Anastasov, N., Hirmer, E., **Klenner, M**., Ott, J., Falkenberg, N., Bao, X., Mutschelknaus, L., Moertl, S., Combs, S., Atkinson, M. J., & Schmid, T. (2020). Mek1 inhibitor combined with irradiation reduces migration of breast cancer cells including mir-221 and ZEB1 EMT marker expression. Cancers, 12(12). https://doi.org/10.3390/cancers12123760